


	<b>The SCIRoCCo</b> <b>Scatterometry Handbook</b>	<b>Ref:</b>	SCI-PUB-14-0001-v01
		<b>Issue:</b>	6
		<b>Date:</b>	10/10/2017
		<b>Proj:</b>	SCIRoCCo Scatterometer Instrument Competence Centre

**Prepared by:**  
The SCIRoCCo Team:

### Change register

Version/Rev.	Date	Reason for Change	Changes
1.0	20/02/2015	Preliminary version	
1.1	26/03/2015	First Release. PM#1	TUW Soil Moisture
1.2	03/06/2015	MTR Release	Ocean Calibration (KNMI)
1.3	19/02/2016	PM#2 Release	Revised Ocean Calibration (KNMI) Section 4.3
2.1	28/06/2016	Review	Structure revised. Calibration and Data products description to be added.
2.2	24/10/2016	New chapter on ERS Calibration	Chapter 3.2
3.0	10/11/2016	FR pre-Release	Review
3.1	16/12/2016	FR pre-Release	Review
3.11	22/12/2016	Team Review Version	
4.0	10/01/2017	ESA Review	
5.0	26/01/2017	Team Review after ESA coments	Formatting made consistent. References checked and gathered in Chapter Scope has been revised. Section 2 restructured: Sections 2.1 2.2 2.3 added: Historical Developmen, Space-Borne Scatterometers Introduction to Scatterometry and theoretical background. The Scatterometry Glossary inserted in Appendix
5.1	27/01/2017	Typos corrected	Few typos and formatting
5.2	27/01/2017	Internal review. Branched	N/A
5.3	28/01/2017	References	Section 7. References have been merged into one. Duplications removed
6.0	10/10/2017	Final Project version	All formatting cleaned

### Document Approval

Role/Title	Name	Signature	Date
SCIRoCCo Project Manager	A. Bigazzi		10/10/2017
SCIRoCCo Contract Manager	R. Crapolicchio		10/10/2017
ESA Technical Officer	A. Dehn		10/10/2017

 <b>scirocco</b> scatterometer instrument competence centre	<b>The SCIRoCCo          Scatterometry Handbook</b>	<b>Ref:</b>	<b>SCI-PUB-14-0001-v01</b>
		<b>Issue:</b>	<b>6</b>
		<b>Date:</b>	<b>10/10/2017</b>
		<b>Proj:</b>	<b>SCIRoCCo</b> Scatterometer Instrument Competence Centre

	<h1>The SCIRoCCo Scatterometry Handbook</h1>	<b>Ref:</b>	SCI-PUB-14-0001-v01
		<b>Issue:</b>	6
		<b>Date:</b>	10/10/2017
		<b>Proj:</b>	SCIRoCCo Scatterometer Instrument Competence Centre

## Contents

1	Introduction.....	7
1.1	Scope.....	7
2	Scatterometry and the ERS Missions.....	10
2.1	Historical Development.....	10
2.2	Space-Borne Scatterometers.....	11
2.3	An introduction to scatterometry.....	14
2.3.1	Theoretical and practical background.....	15
2.4	Applications.....	17
2.4.1	Ocean winds.....	17
2.4.2	Land Surface Monitoring.....	19
2.4.3	Sea Ice and Drift.....	22
3	ERS Scatterometer Processing.....	24
3.1	The ERS Active Microwave Instrument (AMI).....	25
3.2	Towards a geophysical interpretation of the ESCAT backscatter data.....	26
3.3	The ERS-2 scatterometer ground processors.....	33
3.3.1	LRDPF ground processor – the first processor.....	33
3.3.1.1	Block diagram.....	33
3.3.2	ESACA/ASPS GROUND PROCESSOR.....	35
3.3.2.1	Block diagram.....	35
3.3.2.2	ADC non-linearity correction.....	35
3.3.2.3	Yaw angle estimation.....	36

	<h1>The SCIRoCCo Scatterometry Handbook</h1>	<b>Ref:</b>	SCI-PUB-14-0001-v01
		<b>Issue:</b>	6
		<b>Date:</b>	10/10/2017
		<b>Proj:</b>	SCIRoCCo Scatterometer Instrument Competence Centre

3.3.2.4	Residual Doppler frequency shift measurement.....	36
3.3.2.5	Computation of the yaw angle from the frequency shift.....	37
3.3.2.6	Data processing.....	39
3.3.2.6.1	Data filtering.....	39
3.3.2.6.2	Amplitude correction filter.....	39
3.3.2.6.3	Low pass filtering —Butterworth filter.....	40
3.3.2.6.4	Noise subtraction.....	40
3.3.2.6.5	Normalization/calibration.....	40
3.3.2.6.6	Spatial filtering.....	41
3.3.2.6.7	Sea-ice probability estimation .....	41
3.3.2.7	Quality control and monitoring.....	41
3.3.2.7.1	High power amplifier monitoring .....	42
3.3.2.7.2	Power spectrum monitoring .....	42
3.3.2.7.3	Doppler compensation monitoring .....	42
3.3.2.7.4	Internal calibration level monitoring.....	42
3.3.2.7.5	Number of valid samples contributing to a node.....	42
3.3.2.7.6	Noise power monitoring .....	42
4	Soil Moisture .....	44
4.1	Introduction.....	44
4.2	Theoretical background.....	45
4.2.1	Dielectric constant of soils .....	46
4.2.2	Dielectric constant of vegetation.....	48
4.2.3	Backscatter from natural land surfaces .....	49
4.3	The TU-Wien soil moisture model .....	51

	<h1>The SCIRoCCo Scatterometry Handbook</h1>	<b>Ref:</b>	SCI-PUB-14-0001-v01
		<b>Issue:</b>	6
		<b>Date:</b>	10/10/2017
		<b>Proj:</b>	SCIRoCCo Scatterometer Instrument Competence Centre

4.3.1	Introduction .....	51
4.3.2	Normalisation of ESCAT backscatter measurements.....	52
4.3.3	Vegetation correction.....	61
4.3.4	Soil moisture retrieval.....	63
4.3.5	Soil moisture uncertainty estimation.....	66
4.4	Applications .....	68
4.4.1	From surface soil moisture to root zone soil moisture.....	68
4.4.2	Creation of a Climate Data Record (ESA CCI soil moisture).....	70
4.4.3	Rainfall estimation through surface soil moisture observations .....	72
5	Ocean winds .....	73
5.1	Algorithms and Processing.....	73
5.2	Stress-equivalent 10m wind .....	74
5.3	Geophysical model function .....	76
5.4	Wind retrieval .....	77
5.5	Ambiguity removal.....	78
5.6	Quality control.....	78
5.7	NWP collocation.....	78
5.8	Calibration and Data quality .....	79
5.8.1	Calibration.....	79
5.8.2	Validation .....	79
5.9	Quality control and monitoring.....	79
5.10	NWP Ocean Calibration (NOC).....	80
5.10.1	Description .....	80
5.10.2	Application.....	84

	<h1>The SCIRoCCo Scatterometry Handbook</h1>	<b>Ref:</b>	SCI-PUB-14-0001-v01
		<b>Issue:</b>	6
		<b>Date:</b>	10/10/2017
		<b>Proj:</b>	SCIRoCCo Scatterometer Instrument Competence Centre

5.10.3	Error analysis.....	86
5.10.3.1	Sensitivity to NWP wind direction error.....	86
5.10.3.2	Sensitivity to NWP wind speed error .....	88
5.10.3.3	Sensitivity to non-linearity and GMF error.....	88
5.10.3.4	Sensitivity to QC filter settings .....	88
5.10.3.5	Temporal stability of backscatter .....	90
5.10.4	Concluding remarks.....	91
5.10.5	NOC-related detailed calculations.....	92
5.10.5.1	Compensating weights.....	92
5.10.5.2	Pseudobiases .....	94
5.11	Applications.....	98
6	The future .....	101
6.1	C-band Fan-Beam Scatterometer Heritage .....	101
6.2	Other Wind Resources.....	102
6.3	Doppler Scatterometer.....	102
7	References.....	103
Appendix A.	The Scatterometry Glossary.....	113

	<h1>The SCIRoCCo Scatterometry Handbook</h1>	<b>Ref:</b>	SCI-PUB-14-0001-v01
		<b>Issue:</b>	6
		<b>Date:</b>	10/10/2017
		<b>Proj:</b>	SCIRoCCo Scatterometer Instrument Competence Centre

## 1 Introduction

### 1.1 Scope

The Scatterometry Handbook aims at providing, in a single publication, a knowledge base on Scatterometry data processing, and references to the relevant literature, needed to the users for exploiting the wealth of available scatterometer data, notably but not limited to those provided by ESA's ERS Missions.

This Handbook, is focused on two major applications of scatterometer data: Ocean Winds and Soil Moisture. Calibration and cross-calibration are paramount to the understanding and full exploitation of scatterometer data, and make up a consistent part of this publication.

The Handbook is organized as follows:

- Y Section 1 is the Introduction.
- Y Section 2, Scatterometry, provides an introduction to Scatterometry in general and to Space Borne scatterometry in particular, also discussing its main applications over Land and Ocean.
- Y Section 3, ERS Scatterometer Processing, explains in full details the processing from instrument measurement to Level-1 products, and all issues related with instrument calibration.
- Y Section 4 is dedicated to Soil Moisture
- Y Section 5 is dedicated to Ocean Winds and Numerical Weather Predictions
- Y Section 6 closes with a view on the future of Scatterometry
- Y Section 7 contains the bibliographical references
- Y Appendix A contains the Scatterometry Glossary, defining the commonly agreed terminology to use in all the documents generated by the SCIRoCCo Consortium.

This Handbook has been compiled by the SCIRoCCo (SCatterometer InstRument Competence Centre) working group, established in 2014 by ESA, the European Space Agency, following the end of the operational phase of the ERS-2 Mission. SCIRoCCo aims at promoting the continuing exploitation of this uniquely extended set of Scatterometer (ESCAT) data at medium (25 km, 50 km) spatial resolution, and at improving the quality of current and future C-band scatterometer products.

	<h1>The SCIRoCCo Scatterometry Handbook</h1>	<b>Ref:</b>	SCI-PUB-14-0001-v01
		<b>Issue:</b>	6
		<b>Date:</b>	10/10/2017
		<b>Proj:</b>	SCIRoCCo Scatterometer Instrument Competence Centre

<b>Acronyms</b>	
ADEOS	Advanced Earth Observing Satellite
AMI	Active Microwave Instrument
AMSR-E	Advanced Microwave Scanning Radiometer - Earth Observing System
AR	Ambiguity Removal
ASCAT	Advanced Scatterometer
BUFR	Binary Universal Format Representation
CERSAT	Centre ERS d'Archivage et de Traitement
DAAC	Distributed Active Archive Center
EARS	EUMETSAT Advanced Retransmission Service
ECV	Essential Climate Variable
EPS	Eumetsat Polar System
ERS	European Remote-Sensing Satellite
ESA	European Space Agency
ESCAT	AMI ERS-1/2 satellites in scatterometer mode
EUMETCast	EUMETSAT's Digital Video Broadcast Data Distribution System
EUMETSAT	European Organisation for the Exploitation of Meteorological Satellites
FCDR	Fundamental Climate Data Record
GMF	Geophysical Model Function
HDF	Hierarchical Data Format
HiRLAM	High Resolution Local Area Modelling for numerical weather prediction
IFREMER	Institut français de recherche pour l'exploitation de la mer
JAXA	Japanese Aerospace Exploration Agency
JPL	Jet Propulsion Laboratory (NASA)
KNMI	Royal Netherlands Meteorological Institute
LRDPF	Low-Rate Data Processing Facility
MetOp	Meteorological Operational satellite
MLE	Maximum Likelihood Estimator
NASA	National (US) Aeronautics and Space Administration
NOAA	National (US) Oceanic and Atmospheric Administration
NRT	Near-Real-Time
NSCAT	NASA Scatterometer
NWP	Numerical Weather Prediction
OSI SAF	Ocean and Sea Ice SAF (EUMETSAT)
PDF	Probability Density Function
PODAAC	Physical Oceanography Distributed Active Archive Center
QC	Quality Control
QuikSCAT	Quick scatterometer mission(NASA)
RENE	Rehearsals ERS-1 Validation North Europe
RMDCN	Regional Meteorological Data Communication Network
SAF	Satellite Application Facility



	<h1>The SCIRoCCo Scatterometry Handbook</h1>	<b>Ref:</b>	SCI-PUB-14-0001-v01
		<b>Issue:</b>	6
		<b>Date:</b>	10/10/2017
		<b>Proj:</b>	SCIRoCCo Scatterometer Instrument Competence Centre

SAR	Synthetic Aperture Radar
SASS	Seasat-A Scatterometer System
SCIRoCCo	Scatterometer Instrument Competence Centre
SeaWinds	scatterometer on-board the QuikSCAT, ADEOS-II and RapidScat platforms
SMOS	Soil Moisture and Ocean Salinity Mission (ESA)
SMMR	Scanning Multi-channel Microwave Radiometer
SSM/I	Special Sensor Microwave Imager
SST	Sea Surface Temperature
TMI	TRMM microwave imager (TMI)
TRMM	Tropical Rainfall Measuring Mission
u	West-to-east wind component
U10S	Stress-equivalent 10-m-height wind speed
v	South-to-north wind component
WVC	Wind Vector Cell

	<p>The SCIRoCCo Scatterometry Handbook</p>	Ref:	SCI-PUB-14-0001-v01
		Issue:	6
		Date:	10/10/2017
		Proj:	SCIRoCCo Scatterometer Instrument Competence Centre

## 2 Scatterometry and the ERS Missions

ERS-1 and ERS-2 were the first “European Remote Sensing” satellites. ESCAT, was the scatterometer on-board both ERS Missions. ESA launched ERS-1 on 17 Jul 1991, carrying out its Operations for almost a decade, until [March 10 2000](#). ERS-2 operations partly overlapped with those of ERS-1. ERS-2 was launched on 20 April 1995, operating until [September 5th 2011](#). Data from the two ERS Missions thus cover a remarkable 20 year span, making it an invaluable source of information for climatological records.

ERS data will be a major component of an over 40 year dataset of C-band scatterometer data which will result from the ERS legacy and from ESCAT’s successors: the Advanced Scatterometer (ASCAT) instrument, flying on the MetOp satellites of the EUMETSAT Polar System (EPS), and the EPS Second Generation ASCAT (ASCAT-SG), now being designed, and which is keeping the ESCAT C-band static fan beam concept. This extended dataset is going to prove a unique resource for climate applications, from wind climatologies to air–sea interactions and atmospheric processes, only to name a few. All-weather scatterometer observations have proven accurate and important for the forecasting of dynamic and severe weather. Scatterometers also provide unique forcing information on the ocean eddy scale and on soil moisture, snow cover and sea ice, all important inputs to oceanographic and land applications. Demand for ESCAT data and services are therefore expected to remain high, in the years to come.

### 2.1 Historical Development

Scatterometers measure the return echoes of a transmitted radar pulse as it interacts with the dielectric discontinuities it encounters in its path. The backscatter coefficient, which quantifies the amount of power returned relative to that originally transmitted, is usually modelled in terms of surface scattering off rough interfaces, and volume scattering from inhomogeneous media. With a cm-scale wavelength, microwaves are almost insensitive to atmospheric cloud and rain droplets, somewhat susceptible to vegetation, and most responsive to the dielectric properties of the Earth’s ocean and land surfaces, with a backscatter response that depends on the change in dielectric permittivity at the surface, and the angle of incidence with which the original pulse hits the surface. Wind scatterometers measure the radar backscatter from wind-generated centimetre-sized gravity capillary waves and provide high-resolution vector wind fields over the oceans. All-weather scatterometer observations have proven accurate and important for the forecasting of dynamic and severe weather. Oceanographic applications have been developed since scatterometers provide unique forcing information on the ocean eddy scale. Scatterometers also provide useful information on soil moisture, snow cover and sea ice (see Figure 2.1.1).

	<h1>The SCIRoCCo Scatterometry Handbook</h1>	<b>Ref:</b>	SCI-PUB-14-0001-v01
		<b>Issue:</b>	6
		<b>Date:</b>	10/10/2017
		<b>Proj:</b>	SCIRoCCo Scatterometer Instrument Competence Centre

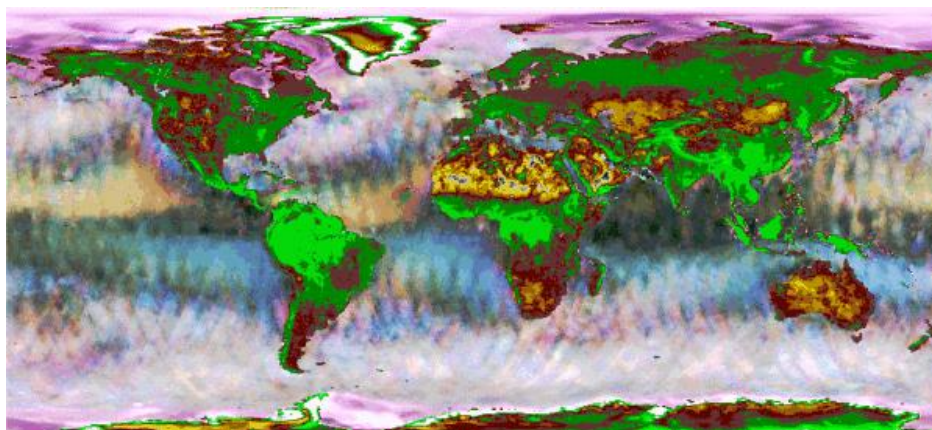


*Figure 2.1.1 Color rendering from a radar map of Earth's surface as observed by the ERS scatterometer. Sea ice is shown in violet, variable winds in grey and high winds in white, but with wind sensitivity depending somewhat on swath position. The yellow and blue in the northern and southern hemispheres indicate trade winds and correspond to higher signals in the fore and aft antennae, respectively, and thus indicate the directional stability of the wind in the intertropical regions. (Data processing by IFARS, Germany, for land surfaces, and by the ERS Product Control Service at ESRIN for oceans. (©ESA, 1998)*

During the Second World War, the radar technique was developed and used to detect and track hostile vessels. Detection, though, was hampered by wind speed. Starting from this observation, the idea of measuring wind near the sea surface by using microwaves, was developed. The first scatterometer was thus born (see e.g. Moore & Pierson, 1967).

## 2.2 Space-Borne Scatterometers

Space-borne scatterometers provide unique global ocean surface vector wind products at high spatial resolution. Since they operate at microwave (radar) frequencies, these instruments are not hindered by cloud cover and hence are able to reveal phenomena such as polar front disturbances and tropical cyclone winds. Figure 2.2.1 shows mesoscale ESCAT winds (red) detected by the ESCAT instrument on ERS-2 and Numerical Weather Prediction (NWP) model winds (blue wind vectors). The ESCAT mesoscale wind details in the area where the cold northerly flow interacts with the warmer southerly flow line up well with the geostationary satellite cloud bands at the time of the ERS-2 overpass. The NWP winds describe only the larger scales well.

	<h1>The SCIRoCCo Scatterometry Handbook</h1>	Ref:	SCI-PUB-14-0001-v01
		Issue:	6
		Date:	10/10/2017
		Proj:	SCIRoCCo Scatterometer Instrument Competence Centre

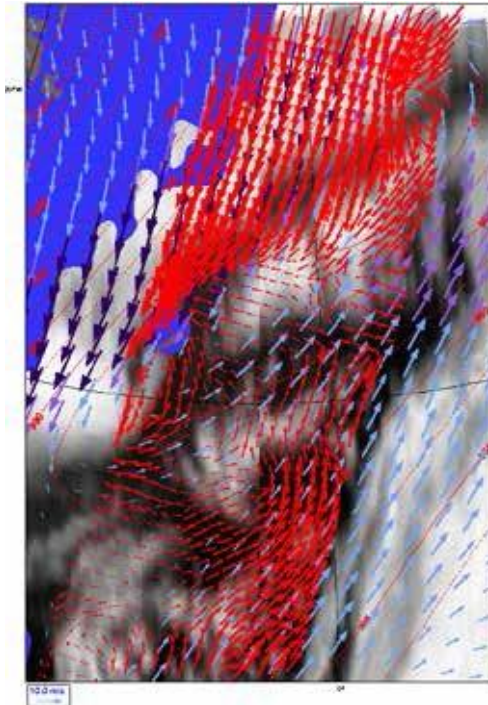


**Figure 2.2.1** Scatterometer winds from ERS-2 at around 12:00 GMT on 24 November 1999 at 70°N and 0°W ([www.knmi.nl/scatterometer](http://www.knmi.nl/scatterometer)). The grey shading is a Meteosat IR image coherent with the scatterometer winds. Blue mask: areas where the sea surface temperature is below zero and sea ice is probable. Grey mask: land at 80°N and 20°W (top right). The red contours indicate surface pressure from the HIRLAM model at KNMI (3-h forecast). Blue and purple are the spatially smooth wind vectors from HIRLAM (the amount of purple increases with wind speed). The red wind vectors depict the spatially detailed ERS-2 winds. The red dots indicate where winds were rejected because of a confused sea state (bottom left) or the presence of sea ice (top left). Scatterometers reveal more coherent spatial detail than NWP winds. (© Eumetsat OSI SAF, 1999)

	<h1>The SCIRoCCo Scatterometry Handbook</h1>	Ref:	SCI-PUB-14-0001-v01
		Issue:	6
		Date:	10/10/2017
		Proj:	SCIRoCCo Scatterometer Instrument Competence Centre

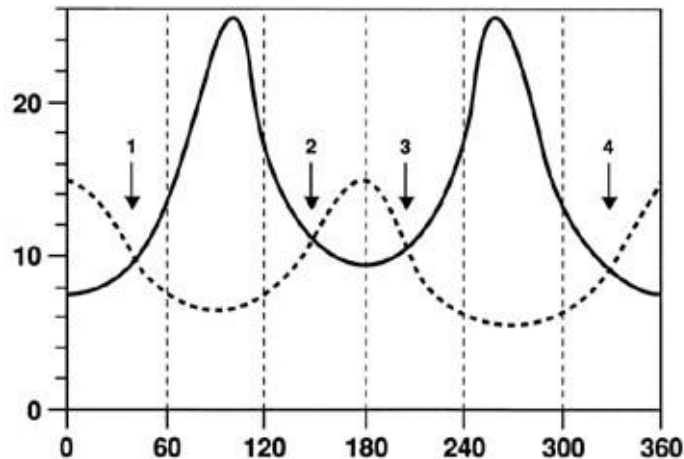


**Figure 2.2.2.** Wind speed as a function of wind direction for fore and aft beam measurements of backscatter from SASS data. The arrows indicate the four possible solutions for this typical case. (© Utrecht University, Stoffelen, 1998)

Scatterometers have been flown on space missions since the early 70's. The first time with NASA's Earth Resources Experiment Package (EREP) on Skylab, the so-called S193 scatterometer operated between November 1973 and January 1974 to prove the feasibility of wind speed remote sensing from space.

The technique was refined with the first operational NASA's Seasat-A Scatterometer System (SASS), operating between June and November in 1978. SASS bore two antennae on each side of the satellite pointing at 45° and 135° azimuth to the ground track. A location in the swath would be first hit by the fore beam, and a few minutes later by the aft beam providing two backscatter measurements with a 90° difference in azimuth. Figure 2.2.2 illustrates the analysis of two such measurements, showing the wind speed solution as a function of all possible wind directions. Given the dependency of the backscatter signal on wind direction, four solutions exist in this case. This ambiguity posed a strong limitation on the usefulness of the SASS wind data, and extended manual efforts were needed to remove the ambiguity in order to obtain an acceptable wind product (Peteherych et al., 1984). The usefulness of this product has been demonstrated (see, e.g. Stoffelen & Cats, 1991).

ESA's Earth Remote Sensing (ERS-1 and ERS-2) ESCAT scatterometer missions operated globally between 1992 and 2001 to provide the first continuous record of global wind vector measurements of demonstrated quality. Since then, the global record of ocean wind vectors has been supported by the NASA NSCAT instrument on ADEOS I (1996-1997), the SeaWinds instrument on Quikscat (1999 to 2009), ADEOS II (2002) and RapidScat (2014-2016), along with ESA's Advanced Scatterometer on Metop A (2007 to present) and Metop B (2012 to present). More recently, the Indian Space Research Organization (ISRO) OSCAT instrument on OceanSat-2 (2009-2014) and SCATSat-1 (2016 to present), and the Chinese State Oceanic Administration (SOA) HY2A scatterometers (2011 to present) complete the family. Their general characteristics are detailed in Table 2.2.1 below.

	<b>The SCIRoCCo</b> <b>Scatterometry Handbook</b>	<b>Ref:</b>	SCI-PUB-14-0001-v01
		<b>Issue:</b>	6
		<b>Date:</b>	10/10/2017
		<b>Proj:</b>	SCIRoCCo Scatterometer Instrument Competence Centre

**Table 2.2.1.** General characteristics of space-borne scatterometers (current and approved missions)

Instrument	Platform	Frequency (GHz)	Antenna	Polarization	Incidence (deg)	Resolution	Operating date
S193	Skylab	13.9	Scanning pencil beam	HH VV HV VH	0-48	16 km	1973
SASS	Seasat	14.6	Two-sided 2 fan-beams	VV HH	0-70	50 km	1978
AMI	ERS-1, ERS-2	5.3	One-sided 3 fan-beams	VV	18-57	50 km	1991-2000 1995-2011
NSCAT	ADEOS	14	Two-sided 3 fan-beams	VV HH	17-60	25 km	1996-1997
SeaWinds	QuickScat, ADEOS-II	13.4	Scanning pencil beam	VV HH	46 & 54	25 km	1999-2009 2002-2003
ASCAT	MetOp-A, MetOp-B, MetOp-C	5.3	Two-sided 3 fan beams	VV	25-65	25 km	2006- 2012- 2018-
OSCAT	OceanSat-2, ScanSat-1, OceanSat-3	13.5	Scanning pencil beam	VV HH	49 & 57	25 km	2009-2014 2016- 2018-
Ku-RFSCAT	YaiHang-2A, YaiYang-2B,	13.3	Scanning pencil beam	VV HH	41 & 48	25 km	2011- 2018-
Rapidscat	ISS	13.4	Scanning pencil beam	VV HH	46 & 54	25 km	2016-
SCAT	CFOSAT	13.25	Scanning fan beam	VV HH	20-65	50km	2018-
WindRad	FengYung-3E, FengYung-3H	13.26 & 5.3	Scanning fan beam	VV HH	36-45 37-43	10 km 20 km	2018- 2021-
SCAT-M3	Meteor-M N3	13.4	Scanning pencil beam			25 km	2021-

## 2.3 An introduction to scatterometry

A (radar) scatterometer is an instruments that provide an extremely accurate measure of the radar backscatter of the Earth surface. Radar backscatter from extended areas, where a large number of scatterers are present in the footprint of the antenna, as opposed to point targets where the echo signal is dominated by a single scatterer, are affected by a seemingly random noise called speckle, inherent to the coherent nature of the instrument. The measurements are further affected by instrument noise, by the black-body emission of the observed surface and possibly by interferences.

In order to achieve highly accurate measurements, the effect of the speckle has to be attenuated. This is obtained by performing incoherent integration of the measurements, where the measurements are thus incoherently averaged over

	<h1>The SCIRoCCo Scatterometry Handbook</h1>	<b>Ref:</b>	SCI-PUB-14-0001-v01
		<b>Issue:</b>	6
		<b>Date:</b>	10/10/2017
		<b>Proj:</b>	SCIRoCCo Scatterometer Instrument Competence Centre

a certain spatial area, called a cell. The accurate radiometry is thus obtained at the expense of the spatial resolution, whereas for example in Synthetic Aperture Radar (SAR), high spatial resolution is preferred and speckle thus has to be tolerated. Noise and black-body radiation powers are subtracted from the incoherently-averaged measurements to remove their contributions. Finally, in order to cope with the possibly varying output power of the high power amplifier generating the transmitted wave, the power of the transmitted wave is measured and taken into account when computing the normalized backscattering coefficient.

The fundamental product of a (radar) scatterometer is thus a normalized radar cross section of the Earth surface (also called sigma-zero or sigma-naught) at a typical spatial resolution of 50km or 25km.

As with any radar measurement, the carrier frequency of the transmitted waveform, the incidence angle of that wave onto the Earth surface and the look angle (direction of the propagation of the wave with respect to the North) are essential parameters of the measurement.

The main applications of space-borne scatterometry are wind vector retrieval at the surface of the oceans, soil moisture extraction over land and (sea-)ice monitoring and are detailed below.

One of the main applications of scatterometry is wind vector retrieval and the associated geophysical model function exhibits ambiguities, i.e., different wind vectors (speed and direction) can yield the same backscatter as discussed in the previous section. In order to resolve these ambiguities, measurements of the same area at the same time at different look angles are necessary. This explains why all scatterometer instruments measure the normalized backscatter simultaneously in different directions, either using different fixed-direction fan-beam antennas or using rotating antennas.

### 2.3.1 Theoretical and practical background

Wind scatterometry was developed heuristically. It was found experimentally that the sensitivity to wind speed and direction describe well the changes in backscatter over the ocean at moderate incidence angles due to changes in surface roughness, as depicted in figure 5.2.1 (Valenzuela, 1978). In return, backscatter measurements can be used to determine the wind speed and wind direction in a Wind Vector Cell (WVC).

Measured backscatter appears indeed primarily due to surface roughness. One may then define the air-sea interaction and the associated temporal evolution of the ocean topography in a mathematical approximation and further assume e.m. scattering of microwaves on gravity-capillary waves in order to obtain a theoretically-based relationship between wind-induced ocean surface roughness and radar backscatter. In fact, it has been experimentally established that first-order Bragg scattering appears to be the main contribution, but theoretically-based models have a hard time to get a description to within the precision of the scatterometer measurement. Critical assumptions in describing ocean microwave scattering are among others:

- Electromagnetic (e.m.) closure;

	<h1>The SCIRoCCo Scatterometry Handbook</h1>	Ref:	SCI-PUB-14-0001-v01
		Issue:	6
		Date:	10/10/2017
		Proj:	SCIRoCCo Scatterometer Instrument Competence Centre

- Isotropic Bragg scattering; are breaking and wind-reinforced cm-waves really the same in all directions?
- Roughness spectrum, different spectra provided wildly different backscatter; are spectra always the same?
- Foam coverage, particularly at strong winds;

More advanced theoretical developments remains useful, in particular towards the design of new missions that effectively obtain simultaneous information on the ocean winds (backscatter) and on the ocean motion (Doppler), probably exploiting new wavelengths and new polarizations (e.g., Fois et al., 2014).

Nevertheless, for ERS wind retrieval, we describe the empirical developments in geophysics that led to the current state-of-the-art scatterometer wind retrieval below. We first describe the stress-equivalent 10-meter wind that is retrieved from wind scatterometers.

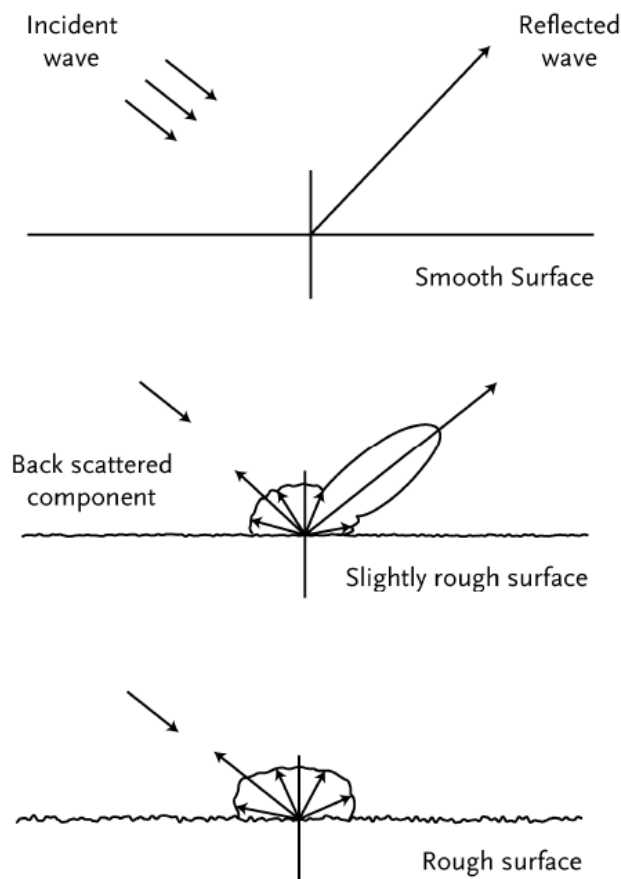


**Figure 2.3.1.** Schematic representation of microwave scattering and reflection at a smooth (a), rough (b) and very rough (c) ocean surface. As the roughness increases more microwave power is returned towards the direction of the microwave source.



	<h1>The SCIRoCCo Scatterometry Handbook</h1>	<b>Ref:</b>	SCI-PUB-14-0001-v01
		<b>Issue:</b>	6
		<b>Date:</b>	10/10/2017
		<b>Proj:</b>	SCIRoCCo Scatterometer Instrument Competence Centre

In Section 3.1, the main functioning principle of the ERS scatterometer is discussed in greater detail.

Section 3.2 details all the processing principles and steps allowing to retrieve the basic measurables from the Instruments' echo signal.

Soil moisture retrieval principles are described in Sections 4.2 and following.

Ocean Winds processing is described in Section 5.

Numerical Weather Prediction Ocean Calibration is discussed in Section 5.10

## 2.4 Applications

### 2.4.1 Ocean winds

ESCAT was originally designed for wind monitoring. Retrieved ERS scatterometer winds have proven to be very useful for the forecasting of dynamic weather (Le Meur et al., 1998; Isaksen & Stoffelen, 2000) using the 4D-Var data assimilation system. This is mainly due to the capability of the 4D-Var system to assimilate winds with dual ambiguity (Stoffelen & Anderson, 1997b) and to propagate the ESCAT surface information vertically (Isaksen & Janssen, 2004). Increased coverage, such as from tandem ERS-1/ERS-2 measurements, clearly improve the forecasts of extreme events (e.g. Stoffelen & Beukering, 1997; Le Meur et al., 1998); see Fig. 2.3.1. Severe storms that hit Europe often originate over the North Atlantic, where sparse meteorological observations are available. Consequently, the initial stages of severe storms are often poorly analysed and their development poorly predicted (e.g. ESA, 1999). As a result, occasional devastating ocean or coastal wind and wave conditions remain a major challenge for NWP. In addition, NWP data assimilation systems are cycled over observation windows, e.g. of 6 h length, with cut-off times in the range of 2–6 h. Therefore, particularly in case of fast weather developments, which often have large societal impacts, the timely use of satellite observations is complicated.

Ref:	SCI-PUB-14-0001-v01
Issue:	6
Date:	10/10/2017
Proj:	SCIRoCCo Scatterometer Instrument Competence Centre

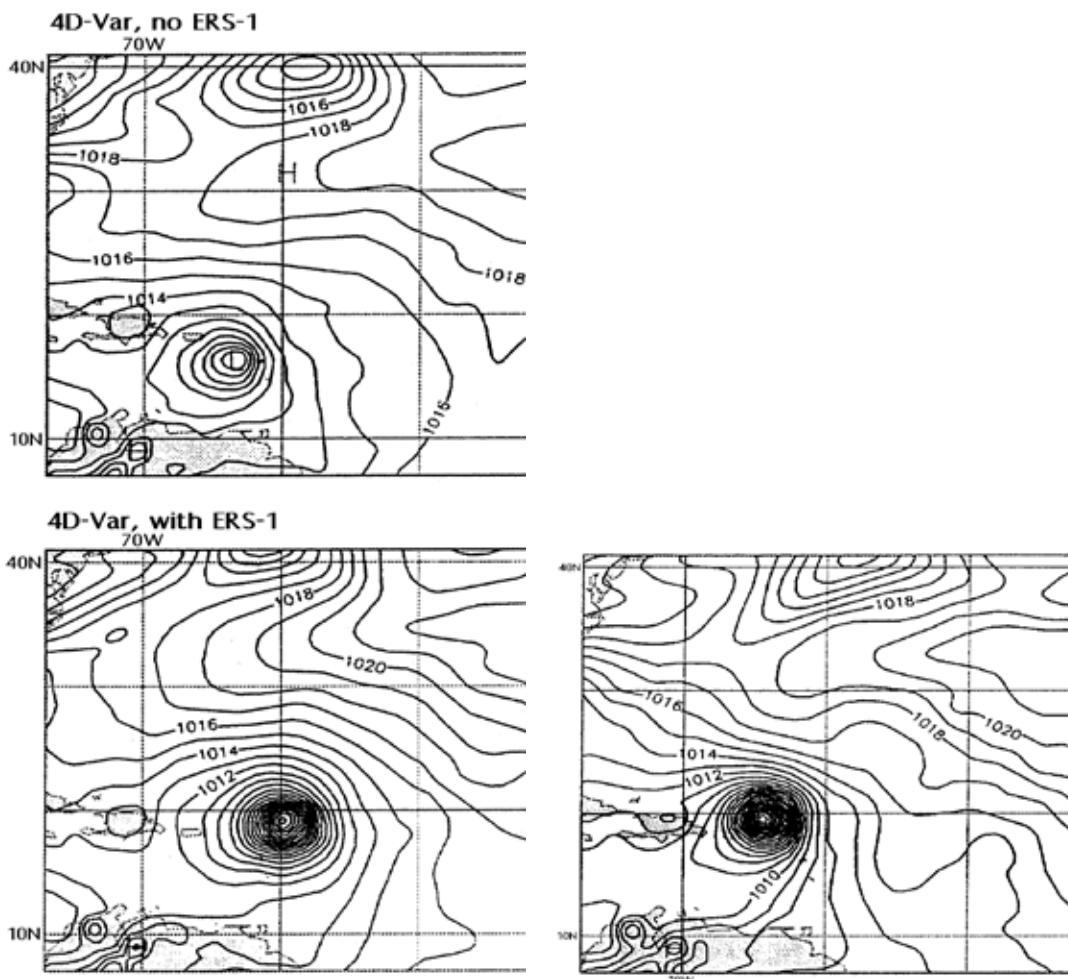


**Figure 2.3.1.** Mean sea level pressure fields from the ECMWF model valid at 12:00 UTC on 6 September 1995. Top left: Five-day forecast using the 4D-Var data assimilation system without ERS scatterometer data. Bottom left: Forecast using the 4D-Var data system with scatterometer data. Bottom right: Analysed field for verification of the forecasts showing an excellent tropical cyclone strength forecast with ESCAT winds at the 5-day range. (Le Meur et al., 1998)

Scatterometer data are therefore used for nowcasting applications such as hurricane warnings over sea (Sienkiewicz et al., 2010) for marine traffic or offshore activities. Moreover, the near-surface wind conditions drive the ocean circulation, which in turn plays a major role in the climate system and in marine ecosystems (e.g. fisheries). Scatterometer winds have proven to be very relevant in driving ocean circulation and air-sea interactions (Chelton et al., 2004; Tokmakian, 2005; Blanke et al., 2005; Liu & Xie, 2006), which in turn play a major role in the climate system

	<p>The SCIRoCCo Scatterometry Handbook</p>	Ref:	SCI-PUB-14-0001-v01
		Issue:	6
		Date:	10/10/2017
		Proj:	SCIRoCCo Scatterometer Instrument Competence Centre

and marine biology (Moore & Renfrew, 2005). An overview of the Ocean Vector Wind observation requirements, capabilities and applications is provided in Bourassa et al. (2009).

## 2.4.2 Land Surface Monitoring

Because ESCAT was designed for wind monitoring, it was initially not clear if and how it might be useful for monitoring of the land surface. One particular concern was that the spatial resolution of ESCAT is simply too coarse to be of value for land applications due to the high heterogeneity of land surfaces. Nevertheless, the global systematic coverage achieved by ESCAT attracted several research groups who began to investigate the capabilities of ESCAT for mapping of vegetation (Frison & Mougín, 1996), soil moisture (Wagner et al., 1999b), freeze/thawing (Wismann, 2000) and snow (Drinkwater et al., 2001).

One of the scientific challenges faced by all initial land surface studies was the strong dependency of the backscattering coefficient on the incidence angle, which varies from 18° for the mid-beam in the near-range, to 59° for the fore and aft beams in the far range. Therefore, the backscattering coefficient changes significantly over the image swath, and from acquisition to acquisition, making the interpretation of the images, or time series, elusive without a prior correction or normalisation of the backscatter data. Thus many of the initial studies addressed this dependency by fitting a linear function to the ESCAT backscatter measurements collected over a long period such as a month (Mougín et al., 1995; Schmullius, 1997), following a procedure previously developed for the SASS scatterometer by Kennett & Li (1989). This allowed studies of the relationship between the ESCAT measurements and global land cover, and seasonal land surface dynamics due to vegetation phenology or freeze/thaw processes in high-latitude areas. Nevertheless, this monthly fitting procedure suppresses short-term signal fluctuations caused, for example, by changes in soil moisture, short-term freeze/thaw events, or changes in snow morphology, rendering a more physically based interpretation of the ESCAT data impossible.

To improve our capabilities to analyse ESCAT data over land, more advanced modelling approaches have been developed in which the ESCAT signal can be decomposed into its different backscatter components. One such approach is the method developed by Wagner et al. (1999b), where in one of the first processing steps the incidence angle dependency of  $\sigma^0$  is determined for each land surface pixel and for each day of the year by comparing the quasi-simultaneous mid- and aft/fore beam backscatter measurements. This knowledge of the incidence angle behaviour then not only allows extrapolation of the backscatter measurements to a given reference angle (40°), but also separating the backscatter contributions due to seasonal vegetation growth and decay from the shorter-term soil moisture fluctuations (Wagner et al., 1999a). Furthermore, several semi-empirical backscatter models typically composed of bare soil backscatter- and volume scattering formulations for simulating backscatter of vegetation- and snow-covered surfaces have been developed (Magagi & Kerr, 1997; Pulliainen et al., 1998; Wen & Su, 2003;

	<h2 style="text-align: center;">The SCIRoCCo Scatterometry Handbook</h2>	<b>Ref:</b>	SCI-PUB-14-0001-v01
		<b>Issue:</b>	6
		<b>Date:</b>	10/10/2017
		<b>Proj:</b>	SCIRoCCo Scatterometer Instrument Competence Centre

Woodhouse & Hoekman, 2000; Zribi et al., 2008). These semi-empirical models can be used to improve our theoretical process understanding and, at a more practical level, the simultaneous retrieval of soil moisture, vegetation and other land surface parameters (e.g. roughness) using iterative least-squares matching procedures. These models have been implemented over selected world regions with varying degrees of success, but not yet on a global scale.

These research efforts led to the derivation of the first global long-term (1992–2000) soil moisture database using ESCAT data from both ERS-1 and ERS-2 (Scipal et al., 2002; Wagner et al., 2003; see Fig. 2.3.2). This dataset was released in 2002 by the Vienna University of Technology (TU Wien) and freely shared with the scientific community. Fortunately, the dataset raised considerable interest and several validation studies carried out by independent research teams quickly demonstrated the high quality of the data (Dirmeyer et al., 2004; Drusch et al., 2004; Pellarin et al., 2006). This was unexpected because active C-band measurements had not been considered to be well suited for the retrieval of soil moisture. This was mainly because, first, active measurements are more sensitive to surface roughness compared with passive microwave measurements and, second, the C-band ( $\lambda = 3.8\text{--}7.5$  cm) is less able to penetrate vegetation and the soil than the L-band ( $\lambda = 15\text{--}30$  cm) (Wagner et al., 2007). Exactly for these reasons, passive long-wavelength measurement concepts have been selected for ESA's Soil Moisture and Ocean Salinity (SMOS) mission and NASA's Soil Moisture Active Passive (SMAP) mission – the first two satellite missions developed specifically for the retrieval of soil moisture – utilising passive sensors operating at the L-band (Entekhabi et al., 2004; Kerr, 2007).

Nevertheless, the positive results from the validation studies, and the increasing use of the ESCAT soil moisture database in such diverse applications as hydrology (Parajka et al., 2006; Scipal et al., 2005), Numerical Weather Prediction (Scipal et al., 2007; Zhao et al., 2006), agronomy (De Wit & van Diepen, 2007) and climate monitoring (Künzer et al., 2009) led to the recommendation to build up a global near-real time soil moisture service for ASCAT. This operational service was developed by Eumetsat in cooperation with TU Wien, and went fully operational in December 2008 (Bartalis et al., 2007; Wagner et al., 2010).

	<h1>The SCIRoCCo Scatterometry Handbook</h1>	Ref:	SCI-PUB-14-0001-v01
		Issue:	6
		Date:	10/10/2017
		Proj:	SCIRoCCo Scatterometer Instrument Competence Centre

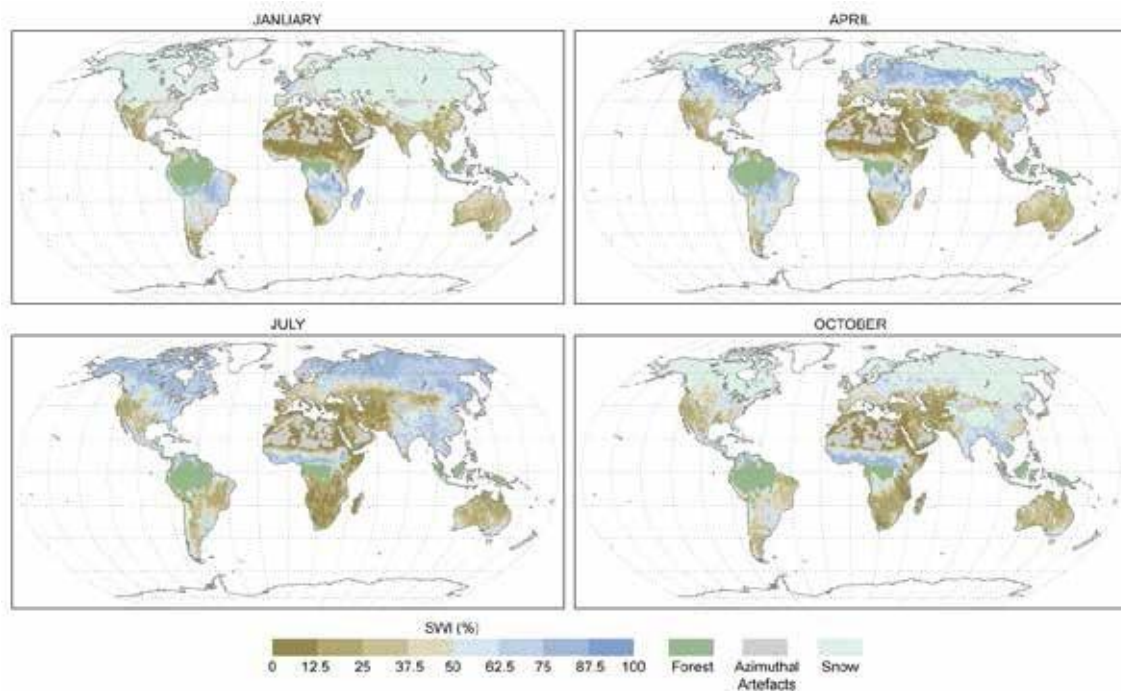


**Figure 2.3.2.** Mean monthly soil moisture derived from ESCAT backscatter data (1992–2000) for January, April, July and October. Brown tones indicate dry conditions (wilting level), blue tones indicate wet conditions (field capacity). Tropical forest, desert regions with strong azimuth effects, and areas affected by snow and frost have been masked out.

In retrospect, it can be said that this unexpected success was possible because of ESCAT’s unique characteristics:

- the multi-incidence angle viewing capability, which allows the separation of vegetation and soil moisture effects;
- the high temporal sampling rate, which allows researchers to exploit the advantages of change detection; and
- the excellent radiometric accuracy, which results in a suitable signal-to-noise ratio for the task of soil moisture retrieval.

Now that the ERS-2 mission has come to a successful end, there is an opportunity to reprocess the complete ESCAT data archive to 25 km to create a Fundamental Climate Data Record (FCDR) that will provide crucial inputs to any effort dealing with the creation of an Essential Climate Variable (ECV) record on soil moisture (Wagner et al., 2009). The first efforts in this direction are underway and it is planned to release an improved 25-km resolution ESCAT soil moisture dataset in 2013. Furthermore, by merging ESCAT and ASCAT soil moisture data with a suite of soil moisture products derived from passive microwave sensors (SMMR, SSM/I, TMI, AMSR-E) it will be possible to

	<p>The SCIRoCCo Scatterometry Handbook</p>	Ref:	SCI-PUB-14-0001-v01
		Issue:	6
		Date:	10/10/2017
		Proj:	SCIRoCCo Scatterometer Instrument Competence Centre

create a 30+ year soil moisture ECV data record (Dorigo et al., 2010; Liu et al., 2011). Such a first soil moisture ECV dataset, where ESCAT is essential for characterising the climate in the 1990s, is also released (Hollman et al., 2013).

### 2.4.3 Sea Ice and Drift

The extent of sea ice over the polar oceans is a critical parameter for understanding and forecasting ocean circulation and climate change. Sea ice is difficult to observe using satellite optical sensors because of the low level of illumination and the frequent cloud cover in polar regions. Microwave instruments and in particular satellite-borne radars, such as the ESCAT scatterometers, are of great interest because of their large temporal and spatial coverage and their all-weather measurement capability. The development of specific data analysis methods for these radars led to the detection of sea ice and estimates of its extent, drift and age (see Fig. 2.3.3). A routine ESCAT processing has been developed at the ERS Processing and Archiving Facility of the French Research Institute for Exploitation of the Sea (CERSAT/IFREMER) to produce fields of sea ice age, drift and extent, with polar coverage, on a weekly and monthly basis.

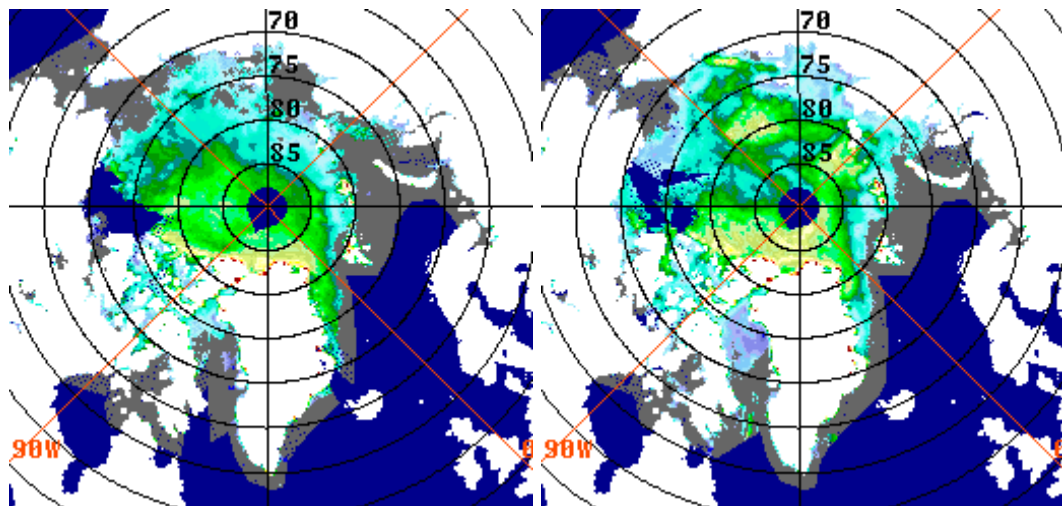


**Figure 2.3.3.** Images of the backscatter coefficient over the Arctic region, observed at an incidence angle of  $40^\circ$  during October 1995 (ERS 1, left) and October 1996 (ERS 2, right). Dark blue: unprocessed areas; grey: open water. The highest value of the backscatter coefficient are observed for multi-year ice (ice that has survived at least one summer), shown in green or yellow. This pair of images shows how the sea ice situation can differ from year to year. In 1996, new and multi-year ice covered the coastal zones of Siberia where large areas of open water were apparent in the 1995 image. (CERSAT, 2011)

	<h2>The SCIRoCCo Scatterometry Handbook</h2>	<b>Ref:</b>	SCI-PUB-14-0001-v01
		<b>Issue:</b>	6
		<b>Date:</b>	10/10/2017
		<b>Proj:</b>	SCIRoCCo Scatterometer Instrument Competence Centre

Over polar oceans, values of backscatter measurements depend on the dielectric properties of the observed materials – sea water, first-year ice and multi-year ice – on their relative concentrations and on surface topography. As sea ice ages, its dielectric properties, linked to volume and surface scattering, as well as its surface roughness are modified. Sea ice characteristics are derived from backscatter levels at prescribed incidence angles ( $40^\circ$ ), and from backscatter variations with incidence angle. In summer, surface melting of sea ice changes the backscatter signature and renders interpretation of the data more difficult.

	<p>The SCIRoCCo Scatterometry Handbook</p>	Ref:	SCI-PUB-14-0001-v01
		Issue:	6
		Date:	10/10/2017
		Proj:	SCIRoCCo Scatterometer Instrument Competence Centre

### 3 ERS Scatterometer Processing

The European Remote Sensing satellite, ERS-1, was launched in July 1991. Flying on the satellite, was the first Active Microwave Instrument. When operated in Wind Scatterometer mode, the instrument acquired measurements of sea surface wind speed and direction. ERS Scatterometer (ESCAT) data have since been widely used for hurricane prediction, Numerical Weather Prediction, marine ‘nowcasting’, oceanography, hydrology and studies of the cryosphere, with societal and economic benefits in areas such as marine safety, offshore activities, ship routing, wind energy and climate change monitoring. A second Mission, ERS-2 was then launched, partly overlapping with ERS-1. ERS-2 was launched on 20 April 1995, operating until September 2011 (see also [https://earth.esa.int/web/guest/news/-/asset\\_publisher/G2mU/content/ers-satellite-missions-complete-after-20-years-7895](https://earth.esa.int/web/guest/news/-/asset_publisher/G2mU/content/ers-satellite-missions-complete-after-20-years-7895))

The ESCAT research mission was well prepared with aircraft campaigns, including the setup of the RENE campaign for Calibration and Validation (Cal/Val), the development of a Geophysical Model Function (GMF) and initial preparations for user applications, such as the near-real-time (NRT) availability of the scatterometer winds. Nevertheless, initial comparisons of the ESCAT winds with other wind information were affected by large inconsistencies. This led to the development of novel analytical techniques using the measurement space of ESCAT, which confirmed the expected internal consistency of the ESCAT measurements and the low noise, but also provided an improved characterisation of the sensitivity to wind speed and direction, resulting in improved GMFs. Moreover, the visualisation of the ESCAT measurement space provided insights into the nonlinear wind retrieval problem, which has subsequently been improved, aided the discrimination of sea ice and water, and provided important insights into wind quality control.

The ESCAT wind Cal/Val also led to the development of the triple collocation methodology, which is now widely used in satellite algorithm development. The lessons learnt from ESCAT were readily applied to the NASA scatterometer missions at the Ku-band and provided similar benefits, leading to improved rain screening and wind datasets. ESCAT has also been successfully applied to soil moisture, sea ice and snow characterisation, leading to operational applications. ESCAT’s heritage has also been important in the development of the Advanced Scatterometer (ASCAT) on MetOp for the Eumetsat Polar System (EPS). The EPS Second Generation ASCAT (ASCAT-SG) is now being designed, where the ESCAT C-band static fan beam concept is being maintained due to its great success. This may well lead to over 40 years of C-band fan beam scatterometer data, which will be a tremendous resource for climate applications for studying wind climatologies, air–sea interactions, atmospheric processes, etc. The demand for the unique ESCAT data and services will therefore remain high in the years to come.



	<h2>The SCIRoCCo Scatterometry Handbook</h2>	<b>Ref:</b>	SCI-PUB-14-0001-v01
		<b>Issue:</b>	6
		<b>Date:</b>	10/10/2017
		<b>Proj:</b>	SCIRoCCo Scatterometer Instrument Competence Centre

### 3.1 The ERS Active Microwave Instrument (AMI)

The Active Microwave Instrument (AMI) was one of the main instruments carried on-board ERS-1 and ERS-2. The AMI incorporated two separate radars, a Synthetic-Aperture Radar (SAR) operating in image or wave mode, and a Wind Scatterometer. The Earth's surface was illuminated by three antennas and backscattered energy is received either to derive data on wind fields and wave spectra, or to produce high resolution images. The operational requirements are such that each mode needs to be operated exclusively, but the Wind and Wave Modes are also capable of interleaved operation, in so-called 'Wind/Wave Mode'.

The scatterometers on ERS-1 and ERS-2 (here denoted ESCAT) were identical and each had three antennae that illuminated the ocean surface from three different azimuth directions (e.g., Stoffelen, 1998). These beams illuminate a 500 km-wide swath as the satellite moves along its orbit, and each provide measurements of radar backscatter from the sea surface on a 25 km grid and separated by only a short time delay; see Fig. 3.2.1. A point on the ocean surface would be hit first by the fore beam, then by the mid-beam and soon after by the aft beam. Since this provided three measurements to determine two parameters, i.e. wind speed and direction, the ESCAT wind retrieval problem is overdetermined in principle. Moreover, the dominant harmonic azimuth dependence of the radar backscatter is a double harmonic (Long, 1986), which is ideally sampled by three azimuth angles  $45^\circ$  apart, enabling rather constant wind direction sensitivity of the ESCAT instrument. It was therefore anticipated (Attema, 1991) that this measurement geometry would generally result in (only) two opposite wind vector solutions and some residual information.

	<p>The SCIRoCCo Scatterometry Handbook</p>	Ref:	SCI-PUB-14-0001-v01
		Issue:	6
		Date:	10/10/2017
		Proj:	SCIRoCCo Scatterometer Instrument Competence Centre

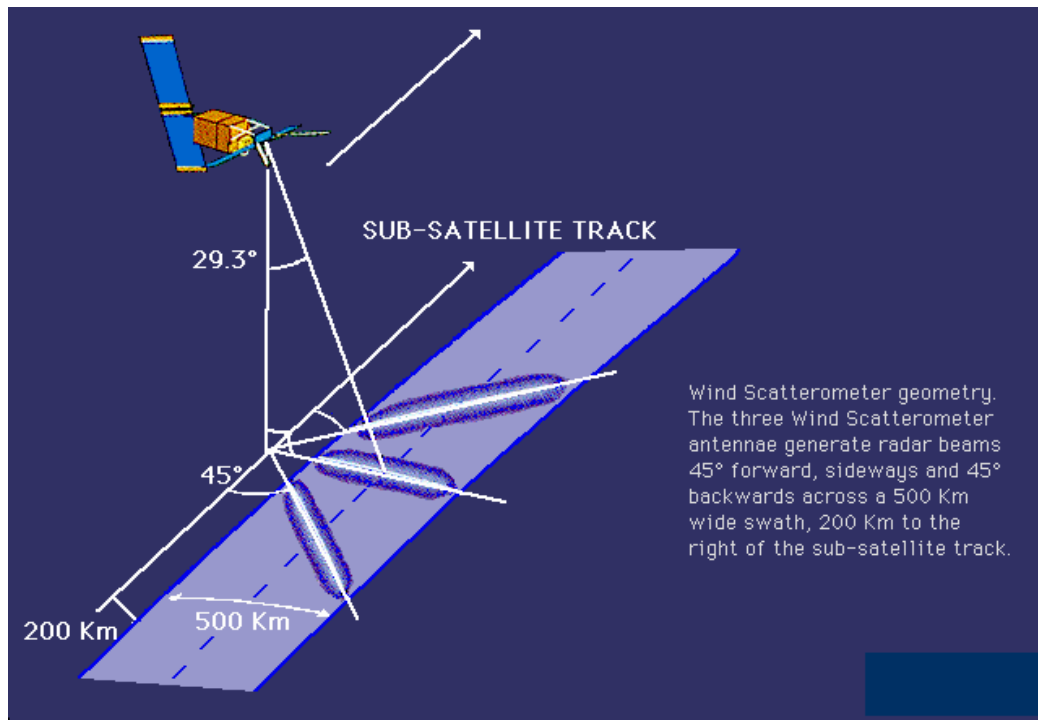


*Figure 3.1.1. ERS wind scatterometer geometry (source: ESA web site).*

Based on the available technology, the C-band wavelength was chosen for the ERS microwave mission. With hindsight, this was a very fortunate choice as it provided sufficient wind sensitivity and little sensitivity to rain effects. Several campaigns were conducted to prepare the ESCAT mission (e.g. PROGRESS and TOSCANE).

### 3.2 Towards a geophysical interpretation of the ESCAT backscatter data

Long (1986) developed empirical GMFs, that is a function used to match backscatter measurements with the measurement geometry and local wind conditions. Inversion of this GMF at each WVC revealed two wind vector solutions. As the satellite propagates along its orbit it thus produced a swath of WVCs with ambiguous winds, so that statistical techniques that exploited prior information on the spatial structure of the surface wind field were developed to resolve these ambiguities (e.g. Offiler, 1987).

Cavanié et al. (1986) made a 3D plot, where radar cross sections of the fore beam were plotted on the horizontal ( $x$ ) axis, those of aft beam on the other horizontal ( $y$ ) axis and mid-beam backscatter on the vertical ( $z$ ) axis, as depicted in Fig. 5. They realised that due to wind speed and direction sensitivity, a two-parameter manifold or surface should

	<h1>The SCIRoCCo Scatterometry Handbook</h1>	Ref:	SCI-PUB-14-0001-v01
		Issue:	6
		Date:	10/10/2017
		Proj:	SCIRoCCo Scatterometer Instrument Competence Centre

emerge in such a 3D space. Stoffelen (1998) set out to make cross sections through this surface in order to observe whether the measured backscatter triplets would indeed follow a manifold and whether the manifold was well described by CMOD2. This led to a true revolution in scatterometry, as described below.

The expected coherence in the measurement data was found and indeed the backscatter triplets are arranged in close proximity to a conical surface, as depicted in Fig. 3.1.2. The major axis of the ‘cone’ corresponds to variations in wind speed, whereas the minor axes represent changes in wind direction, confirming a basic sensitivity to the near-surface wind vector over the world’s oceans (Stoffelen, 1997a, 1998).

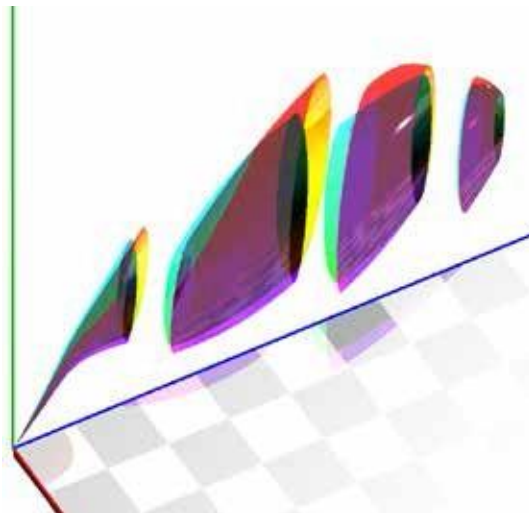


**Figure 3.2.2.** Depiction of the CMOD5.N GMF manifold at the outer ESCAT swath in measurement space spanned by the backscatter measurements of the fore antenna (red axis), the mid antenna (green axis) and the aft antenna (blue axis). The colours indicate the wind direction (red 0°, green 120°, blue 240°, all with reference to the mid-beam). The GMF is split at wind speeds of 10 m s<sup>-1</sup>, 20 m s<sup>-1</sup> and 30 m s<sup>-1</sup>, respectively, to reveal its internal structure. (Vogelzang & Stoffelen, 2012)

The actual shape of the manifold has been characterised to high precision and the GMF has been improved accordingly (Stoffelen, 1998). The resulting C-band GMF, called CMOD5.N (Hersbach et al., 2007), is also used for Synthetic Aperture Radar (SAR; Portabella, 2002) and ASCAT wind retrieval (Stoffelen & Anderson, 1997a).

The measured triplets are spread across the ideal conical manifold and this spread has been characterised in detail by Stoffelen & Anderson (1997a). Later, Portabella & Stoffelen (2006) modelled this spread in the ERS data and found that at high winds it is mainly determined by radar (speckle) noise, but at low winds by local wind variability. Since the fore, mid- and aft beams sample a WVC slightly differently, due to their different sampling sequences and footprint

	<h1>The SCIRoCCo Scatterometry Handbook</h1>	<b>Ref:</b>	SCI-PUB-14-0001-v01
		<b>Issue:</b>	6
		<b>Date:</b>	10/10/2017
		<b>Proj:</b>	SCIRoCCo Scatterometer Instrument Competence Centre

shapes, variable winds may cause the mean wind in the spatially integrated radar footprint over a WVC to be slightly different for each of the three beams. This effect is particularly relevant for low winds, as these show the highest relative variation in surface backscatter. The inconsistency in the spatial collocation of fore, mid- and aft beams and the resulting backscatter uncertainty due to local (sub-WVC) wind variability has been called ‘geophysical noise’ by Portabella & Stoffelen (2006).

In the cross sections (as in Fig. 3.1.3) occasional triplets are seen that lie almost in the middle of the cone (i.e. along its major axis) and rather far away from the wind GMF manifold as measured by the nominal noise parameters. These triplets do not correspond to good-quality winds and are rejected after wind retrieval by a Quality Control (QC) step. For ERS and ASCAT, about 0.5% of data over the open ocean (Portabella et al., 2011) could be rejected as being unlikely wind triplets. The same QC methodology has been applied to the NASA Scatterometer (NSCAT; Figa & Stoffelen, 2000) and SeaWinds instruments at the Ku-band with great success (Portabella & Stoffelen, 2001, 2002). At this wavelength about 5% of open-ocean WVCs are rejected by the QC procedure, most often due to rain clouds.

	<h1>The SCIRoCCo Scatterometry Handbook</h1>	Ref:	SCI-PUB-14-0001-v01
		Issue:	6
		Date:	10/10/2017
		Proj:	SCIRoCCo Scatterometer Instrument Competence Centre

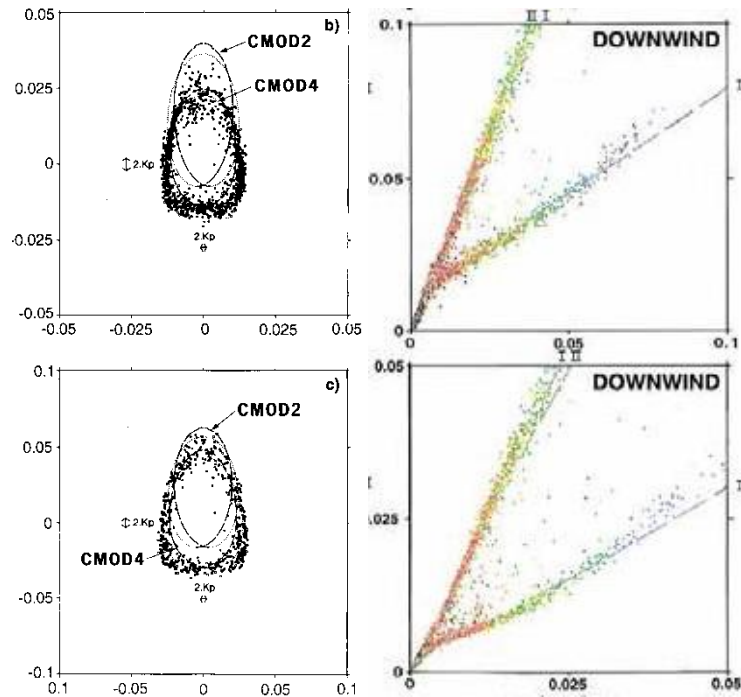


**Figure 3.2.3.** Cross sections through the manifold in the ESCAT measurement space (see Fig. 5) across the manifold (left panels) and along its main axis (right panels). (© AMS, Stoffelen & Anderson, 1997a)

It was also noted that in cross sections across the cone (Fig. 3.1.3, left panels) the measurements appear to be triangular in shape. Stoffelen & Anderson (1997a) realised that prior knowledge of this particular shape could be used in the wind retrieval in order to avoid irregularities (attractors) in the retrieved wind directions. They found a rather simple transformation of the backscatter measurement space that results in a circular manifold. A circular manifold has constant prior probability of each wind direction and is straightforward in the wind retrieval. Later, Stoffelen & Portabella (2006) noted that the wind retrieval in the transformed measurement space with a circular GMF manifold is regular since it results in a wind vector sensitivity that is rather smooth and constant. However, while the transformation works well for ESCAT-type scatterometers, constant wind vector sensitivity cannot be obtained for rotating pencil-beam scatterometers. So, due to rain and measurement geometry rotating pencil-beam Ku-band scatterometers are difficult to handle, but the experiences with ESCAT resulted in unprecedented-quality retrievals for QuikScat and OceanSat-2 (Stoffelen et al., 2013; Vogelzang et al., 2011). Table 1 provides evidence of the high accuracy of the scatterometer products based on ESCAT heritage.

*Table 3.1.2. Wind component error standard deviations with respect to the (different) scales resolved by the different scatterometer wind products as obtained by triple collocation. The lower the buoy error, the better the scatterometer product resolves the buoy scales, and thus the higher the resolution. (© AGU, Vogelzang et al., 2011)*

Dataset	Buoy		ECMWF		Scatterometer	
	$\epsilon_v$ (m s <sup>-1</sup> )	$\epsilon_v$ (m s <sup>-1</sup> )	$\epsilon_v$ (m s <sup>-1</sup> )	$\epsilon_v$ (m s <sup>-1</sup> )	$\epsilon_v$ (m s <sup>-1</sup> )	$\epsilon_v$ (m s <sup>-1</sup> )
ASCAT-12.5	1.21	1.23	1.54	1.55	0.69	0.82
ASCAT-25	1.24	1.30	1.42	1.45	0.65	0.74
SeaWinds – KNMI	1.40	1.44	1.19	1.27	0.79	0.63
SeaWinds – NOAA	1.39	1.41	1.20	1.30	1.20	1.04

The final advance in the geophysical interpretation of the ESCAT backscatter data was its use to model sea ice and to discriminate between water and sea ice surfaces. Just like wind over water, sea ice has a very particular signature in the measurement space. Sea ice surfaces are generally isotropic with varying roughness. Indeed, sea ice points lie on a line in measurement space, where the coordinate along the line depicts sea ice roughness (De Haan & Stoffelen, 2001). Subsequently, Bayesian methods were used to compute the probability of water in the WVC (Belmonte Rivas & Stoffelen, 2011) (Belmonte Rivas et al., 2012). This method, first developed for ESCAT, is now also in use for the QuikScat, OceanSat-2 and ASCAT scatterometers.

Besides the advances inspired by the ESCAT measurement space, the ERS era brought other innovations as well. The first was ocean calibration by NWP model wind fields (Stoffelen, 1998), which is still applied today to obtain interbeam backscatter calibration and the highest-quality ASCAT winds (Verspeek et al., 2012). Another statistical assessment showing the high quality and consistency of the ESCAT and ASCAT instruments and wind retrievals was provided by Hersbach (2008); the collocation plot in Fig. 3.1.4 was produced after calibrating both ESCAT and ASCAT data to the ECMWF model.

Another innovation was in triple wind collocation (Stoffelen, 1998), which is used today for ASCAT wind quality assessment (see Table 3.1.1), but also in several other Earth observation disciplines, such as quality assessments of soil moisture, sea surface temperature, sea ice drift and altimeter wave height data.

 <b>scirocco</b> scatterometer instrument competence centre	<h2>The SCIRoCCo Scatterometry Handbook</h2>	Ref:	SCI-PUB-14-0001-v01
		Issue:	6
		Date:	10/10/2017
		Proj:	SCIRoCCo Scatterometer Instrument Competence Centre

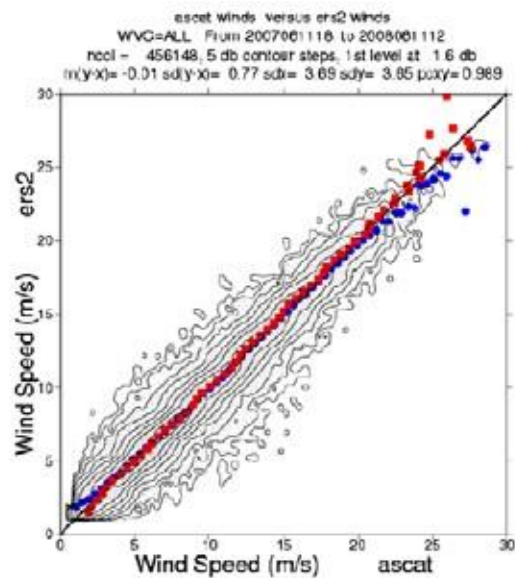


**Figure 3.2.4.** Joint distribution of collocated ESCAT and ASCAT winds with a Pearson correlation of 98.9% and standard deviation of differences of 0.77 m s<sup>-1</sup>. The blue dots depict the average ERS-2 wind speed in a 1 ms<sup>-1</sup> ASCAT wind speed bin, conversely, blue dots are average ASCAT wind speeds in an ERS-2 bin. (From Hersbach, 2008)

Together, NWP Ocean Calibration (NOC) and triple collocation essentially tie the scatterometer winds to the global buoy wind network and at the same time provide statistical evidence of biases in the NWP model (e.g. ECMWF). NOC and triple collocation are performed routinely to assess the stability of scatterometer winds over time (see [www.knmi.nl/scatterometer](http://www.knmi.nl/scatterometer)). Since the global moored buoy wind network is considered as an absolute reference, the combination of triple collocation and NOC may also be used to intercalibrate scatterometers, in particular ESCAT and ASCAT, with the objective of obtaining decadal scatterometer wind time series. These procedures could thus be applied to obtain a high-quality Fundamental Climate Data record for the ESCAT data.

The excellent statistical verification of both ESCAT and ASCAT winds was corroborated by the inspection of wind maps such as the one shown in Fig. 2.2.1 (see [www.knmi.nl/scatterometer](http://www.knmi.nl/scatterometer)). The spatially smooth wind vectors from the High-Resolution Limited Area Model, shown in blue and purple, depict a cold northerly flow on the left, adjacent to a warmer southerly flow on the right (the amount of purple increases with wind speed). The scatterometer winds from ERS-2 at around 12:00 GMT on 24 November 1999 in the Norwegian Sea (indicated in red) show much more structure and detail. Note that the grey-shaded Meteosat IR image is coherent with the scatterometer winds, with wind convergence patterns lining up well with cloud patterns, revealing details of the local meteorological conditions.

	<h2 style="text-align: center;">The SCIRoCCo Scatterometry Handbook</h2>	Ref:	SCI-PUB-14-0001-v01
		Issue:	6
		Date:	10/10/2017
		Proj:	SCIRoCCo Scatterometer Instrument Competence Centre

Since C-band scatterometers are much less affected by rain than Ku-band scatterometers, the representation of deep tropical convection will be much improved. However, there may still be issues of concern due to effects of splash, i.e. rain droplets roughening the sea surface, or wind downbursts. The latter are due to air cooled by melting and evaporating precipitation, thus increasing its mass density and falling to the sea surface, where the air is deflected in the horizontal direction, often in a circular outflow pattern. The horizontal extent of downburst patterns is generally much larger than that of the associated rain patterns.

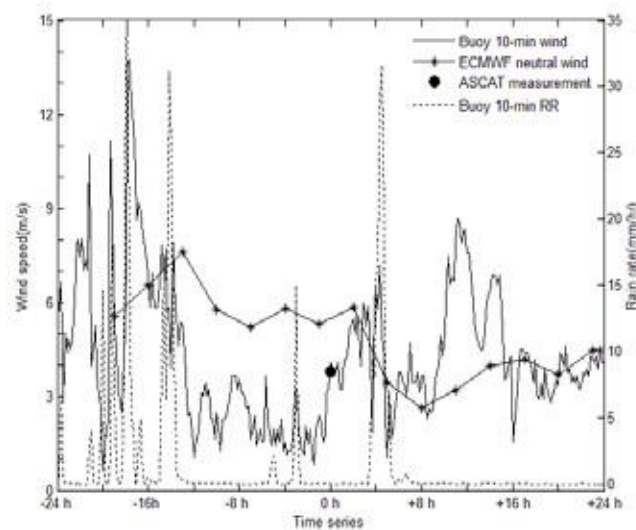


**Figure 3.2.5.** Wind speed (left axis) and rain rate (right axis) as functions of time at a rainy buoy location as explained in the legend. Time is centred around an ASCAT overpass (black dot) where the reference ECMWF forecast winds have base time at  $-25$  h. (Portabella et al., 2011)

Figure 3.1.5 shows a representative example of moored buoy winds in the tropics in the presence of rain. Wind shifts as large as  $10 \text{ m s}^{-1}$  are often associated with local rain. However, convective areas also show wind shifts when no rain is measured at the buoy. This is most likely because the horizontal extent of downburst areas is larger than those of rain areas. ASCAT winds are variable in convective areas, but prove a reasonable representation of the local buoy winds, given the rather high wind variance in the spatial representation difference of buoy and ASCAT. Triple collocation shows that the ECMWF model winds are clearly further away from the buoy winds, as expected, given the rather smooth wind fields in such convective areas (Portabella et al., 2011). It may be clear that convective processes in the tropics have a rather large effect on the surface winds and air–sea interaction processes, but also on vertical exchange in the atmosphere and tropical circulation. It remains a challenge today to assimilate the full spatial detail as measured by a scatterometer into NWP models. Therefore, process studies using scatterometer data will remain necessary in order to exploit scatterometer data to the full.



	<p>The SCIRoCCo Scatterometry Handbook</p>	Ref:	SCI-PUB-14-0001-v01
		Issue:	6
		Date:	10/10/2017
		Proj:	SCIRoCCo Scatterometer Instrument Competence Centre

In summary, the advances inspired by the ESCAT measurement space revolutionised not only the ESCAT wind retrieval and application methodology, but also those of all other wind scatterometers.

### 3.3 The ERS-2 scatterometer ground processors

As written above, the scatterometer on board ERS-2 is a real aperture pulsed radar. Due to the limited bandwidth of the on-board anti-aliasing filter, the satellite needs to be yaw-steered in order to minimize the Doppler frequency shift on the received echo signal.

Due to gyroscopes malfunction, a new attitude and orbit control system is used on-board ERS-2 since the beginning of 2001. The new piloting mode of the spacecraft, termed zero-gyro mode (ZGM), does not use any of the gyroscopes. The remaining attitude sensors (a Digital Earth Sensor and a Digital Sun Sensor) are used to pilot the spacecraft. While the pitch and roll attitude angles have almost nominal values, the yaw angle can exhibit large variations around its nominal yaw-steering mode (YSM) value.

The on-board and on-ground compensation of the Doppler frequency shift is computed to correct the shift introduced by a spacecraft in perfect YSM. When the spacecraft is not in YSM, a significant part of the spectrum of the received echo is shifted outside the pass-band of the on-ground low-pass filter, resulting in an underestimation of the backscattered energy. Moreover, yaw angle variations have obviously geometric implications.

For these two reasons, the algorithm currently used to process the scatterometer data is not able to handle data acquired in non-nominal YSM. This is the main motivation for a review of the scatterometer ground processing. As part of the reviewing process, other enhancements such as the increase of the spatial resolution of the output product were considered.

#### 3.3.1 LRDPF ground processor – the first processor

Currently, data released by ESA are only processed by ASPS. This section thus describes a processing chain not any more operationally used. However, its description is kept to show the historical evolution of the ground processing.

##### 3.3.1.1 Block diagram

The ground processing of the scatterometer data aims at computing the backscattering coefficients ( $\sigma^0$ ) from raw echo data and originally consists in the following steps: a time filtering and a detection followed by spatial averaging.

The aim of the time filtering essentially consists in increasing the signal-to-noise ratio by reducing the pass-band of the system using a low-pass filter. The on-board Doppler shift compensation only roughly compensates the

	<h1>The SCIRoCCo Scatterometry Handbook</h1>	<b>Ref:</b>	SCI-PUB-14-0001-v01
		<b>Issue:</b>	6
		<b>Date:</b>	10/10/2017
		<b>Proj:</b>	SCIRoCCo Scatterometer Instrument Competence Centre

frequency shift experienced by the signal. A finer compensation is performed on-ground in order to center the spectrum of the received signal inside the pass-band of the subsequent low-pass filter. Since the on-board anti-aliasing filter is a Bessel filter, the signal inside the pass-band is slightly attenuated. This has to be compensated before shifting the spectrum of the signal. This compensation is performed in the block called “amplitude correction”. Next the signal is demodulated (envelope detection) and the non-linearity of the on-board ADC is corrected for. The internal calibration correction and the normalization respectively aim at correcting the received signal for a varying emitted energy and removing the effect of the range and incidence angle on the received echo power.

The spatial averaging aims at further reducing the variability of the measurements by averaging the measured samples over a certain window, resulting in the final spatial resolution of the measurements.

Figure 3.2.1 presents a simplified version of the block diagram of the LRDPF processor, where only the major blocks were kept.

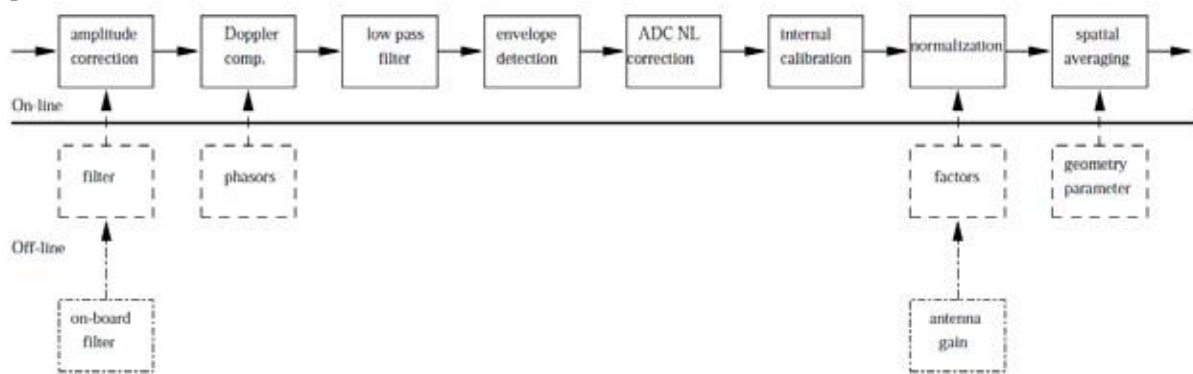


**Figure 3.3.1.** Simplified block diagram of the old processor. This includes both on-line processing, performed while processing the actual measured data and off-line processing, performed once, the resulting look-up tables being uploaded in the operational processor.

Most of the elements of this processing relied heavily on the use of look-up tables that were pre-computed for a perfectly yaw-steered spacecraft. For instance, the factor used to normalize the backscattered energy was pre-computed for a particular orbit and a particular attitude (yaw angle). This was made possible by the fact that the spacecraft always had the same attitude along all orbits. Since all the orbits having the same repeat cycle are the same, one table per repeat cycle was sufficient. Due to the fact that the spacecraft’s actual yaw angle is not a priori known and not periodic anymore, look-up tables cannot be used anymore. For these reasons, a simple adaptation of the existing satellite simulator software, used to compute these look-up tables, was not sufficient. Moreover, since the yaw angle had to be estimated from the data, a full redesign of the ground processor was deemed necessary.

	<h2 style="margin: 0;">The SCIRoCCo Scatterometry Handbook</h2>	<b>Ref:</b>	SCI-PUB-14-0001-v01
		<b>Issue:</b>	6
		<b>Date:</b>	10/10/2017
		<b>Proj:</b>	SCIRoCCo Scatterometer Instrument Competence Centre

### 3.3.2 ESACA/ASPS GROUND PROCESSOR

#### 3.3.2.1 Block diagram

The most striking difference between the block diagram of the LRDPF processor (fig. 3.2.1) and that of the ESACA/ASPS processor (fig. 3.2.2) are first the fact that the modules that pre-computed off-line some of the tables are now moved to compute the equivalent data on the fly. A second difference is the presence of the new yaw estimation module. Other differences reside in the location of the ADC non-linearity compensation step that was moved in front of all processing and the on-line computation of various filters. These differences are further discussed below.

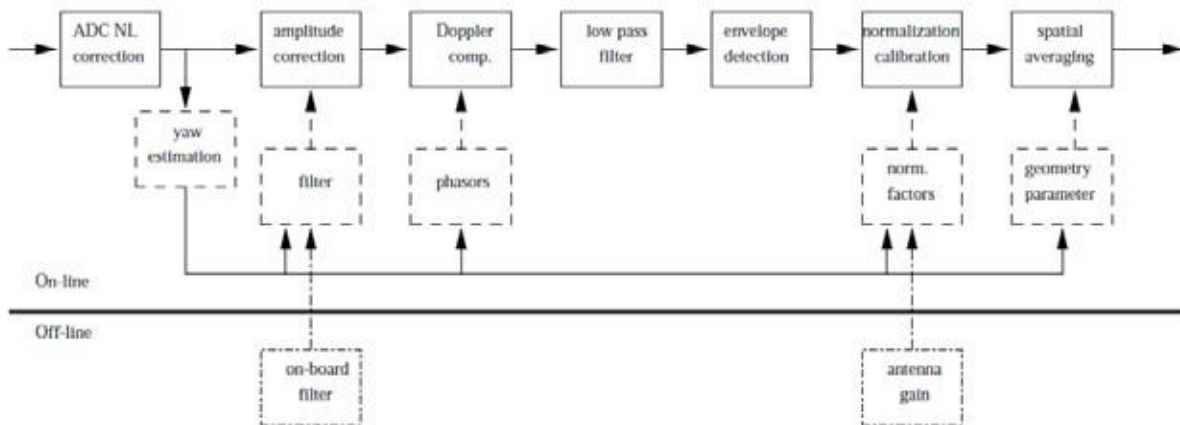


**Figure 3.3.2.** Simplified block diagram of the new processor. This processor does not use any pre-computed tables, mainly because these table could not be pre-computed.

#### 3.3.2.2 ADC non-linearity correction

The old processor performed the ADC non-linearity correction of the input data after all the filtering operations. Since the ADC is the last block influencing the signal on-board, the correction of the corresponding non-linearities should be the first operation to be performed when the signal is received on-ground. Considering that the only non-linearity of the chain resides in the on-board ADC characteristic and compensating for the ADC non-linearities, a linear chain between the acquisition and the reception of the data can be assumed.

Moreover, since all the measurements are affected by the ADC non-linear characteristic, the corresponding correction has to be performed on the internal calibration measurement too, while the old processor only corrected the measured echo data and noise power.

### 3.3.2.3 Yaw angle estimation

One of the first tasks of the new processor is to estimate the yaw angle of the spacecraft. Once the yaw angle is known, the acquisition geometry can be computed. This is then used to locate the samples on ground, compute the relative velocity of the corresponding target point and deduce the corresponding per-sample Doppler frequency shift incurred to finally compensate for it.

The yaw angle is estimated from the raw data by measuring the residual Doppler frequency shift. The yaw angle that caused the measured frequency shift is then taken as estimate for the spacecraft's yaw angle. The details of the method are explained below.

### 3.3.2.4 Residual Doppler frequency shift measurement

If the on-ground scatterers are assumed uniformly distributed, the spectrum of the returned echo can be assumed to be constant, only modulated by the spectrum of the emitted pulse. The ERS scatterometer being a real-pulse radar, it emits a square pulse modulated around 5.3GHz. The corresponding spectrum is  $\text{sinc}/x$ -shaped as illustrated in figure 3.2.3.

The Doppler frequency shift induced by the relative motion of the on-ground target and the spacecraft is not constant in range, even after the on-board Doppler compensation. Hence, instead of a simple shift of the spectrum as would be observed if the frequency shift had been constant over range, a deformation of the returned spectrum is observed as is illustrated in figure 3.2.3. The corresponding modeling is shown in figure 3.2.4.

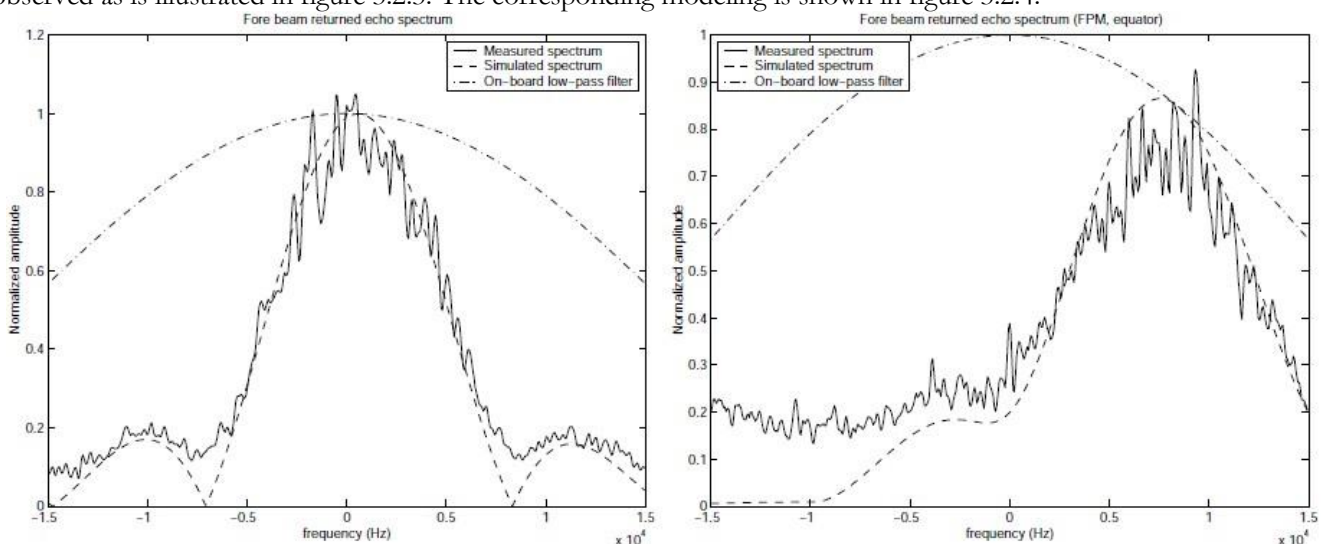


**Figure 3.3.3.** Spectrum of an echo received by the fore-beam antenna. The corresponding pulse length is 130 $\mu$ s. The  $\text{sinc}/x$  model is superposed to the real measurement and shows a close match (left). The transmittance of the on-board anti-aliasing filter is also depicted. The graph on the right shows the spectrum of a pulse acquired when the spacecraft was in fine pointing mode (FPM) at the equator. The

frequency shift is obvious, as is the deformation of the spectrum due to the range-dependent frequency shift. The superposed model does not take aliasing into account, which explains the differences.

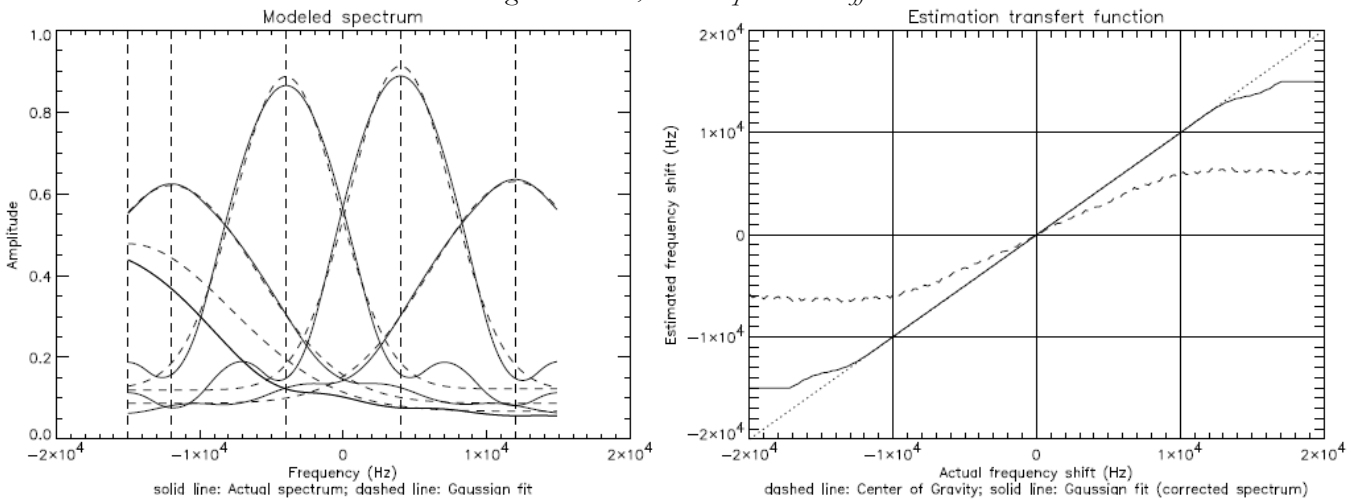


**Figure 3.3.4.** Modelling of the returned spectrum (left). Different across-track evolutions of the Doppler frequency shift are considered. The best matching Gaussian is superimposed on the corresponding spectrum. Validation of the estimation of the Doppler shift (right).

The mean Doppler frequency shift is measured by computing the best-fit of a Gaussian window onto the spectrum of the received echo. The considered model function is

$$m(f) = ae^{-\frac{(f-f_d)^2}{2\sigma^2}} + n$$

where  $a$  is the amplitude,  $\sigma$  is the standard deviation of the Gaussian,  $n$  is modeling the additive noise and  $f_d$  is the estimated mean Doppler frequency shift. This estimate is more robust than the one based on the computation of the center of gravity of the spectrum, particularly when, due to the frequency shift, a major part of the spectrum is shifted outside the anti-aliasing filter bandwidth. The estimation of the mean Doppler frequency shift given for a range-dependent linearly varying Doppler frequency shift is depicted in figure 4. While the Gaussian-fit-based estimator correctly estimates the frequency shift, up to a shift of about 12 kHz, the center of gravity estimator is highly biased due to the asymmetry of the spectrum.

### 3.3.2.5 Computation of the yaw angle from the frequency shift

There exists no closed form expression of the Doppler frequency shift for elliptical orbits over an ellipsoidal earth. Therefore, two simplified models were considered. The first model makes the assumption that the relative velocity between the satellite and the Earth target is independent of the yaw angle and yields the following expression for the Doppler frequency

$$f_{\text{Doppler}} = \frac{2 v_r}{\lambda} \sin\theta \sin(\zeta - \alpha)$$

where  $v_r$  is the relative velocity between the satellite and the Earth target,  $\theta$  is the elevation angle and  $\alpha$  is the squint angle of the antenna (0 for a bore-side looking antenna) and  $\zeta$  is the yaw angle.

The second model considered is drawn from the previous equation and make the assumption of a circular orbit. The following expression is obtained

$$f_{\text{Doppler}} = \frac{2 v_{sc}}{\lambda} \sin \theta \cos a [1 - (\omega_e / \omega)(\cos \beta \sin \Psi \tan a + \cos \Psi)]$$

where  $v_{sc}$  is the velocity of the spacecraft along the orbit,  $\lambda$  is the radar wavelength,  $\theta$  is the elevation angle,  $a$  is the angle between the azimuth plane and the plane formed by the spacecraft position and velocity,  $\omega_e$  is the Earth's rotation rate,  $\omega$  is the spacecraft orbital rotation,  $\beta$  is the argument of latitude (angle measured between the ascending node and the spacecraft position in the orbit plane from the Earth's center) and  $\Psi$  is the orbit inclination measured from the Earth spin vector to the orbit rate vector. The two last equations and are invertible and can yield a closed-form expression of the yaw angle in function of the mean Doppler frequency shift.

Figure 3.2.5 presents a comparison of the various approximations to the true Doppler frequency shift w.r.t. the value obtained by simulation along the orbit. The simulation consists in computing the various quantities involved in the expression of the definition of the Doppler frequency shift

$$f_d = \frac{2 f_t}{c} (\vec{v}_{sc} - \vec{v}) \cdot \vec{r}_1$$

where  $f_t$  is the carrier frequency,  $c$  is the speed of light,  $v_{sc}$  is the velocity vector of the satellite,  $v$  is the velocity vector of the target on Earth and  $r_1$  is the unit vector from the target on Earth to the satellite. The Doppler frequency shift compensation applied on-board is also taken into account in the simulated value. The best approximation seems to be the one deduced from the first expression for  $f_{\text{Doppler}}$  above.

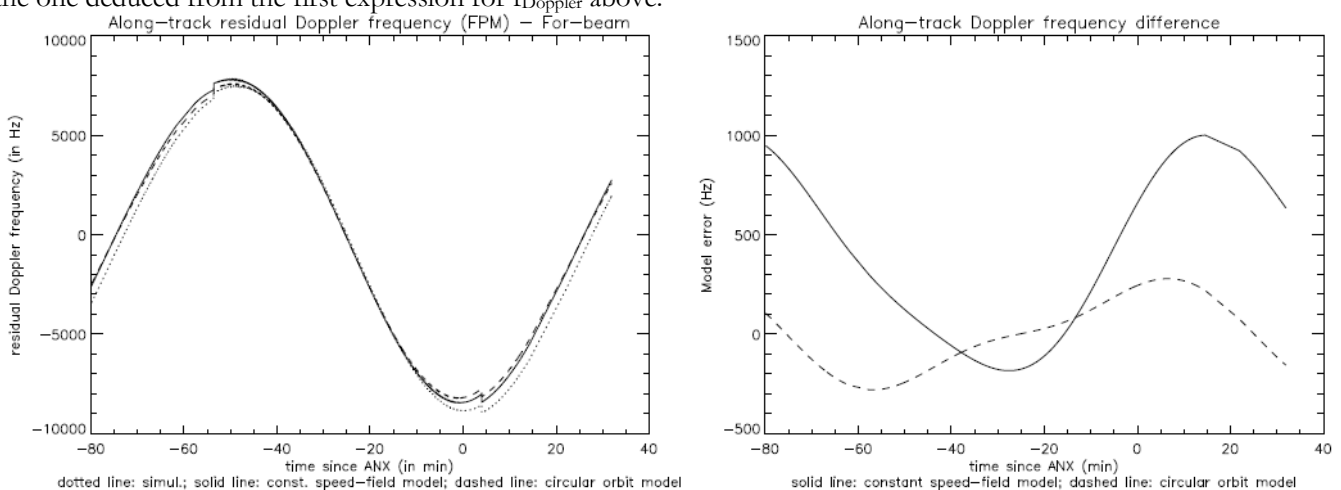


**Figure 3.3.5.** Comparison between the different models and the true value for the residual Doppler frequency shift along an orbit. The satellite pointing was perpendicular to the absolute flight direction (so-called Fine Pointing Mode — FPM) and the yaw error w.r.t. YSM

thus varies from  $-4^\circ$  to  $+4^\circ$ , is zero at the poles and maximum at the equator. The discontinuities in the graphs are due to a discontinuity in the Doppler compensation function applied on-board. Solid line: the true value from the simulator; dotted line: the residual Doppler frequency shift deduced from the second expression for  $f_{Doppler}$  above; dashed line: the residual Doppler frequency shift deduced from the first expression for  $f_{Doppler}$  above. The right graph presents the difference of Doppler frequency shift given by corresponding model with the theoretical value.

The estimated yaw angle is used to correct the data, i.e. to apply a frequency shift in order to compensate for the induced Doppler frequency shift. The yaw angle is also used to re-compute the actual measurement geometry in order to correctly locate the measurement point on ground and to compute the correct normalization factor. Figure 3.2.6 illustrates the effect of an error of  $2^\circ$  on the yaw angle. The mis-estimated yaw angle causes the displacement of the measured samples by several kilometers. The radiometric effect through the geometry, i.e. on the normalization factor is however very limited.

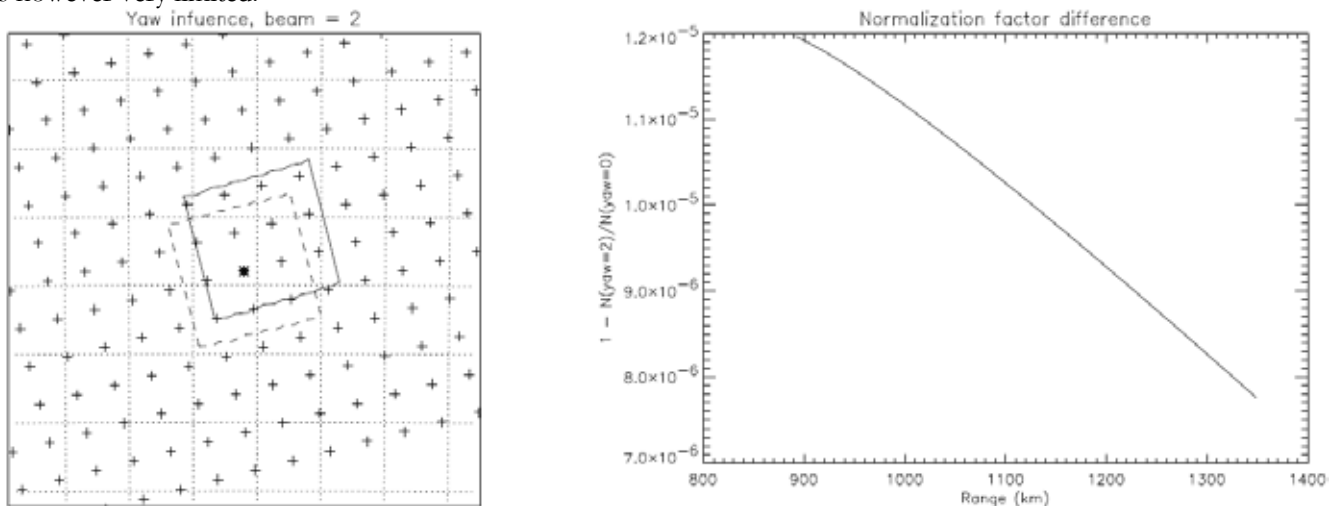


**Figure 3.3.6:** Effect of an error of  $2^\circ$  on the yaw angle. Left: geometrical effect, right: radiometric effect.

### 3.3.2.6 Data processing

#### 3.3.2.6.1 Data filtering

There are two main filters involved in the processing of the data. The first filter, called “amplitude correction filter” aims at compensating the characteristic of the on-board anti-aliasing filter while the second filter, called “low-pass filter” aims at reducing the pass-band of the measurement system in order to increase the signal-to-noise ratio.

#### 3.3.2.6.2 Amplitude correction filter

This filter is implemented in the time domain, and hence only partially compensates the spectral characteristic of the on-board anti-aliasing filter as is illustrated in the following figure.

	<p>The SCIRoCCo Scatterometry Handbook</p>	Ref:	SCI-PUB-14-0001-v01
		Issue:	6
		Date:	10/10/2017
		Proj:	SCIRoCCo Scatterometer Instrument Competence Centre

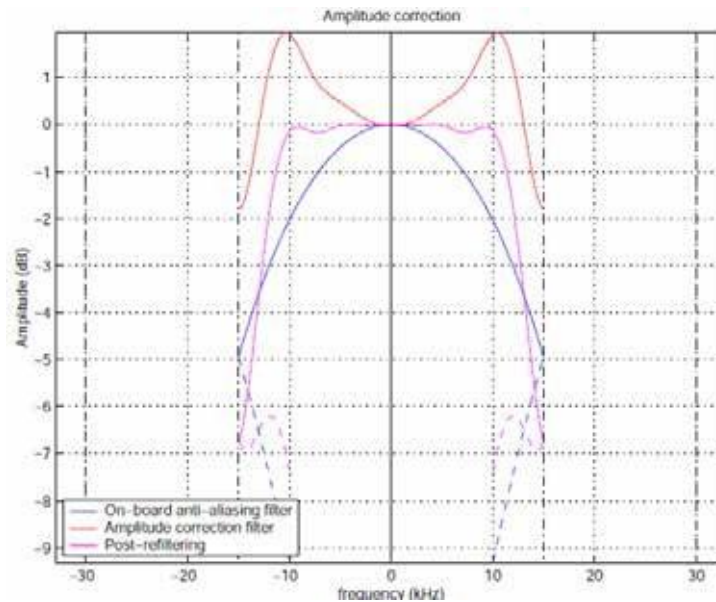


*Figure 3.3.7: Amplitude correction filter and the resulting overall spectral behavior*

### 3.3.2.6.3 Low pass filtering —Butterworth filter

The aim of this filter is to keep only the useful signal while rejecting the other components (considered as noise) in order to increase the signal to noise ratio. The filter currently chosen is a low-pass 4th order Butterworth filter with cut-off frequencies (-3 dB) of 8.8 kHz and 6.4 kHz for respectively the Mid and Fore/Aft beams.

### 3.3.2.6.4 Noise subtraction

In reality, the target signal plus the receiver noise power is measured rather than the target signal alone. To improve the instrument accuracy the receiver noise power is measured separately and then subtracted from the sum of both.

The noise correction is performed by subtracting from each target sample of one measurement block, the averaged noise power estimate  $P_N$  corresponding to that measurement block:

$$s_c(n) = s_u(n) - P_N$$

where  $s_u$  is the square of the averaged uncorrected target signal and  $s_c$  the corresponding noise-corrected target signal.  $P_N$  is the average of the noise power estimates of the corresponding measurement block.

### 3.3.2.6.5 Normalization/calibration

The signal power at the output of the block averaging is proportional to the instantaneous power. It has to be related to the backscattered coefficient to obtain the  $0^0$ . This operation is called normalization and is separated in three factors: a first factor that takes into account the varying power of the transmitted pulse obtained through internal calibration, yielding a time-dependent value; a second factor that takes into account the geometry of the sensor and the gain of



	<h1>The SCIRoCCo Scatterometry Handbook</h1>	<b>Ref:</b>	SCI-PUB-14-0001-v01
		<b>Issue:</b>	6
		<b>Date:</b>	10/10/2017
		<b>Proj:</b>	SCIRoCCo Scatterometer Instrument Competence Centre

the antenna yielding a sample-dependent factor called normalization factor; and a last factor that accounts for the other gains, including the ADC conversion factor and is constant.

Internal calibration consists in injecting a small fraction of the transmit signal directly into the receiver low noise amplifier. During each block, four internal calibration measurements take place. These calibration measurements are received on-ground as I and Q samples. On-ground, these I and Q samples are first corrected for I/Q imperfection (gain imbalance, non-orthogonality and DC-bias. The samples corresponding to one calibration pulse are averaged together (using a weighting function) to give the energy of that pulse. The energies of the 4 pulses corresponding to one measurement block are averaged together. In order to reduce quantization noise, the result is further low pass filtered across several measurement blocks by an exponential (recursive) filter to yield the average peak power of the transmitter.

The normalization factor  $f_N$  from the echo power profile to the surface backscatter coefficient is

$$f_N(n) = \frac{R^3 \sin \theta}{G_{el}^2(\theta_{el})}$$

Where R is the slant range, i.e. the distance between the spacecraft and the target point,  $\theta$  is the incidence angle at the target point and  $G_{el}$  is the one-way antenna gain in the beam elevation plane at the look-angle  $\theta_{el}$ .

### 3.3.2.6.6 Spatial filtering

Spatial filtering denotes here the operation of computing the spatially averaged  $\sigma_0$  values at the node locations and is the final step of the processing. The spatial filtering is used to make the impulse response of the scatterometer system match the requirements. The spatial averaging at the node location can be seen as a spatial filtering of irregularly sampled data, the filtered result being resampled at the node locations.

### 3.3.2.6.7 Sea-ice probability estimation

In order to discriminate  $0^0$  values measured over ice, the probability that a node contains sea-ice is computed. That probability is computed using a state-less algorithm described in. The probability is to be understood in a Bayesian framework, i.e. as a limiting case of the frequency of occurrence on the training set used. A probability close to 1 means that sea-ice is present and a probability close to 0 means only open water is present. A value in between means it is a mixed node containing more or less sea-ice.

### 3.3.2.7 Quality control and monitoring

The overall system behavior must be monitored to check the product confidence. For this purpose, several control parameters are computed and delivered in the source packet headers.

	<p>The SCIRoCCo Scatterometry Handbook</p>	Ref:	SCI-PUB-14-0001-v01
		Issue:	6
		Date:	10/10/2017
		Proj:	SCIRoCCo Scatterometer Instrument Competence Centre

### 3.3.2.7.1 High power amplifier monitoring

A possible cause to missing transmit pulses is HPA-arcng, leading to temporary shutdown of the amplifier. During these time intervals only noise will be recorded, hence the derived  $\sigma_0$  values are invalid and must be detected as such. This can be achieved by monitoring the HPA. The HPA-shutdown detection procedure is based on the difference in energy level of the calibration pulses during normal HPA operation and shutdown. The averaged energy of the samples of the calibration pulses of a measurement block is compared to a threshold value, a flag being raised if the latter is greater. When performing the spatial averaging, the flags of the samples contributing to a node are summed together, yielding the number of “arcng” samples that contributed to a particular node.

### 3.3.2.7.2 Power spectrum monitoring

When the frequency shift of the received signal is too high, an accurate compensation is not possible as a significant part of the energy of the signal was likely filtered-out by the on-board low-pass filter. To assess that, the spectrum of the received signal is monitored and a QC flag is raised when the spectrum is outside pre-defined boundaries.

### 3.3.2.7.3 Doppler compensation monitoring

The Doppler compensation performed (on-board and on-ground) is subject to errors, in particular due to the yaw control inaccuracy. This may lead to a shift of the spectrum out of the low pass filter passband and thus to an alteration of the signal to noise ratio. The required monitoring is performed on the power spectrum at the input of the low-pass filter by computation of the centre of gravity and the standard deviation of the power spectrum of the signal, averaged over a monitoring interval.

### 3.3.2.7.4 Internal calibration level monitoring

The internal calibration level is monitored by computing, for each beam, a control parameter based on the energy of the internal calibration pulses samples.

### 3.3.2.7.5 Number of valid samples contributing to a node

On the principle, the value of  $\sigma^0$  at the nodes is the spatial average of the measurements. However, in some circumstances such as close to instrument mode change, or close to instrument shut down or instrument power up, fewer samples may be available. This is monitored by reporting how many samples contributed to the  $\sigma_0$  value of a particular node.

### 3.3.2.7.6 Noise power monitoring

Too much noise power may be an indication interferences are occurring. Sources of interferences may be other radars on ground, and more generally other RF equipment on ground. In addition to measuring the noise power in order to subtract it from the received power, the level of the received noise power is monitored and flagged when exceeding a pre-defined threshold indicating interferences occurred. The effect of interferences is difficult to remove as their

	<h1>The SCIRoCCo Scatterometry Handbook</h1>	Ref:	SCI-PUB-14-0001-v01
		Issue:	6
		Date:	10/10/2017
		Proj:	SCIRoCCo Scatterometer Instrument Competence Centre

(temporal) behavior may not be the same as the expected white noise from the black-body radiation of the earth and the thermal noise. Figure 7 illustrates the effect of a high noise power interference.

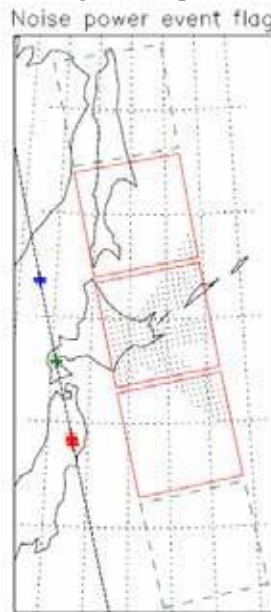


**Figure 3.3.8:** Illustration of a high noise power event. The blue, green and red crosses indicate the on-orbit position at which a high noise power event was detected in respectively the aft, mid and fore beams. The red squares indicated the affected products and the black dots indicate the position of the affected nodes.

	<p>The SCIRoCCo Scatterometry Handbook</p>	Ref:	SCI-PUB-14-0001-v01
		Issue:	6
		Date:	10/10/2017
		Proj:	SCIRoCCo Scatterometer Instrument Competence Centre

## 4 Soil Moisture

The objective of this section of the “Scatterometer Handbook” is to give an overview of the soil moisture retrieval approach based on the ERS-1/2 scatterometers. The demand of global area representative soil moisture measurements is highlighted in a short introduction. The capability of space-borne scatterometers to provide the demanded global soil moisture measurements is discussed based on the theoretical considerations regarding microwave scattering properties of natural media. Furthermore, a comprehensive introduction to the TU-Wien soil moisture retrieval approach is given, concentrating on the main aspects of the retrieval to derive soil moisture estimates from backscatter data, recorded by the European C-band scatterometer missions. Finally, the reader will be pointed to the large number of applications, by providing an overview of selected applications and references to further literature.

### 4.1 Introduction

Soil moisture is a crucial driver for many physical, chemical and biological processes and feedback loops taking place at the land surface and within the atmosphere. Accordingly, soil moisture is a variable that is required in many interdisciplinary scientific and operational applications with the objective to develop, evaluate or improve geophysical models. Most generally speaking, soil moisture, also often referred to as soil water content, is the amount of water stored in the unsaturated soil zone (Hillel, 2014). Soil moisture is commonly given in volumetric units expressed by the ratio of the volume of water in the soil to the total volume of soil constituted of dry soil, air and water. While the mineral- and organic matter contents of the soil usually vary only over very long time scales, the soil water content and, inversely related to it, the air volume fraction are highly variable. Since soil moisture is arguably one of the most important parameters for the understanding of interactions between the hydrosphere, biosphere and the atmosphere, it is essential to know how much water is stored in the soil and how it varies in space and time. Traditional in-situ measurement techniques like time-domain reflectometry, gravimetric or radiological methods basically record point-scale measurements of soil moisture. However, the application of point-scale soil moisture measurements is inappropriate for obtaining a deeper understanding of global interactions and processes of the Earth’s climate system. Temporal and spatial soil moisture variations on a global perspective are exclusively provided by space-borne remote sensing instruments such as scatterometers. Space-borne scatterometers are capable to assess area representative soil moisture measurements indirectly by recording the power of the backscattered signal which is affected by the soil’s dielectric constant. A number of methods for retrieving soil moisture values from the ERS-1/2 scatterometers were developed in the late 1990s (e.g. Magagi and Kerr, 1997; Pulliainen et al., 1998; W. Wagner et al., 1999a, 1999b). In the context of this document, we will concentrate on the method proposed by Wagner et al. (1999b) for estimating remotely sensed soil moisture on a global scale by utilising ERS scatterometer data.

	<p>The SCIRoCCo Scatterometry Handbook</p>	Ref:	SCI-PUB-14-0001-v01
		Issue:	6
		Date:	10/10/2017
		Proj:	SCIRoCCo Scatterometer Instrument Competence Centre

## 4.2 Theoretical background

As already mentioned, the capability of the ERS-1/2 scatterometers, hereafter referred to as ESCAT, to measure soil moisture from space is based on the distinct dielectric behaviour of water in the microwave frequency domain. The distinct dielectric behaviour of water is manifested in the permanent dipole moment due to the triangular structure of the H<sub>2</sub>O molecules. As a consequence, amongst all natural media only water shows orientational polarisation when an electromagnetic field is applied, resulting in a high dielectric constant. In general, the dielectric constant ( $\epsilon$ ) of a material is a complex number, consisting of a real part ( $\epsilon'$ ) and an imaginary part ( $\epsilon''$ ). In Figure 4-1, the relative permittivity ( $\epsilon_w'$ ) and the dielectric loss factor ( $\epsilon_w''$ ) of pure water, at a temperature of 20°C, is illustrated as a function of the frequency of the applied electromagnetic field.

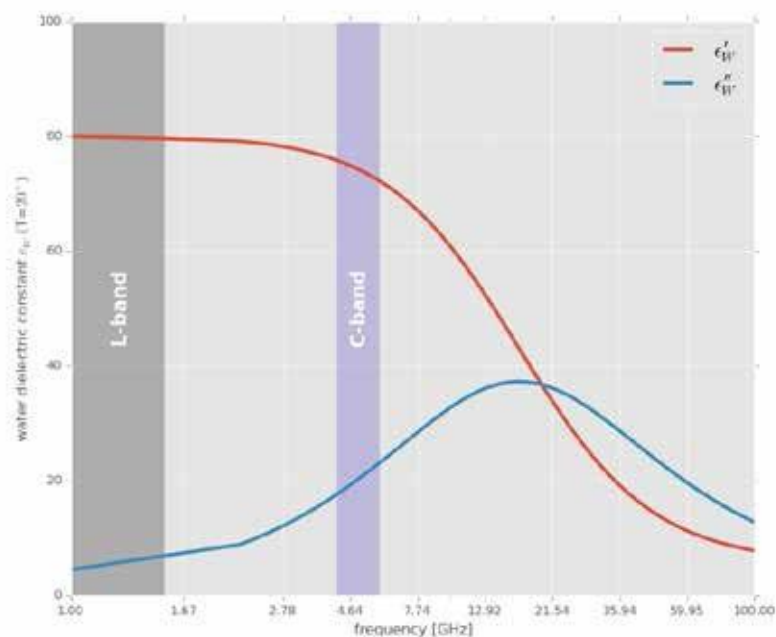


Figure 4-1: Dielectric constant of pure water at 20°C as a function of frequency

Especially the lower frequency part of the microwave spectrum, ranging from 1 to 10 GHz, is dominated by high dielectric constants. Therefore, the water content of soil, vegetation, snow and ice is a crucial driver for the response of natural landscapes when exposed to the microwave radiation. In the following section, the dielectric behaviour of soil and vegetation with respect to soil moisture is discussed.

	<h1>The SCIRoCCo Scatterometry Handbook</h1>	<b>Ref:</b>	SCI-PUB-14-0001-v01
		<b>Issue:</b>	6
		<b>Date:</b>	10/10/2017
		<b>Proj:</b>	SCIRoCCo Scatterometer Instrument Competence Centre

### 4.2.1 Dielectric constant of soils

According to Hillel (2014), soil is defined as the “weathered and fragmented outer layer of the Earth’s terrestrial surface formed initially through disintegration, decomposition, and recombination of mineral material contained in exposed rocks by physical, chemical, and biological processes”. In general, a soil medium consists of three phases: the solid phase which forms the soil matrix consisting of soil particles; the liquid phase, representing the water in the soil and the gaseous phase, which is called the soil atmosphere made up of air pockets (see Figure 4-2).

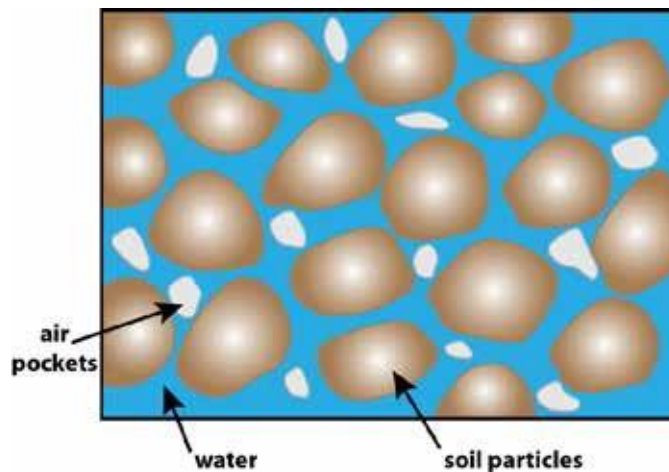


Figure 4-2: Cross section of a soil medium

In the absence of water, the microwave dielectric constant of soil ( $\epsilon_{\text{Soil, dry}}$ ) is almost independent of temperature and frequency, with values ranging from  $2 \leq \epsilon'_{\text{Soil, dry}} \leq 4$  and  $\epsilon''_{\text{Soil, dry}} < 0.05$  (Ulaby et al., 2014). Dobson et al. (1985) determined  $\epsilon'_{\text{Soil, dry}}$  as a function of the dry soil bulk density  $\rho_b$  by an empirical fit to field data resulting in the expression:

$$\epsilon'_{\text{Soil, dry}} = (1.01 + 0.44\rho_b)^2 \quad \text{Eq. 4-1}$$

On the other hand, the dielectric behaviour of wet soil is strongly related to the amount of water held in the soil medium. Water contained in the soil medium is usually divided into two fractions according to the forces that are acting on the water molecules (Dobson et al., 1985; Hallikainen et al., 1985). Water molecules within the first few molecular layers surrounding the soil particles are referred to as bound water, because they are tightly held by the particles due to the influence of matric and osmotic forces. The matric force affecting the water molecules decreases rapidly with increasing distance from the soil particle. As a consequence, water molecules located several molecule layers away from the particles are able to move freely within the medium and hence are referred to as free water. The separation of water into bound and free fractions in the soil medium is based on rather arbitrary criteria for the transition point between bound and free water layers. However, it is apparent that with increasing fractions of bound water in the soil medium the dielectric constant of wet soil  $\epsilon_{\text{Soil, wet}}$  decreases. Accordingly, the dielectric constant of wet soil depends on the textural composition of the soil medium which is directly proportional to the surface area of

	<h1 style="text-align: center;">The SCIRoCCo Scatterometry Handbook</h1>	<b>Ref:</b>	SCI-PUB-14-0001-v01
		<b>Issue:</b>	6
		<b>Date:</b>	10/10/2017
		<b>Proj:</b>	SCIRoCCo Scatterometer Instrument Competence Centre

the soil particles. The textural composition of soil can be conveniently separated into three textural fractions or separates, namely: sand, silt and clay. The separates characterise the size range of particles in the soil medium. With reference to the definition of the U.S. Department of Agriculture (USDA) [Figure 4-3], the particle size of sand is defined in the range of 2000µm down to 50µm, silt from 50µm to 2µm and clay from 2µm downwards.

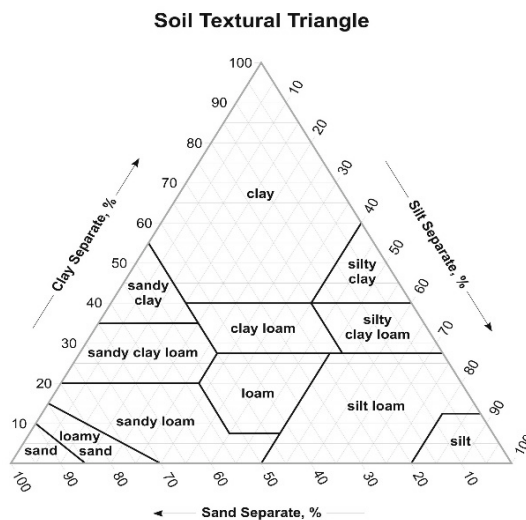


Figure 4-3: Soil texture triangle according to USDA definition

[from [http://www.nrcs.usda.gov/wps/portal/nrcs/detail/soils/edu/?cid=nrcs142p2\\_054311](http://www.nrcs.usda.gov/wps/portal/nrcs/detail/soils/edu/?cid=nrcs142p2_054311)]

Hallikainen et al. (1985) developed an empirical model to succinctly describe the dielectric behaviour of wet soil for different microwave frequencies. The empirical dielectric model is based on the soil textural composition with respect to sand (Sa) and clay (Cl) components in percent of weight and the volumetric water content (W). The general formula of the polynomial fit is:

$$\epsilon_{\text{Soil, wet}} = (aa_0 + aa_1SSaa + aa_2CCCC) + (bb_0 + bb_1SSaa + bb_2CCCC) * WW + (cc_0 + cc_1SSaa + cc_2CCCC) * WW^2 \quad \text{Eq. 4-2}$$

Model parameters  $a_{0-2}$ ,  $b_{0-2}$ ,  $c_{0-2}$  were estimated for a set of different microwave frequencies ranging from 1.4 to 18 GHz separately for the real and the imaginary part of the dielectric constant  $\epsilon_{\text{Soil, wet}}$  (Hallikainen et al., 1985, Table II). Figure 4-4 illustrates the dielectric behaviour of loamy soil, 40% sand and 20% clay, as a function of the volumetric soil moisture. It can be seen that that the dielectric constant  $\epsilon'_{\text{Soil, wet}}$  increases from about 2.4 for dry soil conditions to 46 for a saturated soil surface. In contrast to dry soil, the dielectric constant of wet soil is dependent on the soil temperature, especially on temperatures below 0°C, because frozen water impedes orientational polarisation. However, some water within the soil medium does not freeze even at temperatures around -50°C. Therefore,  $\epsilon_{\text{Soil, wet}}$  shows some dependency on the moisture content before freezing. Nevertheless, it should be stated that the dielectric properties of completely dry soil and wet, frozen soil are very similar.

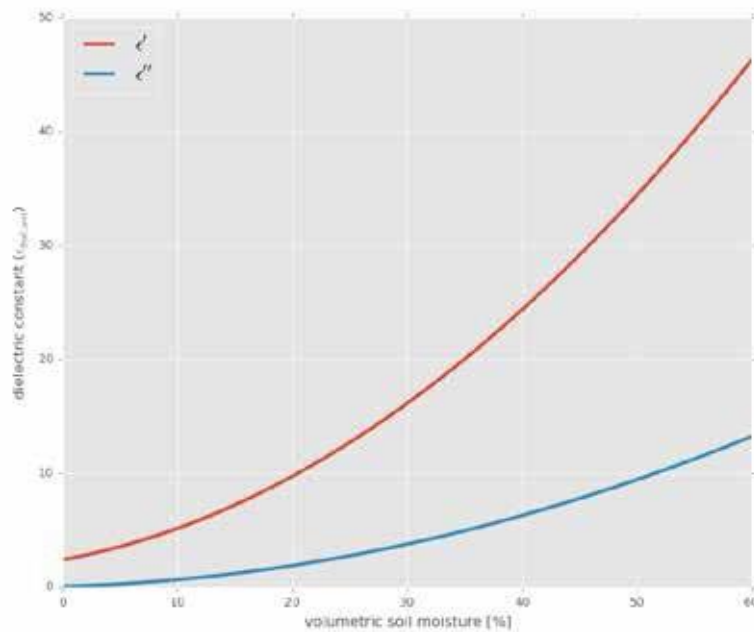


Figure 4-4: Dielectric constant of loamy soil (40% Sand, 20% Clay) as a function of the volumetric soil moisture

#### 4.2.2 Dielectric constant of vegetation

Vegetation can be physically described as a dielectric mixture made up of discrete dielectric inclusions such as leaves, stalks, branches and trunks within a host material (air). Dielectric measurements of oven-dried samples of several vegetation types show that the real part of the dielectric constant  $\epsilon'_v$  is between 1.5 and 2 and  $\epsilon''_v$  is below 0.1 (El-rayes and Ulaby, 1987; Ulaby and El-rayes, 1987). Water makes up about 80% to 90% of the weight of leaf-like plants and even woody plants contain more than 50% of water. Therefore, the dielectric constant of vegetation  $\epsilon_v$  increases strongly with the water content. El-rayes and Ulaby (1987) and Ulaby and El-rayes (1987) developed an empirical formula to model  $\epsilon_v$  as a function of the volumetric water content of the vegetation matter alone. The model distinguishes between bound water that is held tightly by the organic compounds and free water that can move within plants with relative ease. A slightly modified version of this model, known as the Michigan microwave canopy scattering model, was presented by Ulaby et al. (1990) accounting for temperature effects. This scattering model suggests that for a gravimetric vegetation moisture content of around 80%, the dielectric constant  $\epsilon'_v$  takes on values above 40.



### 4.2.3 Backscatter from natural land surfaces

In remote sensing, when the term scattering is used explicitly, it usually refers to the random distortion of coherent electromagnetic waves by surfaces and structures similar to or larger in size than the radar wavelength. In most cases, an electromagnetic wave impinges from above upon the boundary between two semi-infinite media. It should be noted that any interface separating two media with different dielectric properties affects an electromagnetic wave incident on it. The electromagnetic wave interacts with the atoms in the lower medium, causing the atoms to become small electromagnetic oscillators, which themselves radiate waves in all directions. As a consequence, some energy will be radiated towards the upper as well as towards the lower dielectric medium [see Figure 4-5 (a)].

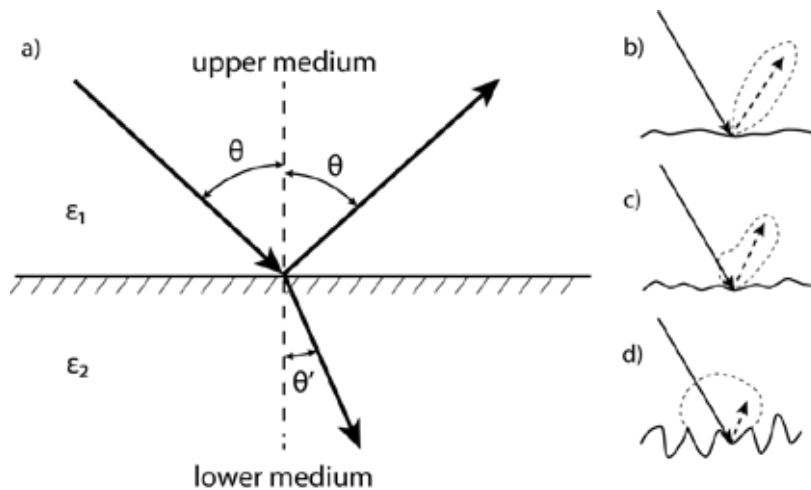


Figure 4-5: Scattering mechanism/pattern

a) at a flat interface between two media

b-d) at an increasingly rough interface between two media

If the interface between two media is perfectly flat, the incident wave will excite the atomic oscillators at a relative phase in a way that the resulting field consists of two plane waves. In the upper medium a plane wave is observed at an angle equal to the angle of incidence  $\theta$ , referred to as reflected wave. According to Fresnel's law, a second wave is perceived in the lower medium, referred to as refracted wave, at an angle equal to:

$$\theta' = \arcsin \left( \frac{\sqrt{\epsilon_2} \sin(\theta)}{\sqrt{\epsilon_1}} \right)$$

Eq. 4-3

In terms of a uniform and homogenous lower medium, scattering only occurs at the surface interface between the upper and the lower medium and is therefore designated to surface scattering. Surface scattering is strongly affected by surface geometrical properties, which are commonly described mathematically by the so-called surface roughness and the surface height autocorrelation function. If the surface interface between two media is smooth relative to the wavelength of the incident wave, most of the radiation returned to the upper medium is in the form of a specular reflection [see Figure 4-5 (b)]. For a rougher surface, less energy is reflected in specular direction and more energy is

	<h2 style="text-align: center;">The SCIRoCCo Scatterometry Handbook</h2>	<b>Ref:</b>	SCI-PUB-14-0001-v01
		<b>Issue:</b>	6
		<b>Date:</b>	10/10/2017
		<b>Proj:</b>	SCIRoCCo Scatterometer Instrument Competence Centre

scattered diffusely in the upper medium [see Figure 4-5 (c)]. With respect to a very rough surface, there is essentially no specular reflection and most of the energy is isotropically scattered from the surface interface [see Figure 4-5 (d)]. Whether a surface interface appears to be smooth or rough is dependent on the wavelength  $\lambda$  of the incident wave. Following the so-called Rayleigh criterion, a surface is classified as rough if the root mean square (r.m.s) height ( $h$ ) satisfies  $h > \lambda/8 \cos(\theta)$ . So far the focus was on the scattering mechanism/pattern of an electromagnetic wave impinging on the boundary of two homogenous dielectric media. However, in case of an inhomogeneous medium, scattering can occur within the medium itself referred to as volume scattering. The propagating wave loses parts of its energy due to absorption and scattering in all directions caused by dielectric discontinuities within the medium. With respect to this effect, for inhomogeneous media, the size, shape and distribution of the individual dielectric discontinuities is more critical than the roughness of the surface boundary.

When an electromagnetic wave impinges on a bare soil surface, a portion of the energy is scattered at the boundary surface in all directions and the rest is transmitted forward into the soil. The penetration depth of the transmitted wave is limited by absorption and scattering losses in the inhomogeneous soil medium. In general, the penetration depth of C-band microwaves, which are used by ESCAT, into the soil varies from about 10 cm under dry conditions to less than 1 cm under wet conditions, if only absorption losses are considered. In most circumstances the layer accessible to C-band microwaves is about 0.5 cm to 2 cm thick (Schmugge, 1983; Ulaby et al., 1978). Hence, scattering from a bare soil surface is determined mainly by the dielectric properties of the upper few centimetres of the soil, controlled by the soil moisture content in this layer, and by the geometrical structure or roughness of the soil surface. Some scattering may arise due to inhomogeneities within the soil medium, but this may be ignored in favour of the surface scattering contribution. However, it should be noted that an increase in the dielectric constant of the soil amplifies the ability of the soil surface to reradiate electromagnetic waves. As a consequence, the backscattered signal and the soil moisture content are positively correlated. It was found empirically, that the power of the backscatter signal, expressed in Decibel (dB), and the volumetric soil moisture content are quasi-linearly related (Champion and Faivre, 1997; Ulaby et al., 1996).

With respect to the scattering of vegetated surfaces, vegetation canopies are inhomogeneous media comprising scattering elements with many different sizes, shapes, orientations, and dielectric properties. Usually, the vegetation constitutes 1% or less of the canopy volume (Attema and Ulaby, 1978) and the penetration depth is in the order of meters (Ulaby et al., 1982). Scattering is mainly caused by the dielectric discontinuities within the canopy volume known as volume scattering. However, scattering from low vegetation canopies also consists of surface scattering contributions emerged by the underlying bare soil surface. Hence, scattering from vegetation is a complex phenomenon and elaborated models have been developed to model the backscatter signal in terms of vegetation and soil surface. A more detailed discussion about scattering characteristics of vegetated surfaces is given in the following chapter, outlining the applied vegetation correction to retrieve soil moisture estimates.

	<p>The SCIRoCCo Scatterometry Handbook</p>	Ref:	SCI-PUB-14-0001-v01
		Issue:	6
		Date:	10/10/2017
		Proj:	SCIRoCCo Scatterometer Instrument Competence Centre

### 4.3 The TU-Wien soil moisture model

The soil moisture retrieval model developed at the Vienna University of Technology (TU-Wien) is a physically motivated empirical change detection method. Initially, the model has been developed step by step over selected study areas across the globe. Vegetation effects on the radar backscatter of ESCAT were studied in detail over the Iberian Peninsula (Wagner et al., 1999a). A first realisation of the soil moisture retrieval model was published by Wagner et al. (1999b), demonstrating the capability of ERS-1 ESCAT data for monitoring soil moisture over the Canadian prairies. Additionally, a method was developed over the Ukraine to estimate the water content in the soil profile from topsoil moisture content as provided by ESCAT (Wagner et al., 1999). The first global application of the soil moisture retrieval model was presented by Scipal et al. (2002) utilising ERS-1/2 ESCAT data ranging from 1992 to 2000. Later on, the soil moisture retrieval model, initially tailored to ESCAT observations, was successfully transferred to the Advanced Scatterometer (ASCAT) on-board of the MetOp satellites (Bartalis, 2009; Naeimi et al., 2009) with a number of enhancements.

#### 4.3.1 Introduction

As already stated at the beginning, the TU-Wien soil moisture retrieval is a physically motivated empirical change detection method. The advantage of change detection over a radiative transfer model is that soil moisture can be directly retrieved from the backscatter measurements without the need of an iterative adjustment process. On the other hand, the change detection approach cannot directly separate the different contributions from soil, vegetation and soil-vegetation interactions to the observed total backscatter as in the case of the radiative transfer model. As a consequence, a multi-year radar backscatter archive is required to calibrate model parameters, used in the change detection approach, to implicitly account for land cover, surface roughness and many other effects. Therefore, full advantage is taken of the multi-incidence angle and multi-beam viewing capability of the European C-band scatterometers ESCAT and ASCAT in order to characterise backscatter variations of the Earth's land surface. For an in-depth discussion and further details about the TU-Wien soil moisture model, the reader shall be referred to Wagner (1998) and Naeimi et al. (2009). Variations of the backscatter coefficient  $\sigma^0$  are related to surface roughness, changes in vegetation and to variations in the soil water content. An important fact is that each of these factors acts on a different spatial and temporal scale. With respect to these aspects, the TU-Wien model allows the determination of model parameters from multi-year backscatter time-series to gain essential knowledge on scattering effects taking place on a certain location on the Earth's land surface. The underlying physical assumptions and empirically observed evidences can be summed up as follows:

- The incidence angle has a strong impact on the backscatter coefficient  $\sigma^0$  of natural targets. This dependency is a characteristic for roughness and vegetation, but soil moisture changes are not or only minimally affected by this circumstance.
- The incidence angle dependent backscatter coefficient  $\sigma^0(\theta)$  is decreasing or increasing with vegetation growth, whether the contribution of the soil on the ground is higher than the contribution of the vegetation

	<b>The SCIRoCCo Scatterometry Handbook</b>	<b>Ref:</b>	SCI-PUB-14-0001-v01
		<b>Issue:</b>	6
		<b>Date:</b>	10/10/2017
		<b>Proj:</b>	SCIRoCCo Scatterometer Instrument Competence Centre

canopy or conversely. Hence, the  $\sigma^0(\theta)$  time series is changing in accordance to the vegetation phenology over time.

- The vegetation phenology cycle influences  $\sigma^0$  on a seasonal scale and local short-term variability are negligible due to the low resolution of the sensor.
- The relationship between soil moisture and  $\sigma^0$ , expressed in dB, is considered to be linear.
- There are certain incidence angles  $\theta_{\text{dry}}$  and  $\theta_{\text{wet}}$  at which  $\sigma^0$  is rather stable in face of vegetation changes. These so called “crossover angles” are assumed to be  $25^\circ$  for the dry reference and  $40^\circ$  for the wet reference.
- The coarse resolution of the scatterometer admits the assumption that roughness and land cover are temporally invariant.

Hereafter, a summary will be given, addressing the major considerations of the initial developed retrieval model and the current state of the art TU-Wien soil moisture retrieval model with their mathematical formulations.

### 4.3.2 Normalisation of ESCAT backscatter measurements

In general, backscatter measurements are recorded at different azimuth and incidence angles at a given location on the Earth’s surface. In order to assure a direct comparison of backscatter measurements acquired in different measurement configurations, it is necessary to normalise each observation with respect to incidence and azimuth angle. The TU-Wien soil moisture retrieval distinguishes between incidence angle and azimuth angle normalisation, which are outlined in the following section. From a technical point of view, the instrument design of ESCAT permits observations of a location on the Earth’ surface under a range of incidence angles as well as under three distinct azimuth angles for each satellite overpass. This is possible because ESCAT is equipped with three different antennas referred to as fore-, mid- and aft-beam antennas.

#### Azimuth angle normalisation

The following paragraphs concentrate on the radar backscatter  $\sigma^0$  dependency with respect to the azimuth angle  $\varphi$ . A comprehensive discussion about this topic related to the soil moisture model can be found in Scipal (2002) and Bartalis et al. (2006). Hereafter, a condensed version of the research performed and published by Bartalis et al. (2006) is given to highlight the main considerations in deriving an azimuthal normalised backscatter  $\sigma^0$ . In most cases, the backscattering coefficient decreases rapidly with increasing incidence angle. However, the topography of the Earth’s land surface within a scatterometer footprint can alter the actual backscatter so that at various azimuthal angles, it differs significantly from the theoretical backscatter expected from a footprint, imaged under a spatially uniform and constant incidence angle. Topographical mechanisms modulating the backscatter with respect to the azimuth angle can be grouped into the following categories:

- “*Sloping Surface Backscattering Targets with Predominant Slope Orientation*”: As illustrated in in Figure 4-6, although the  $\sigma^0$  measurement is recorded at the nominal incidence angle  $\theta$ , the angle determining the backscatter is

	<h2 style="text-align: center;">The SCIRoCCo Scatterometry Handbook</h2>	<b>Ref:</b>	SCI-PUB-14-0001-v01
		<b>Issue:</b>	6
		<b>Date:</b>	10/10/2017
		<b>Proj:</b>	SCIRoCCo Scatterometer Instrument Competence Centre

actually the local incidence angle  $\theta_L$ , because of the local slope of the surface. If the size of the sloping targets is comparable to or larger than the footprint size, a plot of the backscatter versus azimuth angle will have one peak and one trough, or one lobe in a polar plot [Figure 4-7 (a)]. This should be the case for azimuthal effects from mountain ranges and the sloping marginal areas of the Antarctic or Greenlandic ice sheets. It should be noted that for a 25/50-km spatial resolution most places in the world have slope values very close to zero. The mean slope decreases with decreasing spatial resolution, while the standard deviation of the slope increases, often dramatically. Thus, at the scatterometer spatial resolution, we expect little azimuthal variation due to the large-scale slope. If on the other hand the footprint covers several sloping and spatially aligned targets that are still larger than the wavelength, backscatter will be amplified if the satellite is facing the slopes [Figure 4-7 (b) and (c)]. This is anticipated to be the case of aligned crop fields and sand dunes.

- *“Corner Reflectors with Predominant Orientation”*: In this case, local slopes of aligned scattering targets within the footprint become so steep, that a double or multiple “bounce” interaction of the radar signal becomes possible. Backscatter in certain viewing directions from a few point-like targets becomes so high that it can affect the backscatter response over the entire footprint [Figure 4-7 (d)]. This could be the case of urban areas laid out along a rectangular grid.
- *“Resonant Bragg Scattering”*: Scatterometers emit coherent electromagnetic radiation and accordingly, different emitted wave-fronts are “in phase”. When targets are comparable in size to the radar wavelength of the scatterometer with a predominant orientation, the backscattered waves are subject to constructive interference at certain incidence angles. It is likely that reflections from surface ripples on sand dunes also reinforce each other coherently (Stephen and Long, 2005).

*Figure 4-6: Scatterometer viewing geometry [from Bartalis et al. (2006)]*

	<h2 style="text-align: center;">The SCIRoCCo Scatterometry Handbook</h2>	<b>Ref:</b>	SCI-PUB-14-0001-v01
		<b>Issue:</b>	6
		<b>Date:</b>	10/10/2017
		<b>Proj:</b>	SCIRoCCo Scatterometer Instrument Competence Centre

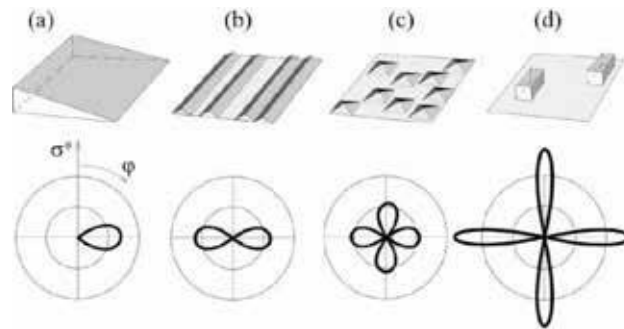


Figure 4-7: Illustration of different sloping backscatter targets and their corresponding schematic polar plots of backscatter coefficient  $\sigma^0$  versus azimuth angle  $\varphi$ . (a) Large-scale slope. (b) Sloping surface backscattering targets with predominant slope orientation of the second order. (c) Sloping surface backscattering targets with predominant slope orientation of the fourth order. (d) Corner reflectors [from Bartalis et al. (2006)]

With respect to the fore- and aft-beam antennas of ESCAT,  $\sigma^0$  are measured almost at the same time and at the same incidence angle, but at two different azimuth angles. Accordingly, backscatter differences between fore- ( $\sigma^0_f$ ) and aft-beam ( $\sigma^0_a$ ) measurements will represent a measure of the magnitude of possible azimuthal effects of a target over land.

$$\begin{aligned} \delta\delta_{AASSAA} &= \sigma\sigma^0_{ff,AASSAA} - \sigma\sigma^0_{aa,AASSAA} & \text{Eq. 4-4} \\ \delta\delta_{DDDDSSAA} &= \sigma\sigma^0_{ff,DDDDSSAA} - \sigma\sigma^0_{aa,DDDDSSAA} \end{aligned}$$

Because a target on the Earth's surface is observed during ascending and descending satellite overpasses, backscatter differences can be calculated separately for each overpass denoted by  $\delta_{ASC}$  in terms of ascending and  $\delta_{DESC}$  for the descending overpass, respectively. Figure 4-8 illustrates the mean value of backscatter differences calculated with Eq. 4-4. Very low values can be found over the tropical rainforests, whereas both mountainous and non-mountainous regions are featured by higher backscatter differences. Extremely high backscatter differences are obvious over sand desert areas like the Sahara, Takalmakan- and Arabian Desert. The first global analyses of potential azimuthal effects on the backscatter over land were performed by Scipal (2002) and further investigations were carried out by Bartalis et al. (2006). In the early stages of the development of the soil moisture retrieval (W. Wagner et al., 1999b), the azimuthal dependence of the backscatter  $\sigma^0$  was not considered. Instead, backscatter triplets, fore-/mid- and aft-beam measurements, in which the backscatter difference of  $\delta_{ASC}$  and  $\delta_{DESC}$  is greater than a defined threshold, were disregarded in the soil moisture retrieval. Although this approach reduced the variability of the backscatter in terms of different observation azimuth, substantial azimuthal effects were observed in the time series over many geographical regions. Hence, Bartalis et al. (2006) developed a method to correct for azimuthal-modulation effects, also referred to as azimuthal anisotropy, observed by ESCAT over land surface. The azimuth normalisation method is based on historically recorded data to derive the statistically expected backscatter value of a target. It is crucial to note that the degree of azimuthal anisotropy could vary depending on the incidence angle as well as with the season of the year. Accordingly, the number of possible azimuth-incidence combinations is  $6 * 19 = 114$  in the case of ESCAT.

	<h2 style="text-align: center;">The SCIRoCCo Scatterometry Handbook</h2>	Ref:	SCI-PUB-14-0001-v01
		Issue:	6
		Date:	10/10/2017
		Proj:	SCIRoCCo Scatterometer Instrument Competence Centre

Therefore, if enough historical data is available for each of the 114 combinations, backscatter measurements could be reliably normalised azimuthally by adding or subtracting a bias, representing the difference between the expected backscatter value for the azimuth-incidence combination in question and a backscatter value measured or derived at a reference azimuth angle. Furthermore, to account for seasonal changes in the magnitude of the azimuthal anisotropy, the number of azimuth-incidence-time combinations can be given by  $114 * n$ , where  $n$  denotes the number of chosen time periods. In terms of ESCAT, the lack of a statistically meaningful number of backscatter observations was found to compute robust normalisation values for all azimuth-incidence-time combinations. Consequently, a compromise solution along the lines of incidence angle and time is feasible by fitting a second order polynomial to the backscatter versus incidence angle relationship, separately for each of the six azimuth angles. In addition, a polynomial can be fitted to all the measurements, irrespective of azimuth, representing the expected backscatter of a target as function of the incidence angle. Finally, the required azimuthal normalisation biases can be calculated at any incidence angle, as the difference between each of the six azimuth polynomials and the seventh, cumulative polynomial.

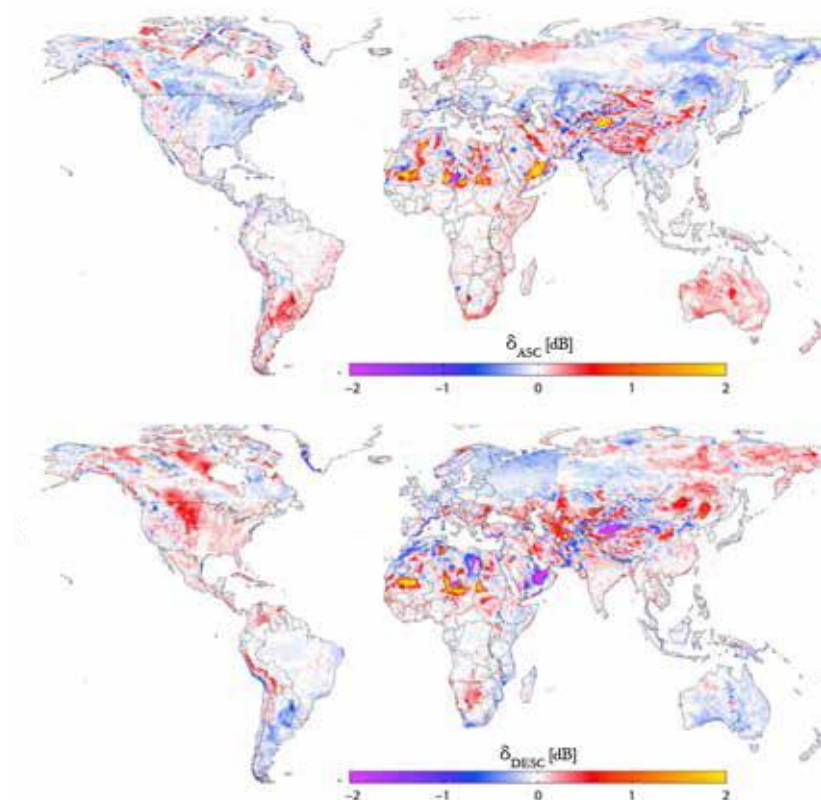


Figure 4-8: Mean of the differences between fore- and aft-beam ESCAT backscatter taken triplet-wise for ascending overpass (top) and descending overpass (bottom) [from Bartalis (2009)]

	<h1>The SCIRoCCo Scatterometry Handbook</h1>	Ref:	SCI-PUB-14-0001-v01
		Issue:	6
		Date:	10/10/2017
		Proj:	SCIRoCCo Scatterometer Instrument Competence Centre

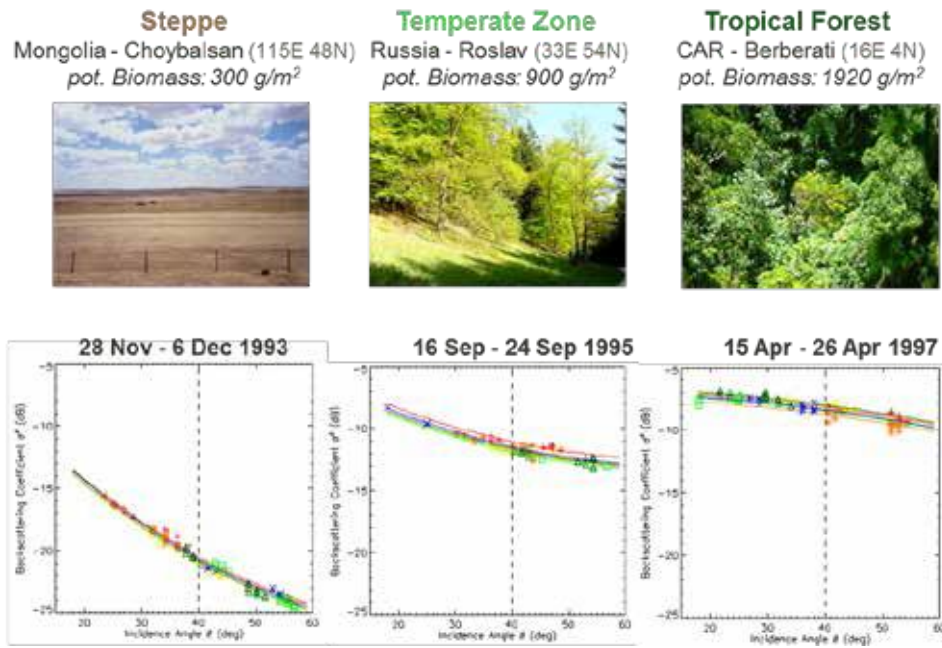


Figure 4-9: Backscatter  $\sigma^0$  as a function of the incidence angle  $\theta$  for three different biomes [from Scipal (2002)]

### Incidence angle normalisation

As already mentioned earlier in this section, the value of the backscatter coefficient  $\sigma^0$  is strongly related to the incidence angle  $\theta$ , with rapidly decreasing values for increasing incidence angles. Hence, an incidence angle normalisation method needs to be applied for each backscatter observation which will be discussed in the following paragraphs. The dependence of the backscatter  $\sigma^0$  on the incidence angle  $\theta$  is influenced by the predominant surface roughness and the amount of biomass (see Figure 4-9). Accordingly, the slope of  $\sigma^0(\theta)$  is indicative for the scattering mechanism taking place at the observed target. It was found that a second order polynomial is adequate to model the backscatter incidence angle behaviour of the Earth's land surfaces sufficiently.

$$\sigma^0(\theta, t) = \sigma^0(40^\circ, t) + \sigma'(40^\circ, t)(\theta - 40^\circ) + \frac{1}{2} \sigma''(40^\circ, t)(\theta - 40^\circ)^2 \quad \text{Eq. 4-5}$$

The key parameters in Eq. 4-5 are referred to as slope  $\sigma'(40^\circ, t)$  and curvature  $\sigma''(40^\circ, t)$  in the soil moisture retrieval model, defining the first and second derivative of  $\sigma^0(\theta)$ . It is worth noting that both parameters are a function of time  $t$  and the reference incidence angle of  $40^\circ$ . Figure 4-9 illustrates a set of second order polynomial fits to ESCAT backscatter data for different times  $t$  over different biomes, confirming the sufficiency of the proposed backscatter-incidence model. In the soil moisture retrieval model it is considered that the slope  $\sigma'(40^\circ, t)$  and curvature  $\sigma''(40^\circ, t)$  parameters are unaffected by soil moisture variations. Therefore, it is anticipated that changes in soil moisture are reflected in the magnitude of the backscatter coefficient  $\sigma^0(40^\circ, t)$  exclusively, as depicted in Figure 4-10 (a).



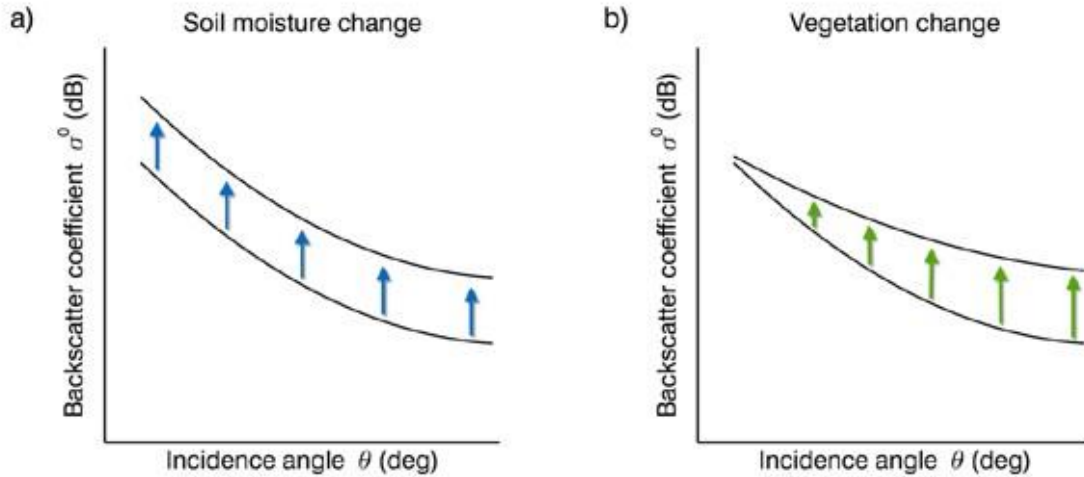


Figure 4-10: Backscatter-incidence angle behaviour with respect to a) soil moisture changes and b) vegetation changes

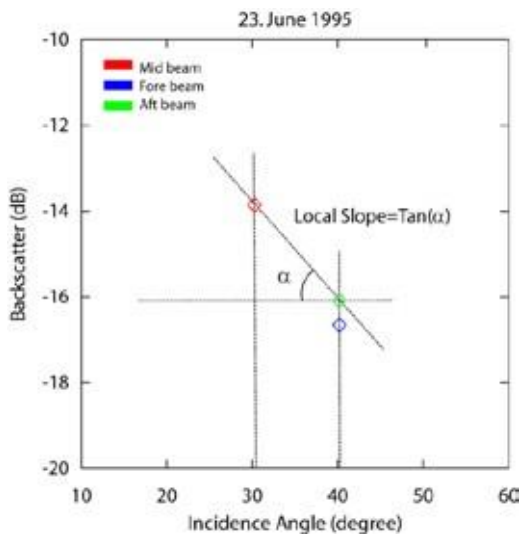
On the other hand, changes in the slope  $\sigma'(40^\circ, t)$  and curvature  $\sigma''(40^\circ, t)$  are expected to show variations in the vegetation phenology and changes in the surface roughness, as can be seen in Figure 4-10 (b). Estimates of slope  $\sigma'(40^\circ, t)$  and curvature  $\sigma''(40^\circ, t)$  are determined by utilising the multi-beam capability of ESCAT, resulting in estimates of the first derivative of the backscatter-incidence angle dependency, referred to as local slopes. Local slopes are computed as difference quotients of each backscatter triplet. To be more specific, each backscatter triplet yields two local slope estimates by computing differences between the fore- and mid-beam and between aft- and mid-beam observations as illustrated in Figure 4-11 (a) and mathematically formulated in Eq. 4-6.

$$\sigma'_{ll} = \frac{\sigma^0_{mm}(\theta_{mm}) - \sigma^0_{ff,aa}(\theta_{ff,aa})}{\theta_{mm} - \theta_{ff,aa}} \quad \text{Eq. 4-6}$$

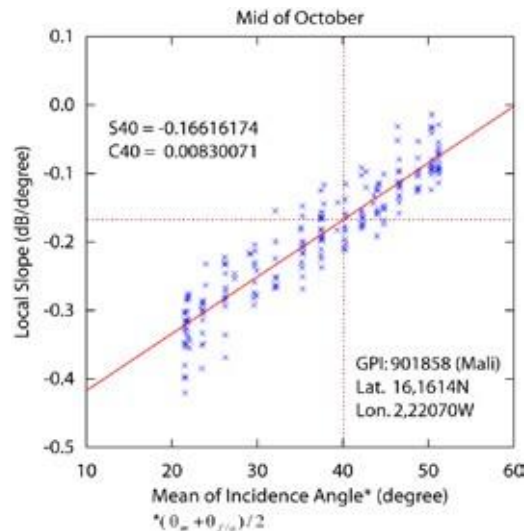
The index “m” denotes the mid-beam antenna and the index “f” or “a” for either the fore-beam or aft-beam antenna. Since the backscatter  $\sigma^0$  decreases with increasing incidence angle,  $\sigma'_{ll}$  takes on negative values with large negative values corresponding to a steep decline of the backscatter  $\sigma^0$ . The local slope  $\sigma'_{ll}$  derived from each backscatter triplet represents only an estimate of the real slope near the respective incidence angles affected by measurement noise. Hence, slope  $\sigma'(40^\circ, t)$  and curvature  $\sigma''(40^\circ, t)$  values of  $\sigma^0(\theta)$  can be obtained by fitting a regression line see Eq. 4-7, to the computed local slopes  $\sigma'_{ll}$  acquired during a particular period, as illustrated in Figure 4-11 (b).

$$\sigma'(\theta, t) = \sigma'_{ll}(40^\circ, t) + \sigma''_{ll}(40^\circ, t)(\theta - 40^\circ) \quad \text{Eq. 4-7}$$

Wagner et al. (1999a) and Scipal (2002) determined slope  $\sigma'(40^\circ, t)$  and curvature  $\sigma''(40^\circ, t)$  values for each month of the year. Consequently, 12 values of  $\sigma'(40^\circ, t)$  and  $\sigma''(40^\circ, t)$  are obtained by fitting a regression line to the computed local slopes  $\sigma'_{ll}$  of each month.



a)



b)

Figure 4-11: Illustration of the computation of slope and curvature. a) Determination of the local slope  $\sigma'_L$  b) Linear regression of the local slopes to determine slope and curvature at  $40^\circ$  incidence angle

Finally, these monthly values were interpolated by utilising empirical trigonometric functions according to

$$\sigma'(40, tt) = CC' + DD'\psi\psi(tt) \quad \text{Eq. 4-8}$$

where  $\psi(t)$  is one of 68 predefined periodic functions describing the dynamic evolution of  $\sigma'(40^\circ, t)$ . In Eq. 4-8,  $C'$  is a constant slope value and  $D'$  is the dynamic range of the slope and the empirical periodic function  $\psi(t)$ . The same procedure was applied to the curvature  $\sigma''(40^\circ, t)$ , the second derivative of the backscatter  $\sigma^0(\theta)$ . The reason for using estimates for each month of the year was robustness with respect to measurement noise, but a one-month time-window length filters high-frequency variations of vegetation growth as stated by Naeimi et al. (2009). Furthermore, in some cases, the applied empirical function  $\psi(t)$  cannot satisfactorily describe natural variations. This problem is particularly evident at the beginning of the vegetation development or vegetation dormancy onset. As a consequence, an improved slope/curvature estimation method was developed to overcome these issues. Naeimi et al. (2009) investigated the impact of the time-window length  $\tau$  on the estimation of the slope  $\sigma'(40^\circ, t)$  and curvature  $\sigma''(40^\circ, t)$ . Therefore, the slope  $\sigma'(40^\circ, t)$  parameters were calculated for different values of  $\tau$  by making use of local slope values  $\sigma'_L$  within a given time-window length  $\tau$ , centred at a specific day of the year. However, the selection of the time-window length  $\tau$  is critical. A too short time-window yields to noisy slope  $\sigma'(40^\circ, t)$  and curvature  $\sigma''(40^\circ, t)$  estimates, while a too long window filters a remarkable part of the variation (see Figure 4-12). Moreover, the time-window length  $\tau$  is also dependent on the regional climate. Hence, to overcome the challenge for the right choice of the time-window length  $\tau$ , a modified Monte Carlo simulation (Niederreiter, 1992) is used with a series of different  $\tau$  values. It is assumed that, with reference to the spatial resolution of scatterometers, the vegetation is not changing remarkably during a less than 2-week period, and the seasonal vegetation change does not take longer than 12 weeks. For a subset

	<h2 style="margin: 0;">The SCIRoCCo Scatterometry Handbook</h2>	<b>Ref:</b>	SCI-PUB-14-0001-v01
		<b>Issue:</b>	6
		<b>Date:</b>	10/10/2017
		<b>Proj:</b>	SCIRoCCo Scatterometer Instrument Competence Centre

of 27 equidistant days of the year, simulated slope values  $\sigma'(40^\circ, \tau)$  are computed by employing local slope values  $\sigma'$  located within the varying time-window length  $\tau$  centred at the specific day of the year. Hence,  $\sigma'(40^\circ, t)$  is determined as the mean of simulated  $\sigma'(40^\circ, \tau)$  values, given a large quasi-random number of  $\tau$  ranging between 2 and 12 weeks as input of the simulation. The mean calculation of  $\sigma'(40^\circ, t)$  is given in Eq. 4-9, whereas the number of evaluations performed in the Monte Carlo simulation is denoted by  $M$ .

$$\sigma\sigma'(40, tt) = \frac{1}{MM} \sum_{SS=1}^{MM} \sigma'(40, \tau_{SS}) \quad \text{Eq. 4-9}$$

The determination of the curvature  $\sigma''(40^\circ, t)$  parameter, the second derivative of  $\sigma^0(\theta)$  at  $40^\circ$  incidence angle, is performed equally by utilising the same method and values of  $\tau$ , as stated by Eq. 4-10.

$$\sigma\sigma''(40, tt) = \frac{1}{MM} \sum_{SS=1}^{MM} \sigma''(40, \tau_{SS}) \quad \text{Eq. 4-10}$$

Because the utilised Monte Carlo simulation is computed on 27 equidistant days of the year, a spline interpolation is performed in order to obtain slope and curvature values for each day of the year. As a result, a full complement of 366 slope  $\sigma'(40^\circ, t)$  and curvature  $\sigma''(40^\circ, t)$  values is used to perform the essential incidence angle normalisation of the recorded backscatter  $\sigma^0(\theta)$ . The normalisation is carried out by making use of Eq. 4-11, which is the rearranged notation of Eq. 4-5, to derive backscatter coefficients normalised to  $40^\circ$  incidence angle  $\sigma^0(40^\circ, t)$ .

$$\sigma\sigma_{SS}^0(40^\circ, tt) = \sigma\sigma_{SS}^0(\theta\theta, tt) - \sigma\sigma'(40^\circ, tt)(\theta\theta - 40^\circ) - \frac{1}{2} \sigma\sigma''(40^\circ, tt)(\theta\theta - 40^\circ)^2 \quad \text{Eq. 4-11}$$

In the TU-Wien soil moisture retrieval model, the computation of  $\sigma_i^0(40^\circ, t)$  is done separately for fore-, mid- and aft-beam observations of each backscatter triplet denoted by the subscript  $i$ . The three resulting values are averaged to obtain a time-series for each location on the Earth's surface.

$$\sigma\sigma^0(40^\circ, tt) = \frac{1}{3} \sum_{SS=1}^3 \sigma\sigma_{SS}^0(40^\circ, tt) \quad \text{Eq. 4-12}$$

Figure 4-13 shows an example of the different developed slope/curvature estimation procedures introduced by Wagner et al. (1999a), denoted by WARP4, and Naeimi et al. (2009), denoted by WARP5, for a grid point located in Kansas (U.S). The enhanced vegetation index (EVI) is used as a reference, displaying two peaks caused by farming activities in this region. Obviously, the slope function estimated by Naeimi et al. (2009) captured these rapid variations of the vegetation canopy, while these variations cannot be discriminated in the slope function determined by Wagner et al. (1999a).

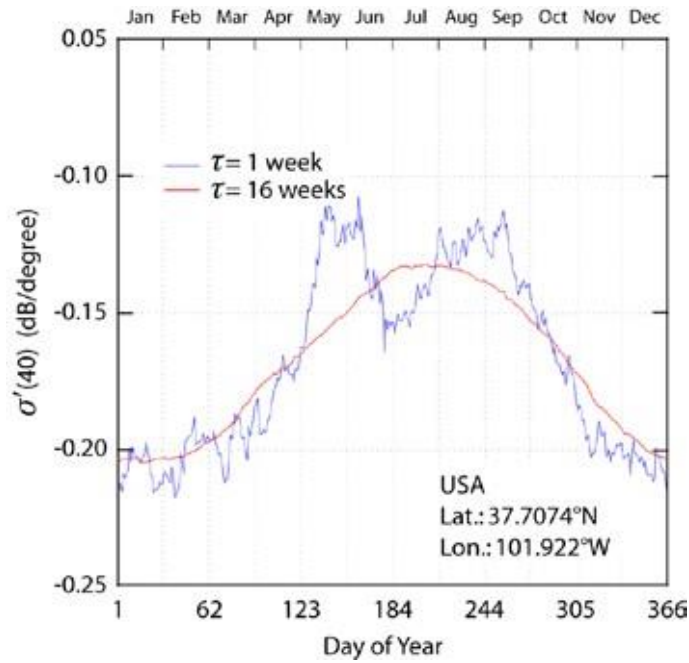


Figure 4-12: Effect of the time-window length  $\tau$  on the estimation of the slope  $\sigma'(40^\circ)$  [from Naeimi et al. (2009)]

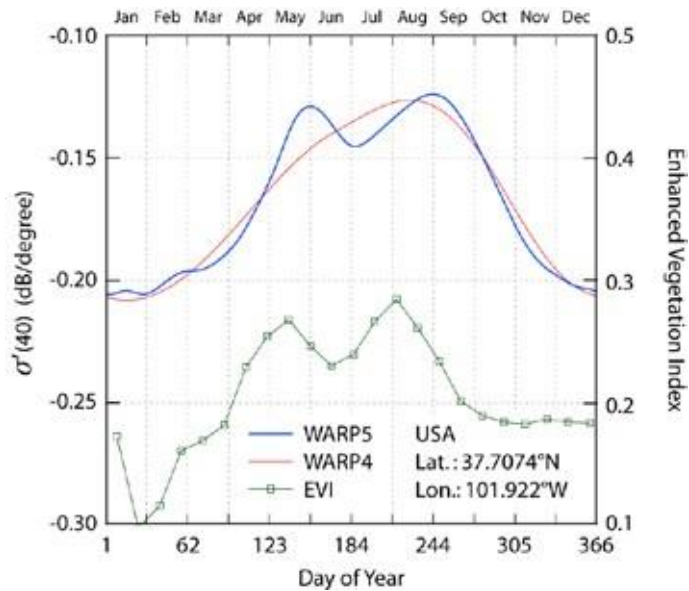


Figure 4-13: Comparison of different estimated slope functions to an averaged enhanced vegetation index (EVI) [from Naeimi et al. (2009)]

	<h2>The SCIRoCCo Scatterometry Handbook</h2>	<b>Ref:</b>	SCI-PUB-14-0001-v01
		<b>Issue:</b>	6
		<b>Date:</b>	10/10/2017
		<b>Proj:</b>	SCIRoCCo Scatterometer Instrument Competence Centre

### 4.3.3 Vegetation correction

The TU-Wien soil moisture retrieval model was developed by making use of a set of study areas covered by different vegetation types. The total backscatter coefficient recorded over these vegetated surfaces is anticipated to be a mixture of three scattering mechanisms (see Figure 4-14). The contributions to the total recorded backscatter are:

- a) surface scattering from the underlying soil surface,
- b) volume scattering from the vegetation canopy and
- c) multiple-path interactions between tree trunks and soil surface.

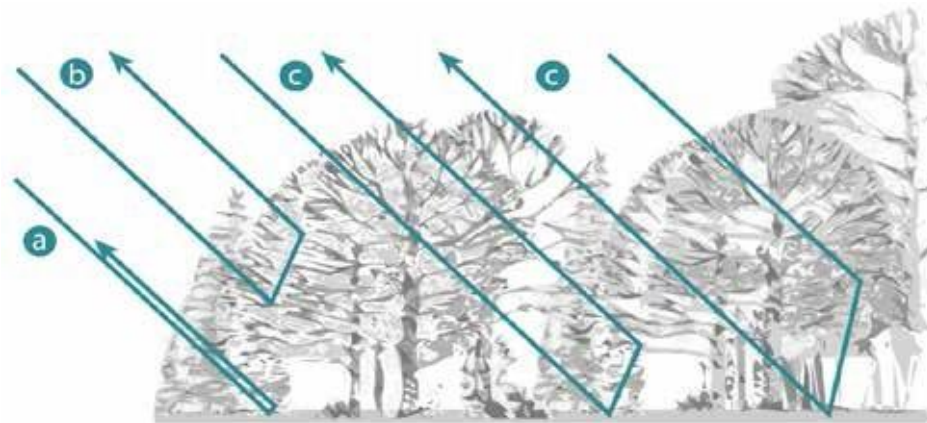


Figure 4-14: Backscatter from vegetated surfaces [from Bartalis (2009)]

Accordingly, a mathematical formulation of the total backscatter recorded over vegetated surfaces is given by:

$$\sigma_{vwSSwvaSS}^0 = \sigma_{sssdffaassvw}^0 + \sigma_{vrsSSSSmmwvw}^0 + \sigma_{SSiwwvwdaaassvwSSSi}^0 \quad \text{Eq. 4-13}$$

The volume scattering contribution  $\sigma_{\text{volume}}^0$  to the total backscatter is due to the direct backscatter of the incoming wave by vegetation elements. The surface scattering term  $\sigma_{\text{surface}}^0$  constitutes the bare soil backscatter of the underlying soil surface attenuated by the vegetation canopy. Multi-path interactions between tree trunks and the soil surface are represented by the interaction term  $\sigma_{\text{interaction}}^0$ . In general, the interaction term  $\sigma_{\text{interaction}}^0$  is assumed to be much smaller than the volume and surface scattering term providing no significant contribution to the total backscatter. The incidence angle behaviour of the volume and the surface scattering terms are noticeably different. With the exception of very rough surfaces, bare soil backscatter coefficients tend to decrease rapidly with increasing incidence angle. In contrast, volume scattering from the vegetation canopy is quite uniform across a large range of incidence angles. With respect to growing vegetation canopy, the total recorded backscatter coefficient may decrease or increase, depending on whether the attenuation of the bare soil scattering is more important than the enhanced contribution of the volume scattering term of the vegetation canopy, or vice versa. However, it is supposed that at a specific incidence angle, hereafter referred to as crossover angle, the total backscatter of dormant vegetation, dominated by the surface scattering term, and the backscatter of fully grown vegetation, dominated by the volume

	<h1>The SCIRoCCo Scatterometry Handbook</h1>	Ref:	SCI-PUB-14-0001-v01
		Issue:	6
		Date:	10/10/2017
		Proj:	SCIRoCCo Scatterometer Instrument Competence Centre

scattering term, are equal. If such a crossover angle exists, the magnitude of the total backscatter depends exclusively on the soil moisture condition. Furthermore, for dry soil moisture conditions, the crossover angle should be found at lower incidence angles than for wet conditions (see Figure 4-15). An empirical analysis performed by Wagner et al. (1999a) stated that the dry crossover angle  $\theta_{dry}$  can be found at  $25^\circ$  and the wet crossover angle  $\theta_{wet}$  at  $40^\circ$  incidence angle. With respect to the soil moisture retrieval, the crossover angle concept allows to account for vegetation effects controlling the total backscatter, if the crossover angles are chosen correctly.

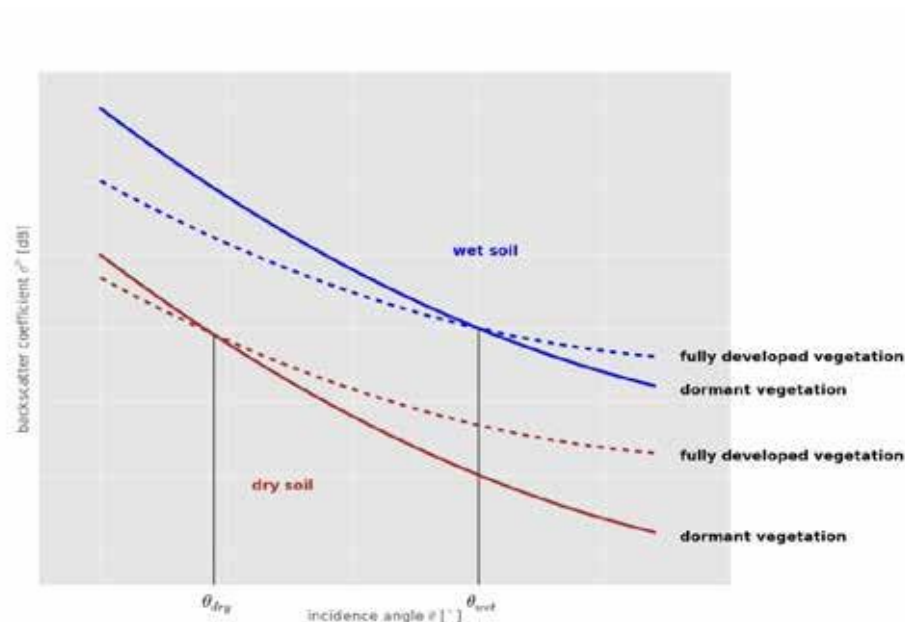


Figure 4-15: Illustration of the crossover angle concept for vegetation correction

	<b>The SCIRoCCo</b> <b>Scatterometry Handbook</b>	Ref:	SCI-PUB-14-0001-v01
		Issue:	6
		Date:	10/10/2017
		Proj:	SCIRoCCo Scatterometer Instrument Competence Centre

#### 4.3.4 Soil moisture retrieval

The TU-Wien soil moisture model is a physically motivated change detection method based on the assumption that the relationship between the observed backscatter coefficient, expressed in Decibel (dB), and the actual soil moisture condition is linear. Accordingly, soil moisture values can be retrieved by comparing azimuth and incidence angle normalised backscatter measurements with the historically driest (lowest backscatter) and wettest (highest backscatter) observed soil condition. The wettest possible condition is that of saturation, defined as the condition in which all the soil pores are filled with water, and the driest possible condition is designated to the so-called air dryness. Therefore, the retrieved soil moisture values from the TU-Wien model are commonly expressed as degree of saturation of the soil surface layer. By employing a multi-year backscatter time series of ESCAT data, it is most likely that the conditions of air dryness and saturation captured. Figure 4-16 depicts the soil moisture retrieval method in a simplified manner which is discussed in the following. The surface soil moisture retrieval can be divided into three modelling steps:

1. Backscatter normalisation
2. Vegetation correction
3. Soil moisture estimation

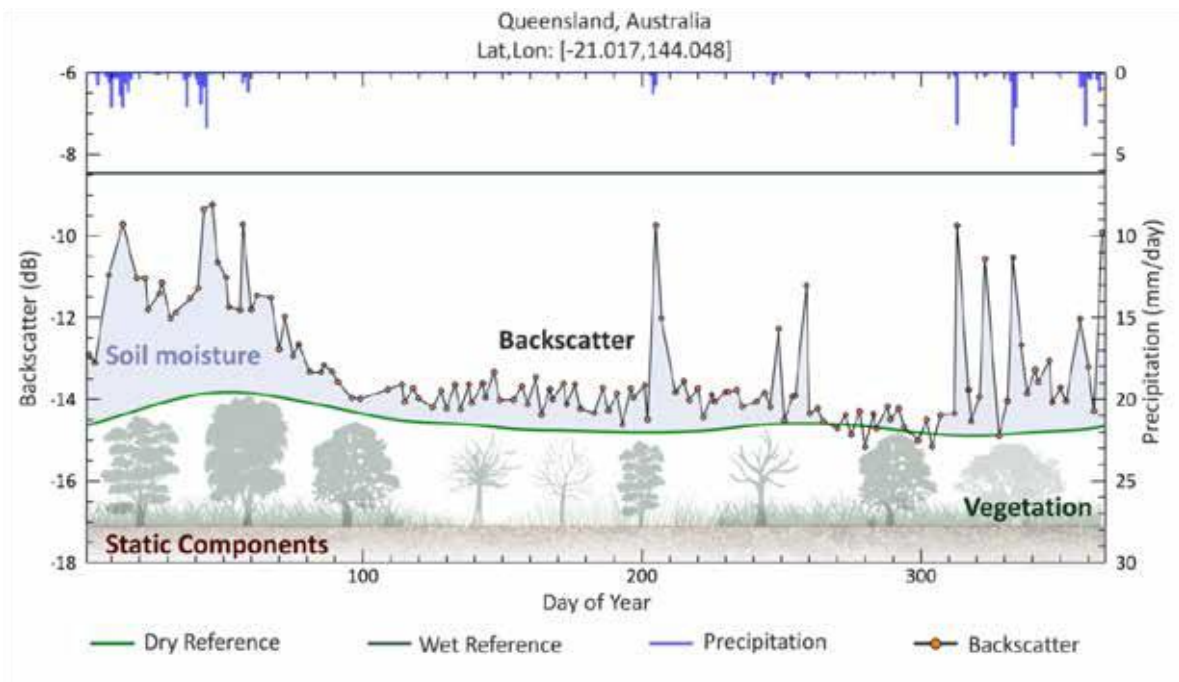


Figure 4-16: Illustration of the soil moisture retrieval approach

	<h2 style="text-align: center;">The SCIRoCCo Scatterometry Handbook</h2>	<b>Ref:</b>	SCI-PUB-14-0001-v01
		<b>Issue:</b>	6
		<b>Date:</b>	10/10/2017
		<b>Proj:</b>	SCIRoCCo Scatterometer Instrument Competence Centre

Backscatter normalisation is done with respect to the already presented considerations discussed in the previous sections of this chapter, following the enhanced approaches from Bartalis et al. (2006) and Naeimi et al. (2009). Employing these methods results in azimuth and incidence angle normalised backscatter observations that are comparable over time.

Vegetation correction is carried out by making use of the already introduced crossover angle concept for estimating the historically driest and wettest soil moisture condition. It should be recapitulated that at the dry and wet crossover angle, vegetation is assumed to have no effect on the total backscatter. As a consequence, the historically driest soil moisture condition can be estimated by means of extrapolating the normalised backscatter coefficients  $\sigma^0(40^\circ, t)$  to the respective dry crossover angle  $\theta_{dry}$  by using:

$$\sigma^0(\theta_{dry}, tt) = \sigma^0(40^\circ, tt) + \sigma'(40^\circ, tt) \cdot (\theta_{dry} - 40^\circ) + \frac{1}{2} \sigma''(40^\circ, tt) \cdot (\theta_{dry} - 40^\circ)^2 \quad \text{Eq. 4-14}$$

An estimate of the dry reference  $\sigma^0_{dry}$  is computed as the mean of the 2.5% lowest backscatter values at the dry crossover angle as indicated by:

$$\sigma^0_{dry}(\theta_{dry}, tt) = \frac{1}{M} \sum_{k=1}^M \sigma^0_k(\theta_{dry}, tt) \quad \text{Eq. 4-15}$$

where M denotes the number of the k lowest backscatter observations. Ultimately, the lowest observed backscatter, dry reference  $\sigma^0_{dry}$ , has to be shifted back to the reference incidence angle  $\theta_{ref}$  of 40 degrees by means of the corresponding slope and curvature functions as stated by Eq. 4-11. It should be noted, that with regard to the estimation of the wet reference  $\sigma^0_{wet}$ , an extrapolation to the wet crossover angle is not necessary, because the reference incidence angle  $\theta_{ref}$  and the wet crossover angle  $\theta_{wet}$  are assumed to be equal to 40 degrees. Apart from that, the wet reference  $\sigma^0_{wet}$  is obtained in a completely analogue fashion, but instead of the 2.5% lowest values, the 2.5% highest backscatter coefficients are averaged. It is worth mentioning that because of the utilised crossover angle concept and the back-shift of the determined dry reference  $\sigma^0_{dry}$  to the reference incidence angle  $\theta_{ref}$ , a vegetation correction is applied, reflected in a temporal varying dry reference. Whereas the wet reference is constant over time, because the wet crossover angle  $\theta_{wet}$  is equal to the reference incidence angle  $\theta_{ref}$  and therefore no back-shift has to be performed.

Finally, soil moisture estimates can be retrieved by comparing the observed normalised backscatter measurements  $\sigma(40^\circ, t)$  to the dry ( $\sigma^0_{dry}$ ) and wet ( $\sigma^0_{wet}$ ) reference [see Figure 4-17 a)]. Under the assumption of a linear relationship between the backscatter in Decibel (dB) and soil moisture [see Figure 4-17 b)], the latter can be estimated as (Wagner, 1998):

$$ssss(tt) = \frac{\sigma^0(40, tt) - \sigma^0_{dry}(40, tt)}{\sigma(40, tt) - \sigma^0_{wet}(40, tt)} \quad \text{Eq. 4-16}$$

Figure 4-18 depicts the individual steps required to retrieve surface soil moisture with the TU-Wien model in a simplified manner as a flow chart.



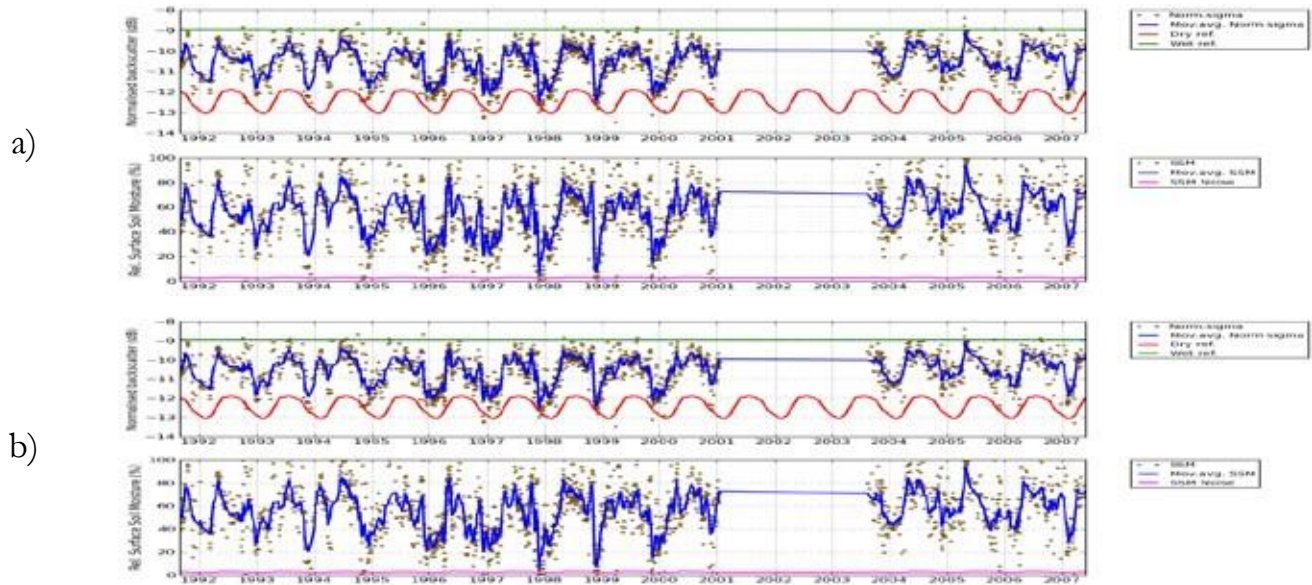


Figure 4-17: Soil moisture retrieval at a location near Moscow [Lat: 55.36, Lon: 39.82]

- a) Illustration of the dry reference, wet reference and the normalised backscatter measurements
- b) The derived soil moisture time series with its noise estimate.

The data gap between 2001 and August 2003 is because of the so called zero gyro mode (ZGM) of ERS-2.

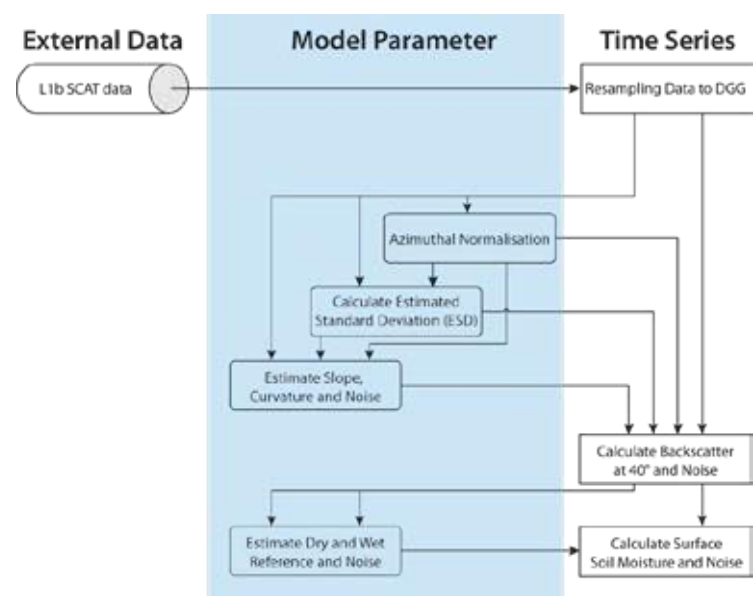


Figure 4-18: Flow chart of the individual steps of the TU-Wien surface soil moisture retrieval model

	<p>The SCIRoCCo Scatterometry Handbook</p>	Ref:	SCI-PUB-14-0001-v01
		Issue:	6
		Date:	10/10/2017
		Proj:	SCIRoCCo Scatterometer Instrument Competence Centre

### 4.3.5 Soil moisture uncertainty estimation

In the TU-Wien model, parallel to the soil moisture calculation, an estimate of the uncertainty of the soil moisture retrieval is determined by rules of error propagation. The initial step of this error propagation is to determine the noise level of the backscatter measurements. This is based on the following observation: all three beams observe the same region (soil moisture), and the fore- and aft-beam have the same incidence angle. Thus, as long as there are no azimuthal effects, the measurements of the fore- and aft-beam are comparable, i.e., statistically speaking, they are instances of the same distribution. Hence, the expectation of the difference:

$$\delta\delta = \sigma_{\text{fssd}} - \sigma_{\text{affw}} \quad \text{Eq. 4-17}$$

should be 0, and its variance should be twice the variance of one of the beams (assuming, the measurements are independent):

$$\text{vvaavv}[\delta\delta] = 2 * \text{vvaavv}[\sigma^0] \quad \text{Eq. 4-18}$$

By taking the square root and re-arranging, Eq. 4-18, this gives us an estimate of the standard deviation of the backscatter  $\sigma^0$ , which is called estimated standard deviation (ESD):

$$\text{EESDD} = \text{sstss}[\sigma^0] = \frac{\text{sstss}[\delta\delta]}{\sqrt{2}} \quad \text{Eq. 4-19}$$

whereby  $\text{std}[\delta]$  is obtained as the empirical standard deviation of  $\delta$  over the entire observation time period. According to the rules of error propagation, a noise estimate of the normalised backscatter  $\sigma^0(40^\circ, t)$  is obtained by:

$$\text{vvaavv}[\sigma^0(40^\circ, tt)] = \frac{1}{9} \sqrt{\text{EESDD}^2 + \text{vvaavv}[\sigma'(40^\circ, tt)] * (\theta_{\text{SS}} - 40^\circ)^2} + \frac{1}{4} \text{vvaavv}[\sigma''(40^\circ, tt)] * (\theta_{\text{SS}} - 40^\circ)^4 \quad \text{Eq. 4-20}$$

In Eq. 4-20 the subscript  $i$  denotes the individual fore-, mid- and aft-beam measurements of the backscatter triplet. Furthermore, Eq. 4-20 was deduced with the assumption that the correlation between the slope  $\sigma'(40^\circ, t)$  and curvature  $\sigma''(40^\circ, t)$  parameter is negligible. Moreover, the uncertainty of the normalised backscatter  $\text{var}[\sigma^0(40^\circ, t)]$  varies depending on the observation time  $t$  and the acquisition incidence angle  $\theta_i$ . Hence, there exists no simple general expression for the noise estimate of the dry and wet reference. Though, under the assumption of uncorrelated noise contributions of the normalised backscatter measurements, the following uncertainty estimate of the dry reference is found.

$$\text{vvaavv}[\sigma^0(40^\circ, tt)] = \frac{1}{MM^2} \sum_{kk=1}^{MM} \text{vvaavv}[\sigma^0(\theta_{\text{kk}}, tt)] + \text{vvaavv}[\sigma'(40^\circ, tt)] * (\theta_{\text{kk}} - 40^\circ)^2 + \frac{1}{4} \text{vvaavv}[\sigma''(40^\circ, tt)] * (\theta_{\text{kk}} - 40^\circ)^4 \quad \text{Eq. 4-21}$$

	<h1>The SCIRoCCo Scatterometry Handbook</h1>		Ref:	SCI-PUB-14-0001-v01
			Issue:	6
	Date:	10/10/2017	Proj: SCIRoCCo Scatterometer Instrument Competence Centre	

The noise estimate of the wet reference is obtained in a completely analogue fashion to Eq. 4-21, but simplifies to

$$v_{\sigma_{\theta}}[\sigma_{\theta}^0(40^\circ)] = \frac{1}{M} \sqrt{\sum_{k=1}^M v_{\sigma_{\theta}}[\sigma_{\theta}^0(\theta_{k, \text{wet}})]^2}, \quad \text{Eq. 4-22}$$

because the wet crossover angle and the reference incidence angle are equal to 40 degrees. In both equations (Eq. 4-21 and Eq. 4-22) the upper bound of summation, denoted by M, represents the number of the k lowest/highest backscatter observations. Finally, by proceeding along the lines of the derivation, the following uncertainty estimate of the soil moisture retrieval can be given.

$$v_{\sigma_{\theta}}[\sigma_{\theta}^0(40^\circ, tt)] = \frac{v_{\sigma_{\theta}}[\sigma_{\theta}^0(40^\circ, tt)]}{\sigma_{\theta}^0(40^\circ, tt) - \sigma_{\theta}^0(40^\circ)} + \frac{v_{\sigma_{\theta}}[\sigma_{\theta}^0(40^\circ, tt) - \sigma_{\theta}^0(40^\circ)]}{\sigma_{\theta}^0(40^\circ, tt) - \sigma_{\theta}^0(40^\circ)} + v_{\sigma_{\theta}}[\sigma_{\theta}^0(40^\circ)] \quad \text{Eq. 4-23}$$

	<b>The SCIRoCCo</b> <b>Scatterometry Handbook</b>	Ref:	SCI-PUB-14-0001-v01
		Issue:	6
		Date:	10/10/2017
		Proj:	SCIRoCCo Scatterometer Instrument Competence Centre

## 4.4 Applications

### 4.4.1 From surface soil moisture to root zone soil moisture

Soil moisture measurements from ESCAT represent the water content of the first few centimetres of the soil profile, because the penetration depth of C-band microwaves is limited to about 0.5 cm to 2 cm. For different applications, such as numerical weather prediction, hydrological or vegetation studies, a key input variable is the root zone soil moisture. Root zone soil moisture constitutes the water content available for vegetation and is therefore an important driver for evapotranspiration which strongly influences the energy flux between the land surface and the atmosphere. The relationship between surface soil moisture and root zone soil moisture is given through the process of infiltration. A large number of parameters like soil characteristics (soil texture and structure), vegetation coverage, soil temperature and the present water content control the infiltration rate of water into the deeper soil layers. Because of the lack of information about this parameters on a global scale, Wagner et al. (1999) developed an empirical method for estimating root zone soil moisture from remotely sensed surface soil moisture measurements. The empirical method is based on a two-layer water balance model, in which the first layer represents the C-band microwave accessible top-soil layer and the second layer is treated as a reservoir coupled with the atmosphere via the first layer exclusively. In view of the fact that the first layer is directly connected to the atmosphere, the water content in the surface soil layer is temporally highly dynamic, due to processes such as precipitation, evapotranspiration and runoff. On the other hand, the temporal variability of the water content within the reservoir, the second layer, is supposed to decrease with increasing reservoir depth as a result of a slow exchange with the surface layer. As a consequence, the water content stored within the reservoir is controlled by the soil moisture conditions in the surface layer and thus a function of preceding precipitation events. Accordingly, the following water balance equation for the reservoir is proposed under the assumption that the water flux between the two soil layers is proportional to the difference of the volumetric water content in the surface layer and the reservoir (Ceballos et al., 2005; Wagner et al., 1999).

$$\frac{d\theta_{ss}(t)}{dt}$$

$$L \frac{d\theta_{ss}(t)}{dt} = CC * [\theta_{ss}(t) - \theta(t)] \quad \text{Eq. 4-24}$$

In this water balance equation for the reservoir, Eq. 3-24, the volumetric water content of the reservoir is denoted by  $\theta$ , the water content of the surface layer is  $\theta_{ss}$ ,  $t$  is the time,  $L$  is the depth of the reservoir layer and  $C$  is a pseudodiffusivity coefficient incorporating all soil properties. If  $C$  is assumed to be constant and  $T=L/C$ , the differential water balance equation can be solved as follows:

$$\theta(t) = \frac{1}{T} \int_{-\infty}^t \theta_{ss}(\tau) * e^{-\frac{t-\tau}{T}} d\tau \quad \text{Eq. 4-25}$$

The parameter  $T$  is referred to as characteristic time length, which increases with the reservoir depth  $L$  and decreases with the pseudo diffusivity coefficient  $C$ . As explained by the water balance model equation (Eq. 4-25), the water content of the reservoir  $\theta$  is fully explained by past dynamics of the surface soil moisture content  $\theta_{ss}$ . Furthermore,

more recent events have a stronger impact on the reservoir water content than events from the distant past as a result of the exponential weighting function. The water balance model is a useful general concept for estimating root zone soil moisture from surface soil moisture measurements, but it does not consider processes like transpiration or evaporation. However, ESCAT provides measurements at irregular temporal intervals. Consequently, the continuous formulation of the model (Eq. 4-25) was replaced by its discrete counterpart defined as the soil water index (SWI). Taking into account the before mentioned considerations, the SWI for a defined characteristic time length T can be calculated as follows:

$$SSWSS(t) = \frac{\sum_{ee}^{ss} ssss(tt) * \frac{e^{-\frac{t-t_i}{T}}}{T}}{\sum_{ee}^{ss} e^{-\frac{t-t_i}{T}}} \quad ffffvvt_{ss} \leq t \quad \text{Eq. 4-26}$$

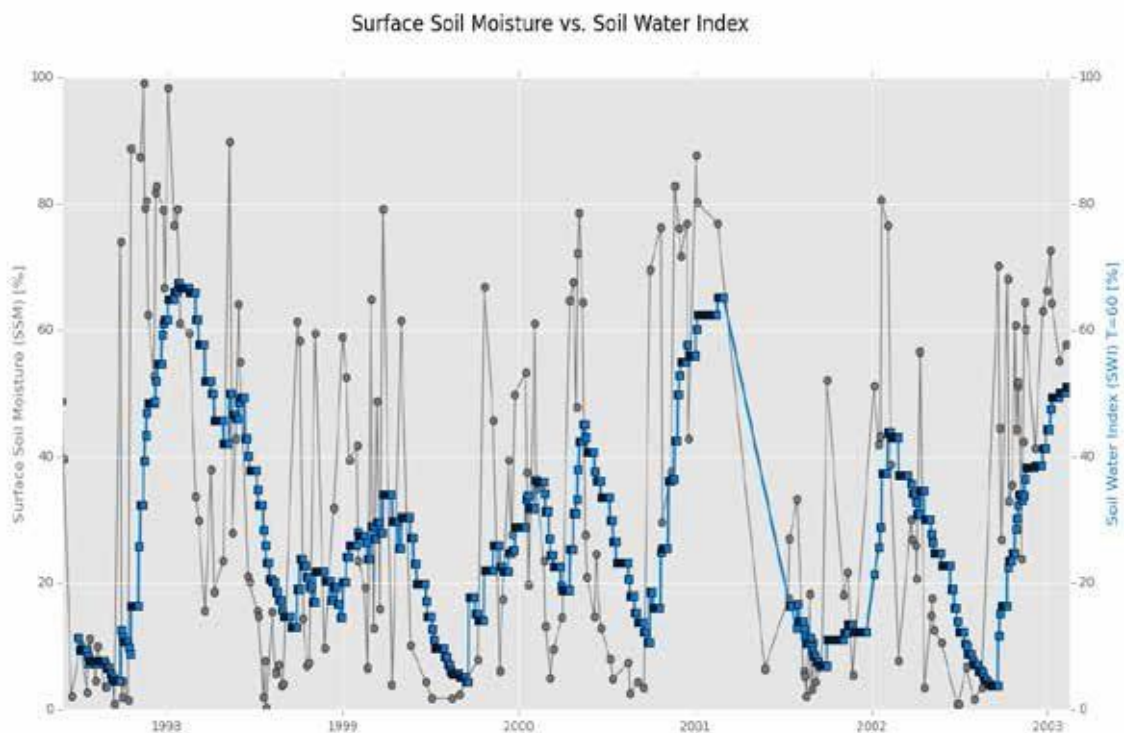


Figure 4-19: Time series of surface soil moisture and the computed soil water index (SWI) at a location in Portugal [Lat: 39.17, Lon: -7.81]

	<h2 style="text-align: center;">The SCIRoCCo Scatterometry Handbook</h2>	<b>Ref:</b>	SCI-PUB-14-0001-v01
		<b>Issue:</b>	6
		<b>Date:</b>	10/10/2017
		<b>Proj:</b>	SCIRoCCo Scatterometer Instrument Competence Centre

#### 4.4.2 Creation of a Climate Data Record (ESA CCI soil moisture)

Surface soil moisture was recognised as an Essential Climate Variable (ECV) in 2010 and accordingly became an important dataset for IPCC (Intergovernmental Panel on Climate Change) and UNFCCC (United Nations Framework Convention on Climate Change) needs. ECV data records should be as long, complete and consistent as possible, and in the case of soil moisture this means that the data record shall be based on multiple data sources, including but not limited to active (scatterometer) and passive (radiometer) microwave observations acquired preferably in the low-frequency microwave range. The list of space-based microwave sensors that can be used for this task are the European C-band scatterometers on-board of the ERS and MetOp satellites and the multi-frequency radiometers SMMR, SSM/I, TMI, AMSR-E, Windsat and AMSR2 covering a time period of more than 30 years. Therefore, in recognition of the strong need for global soil moisture data sets, the European Space Agency (ESA) set up the Climate Change Initiative “Soil Moisture” (ESA CCI SM) with the objective to produce the most complete and most consistent global soil moisture data record based on active and passive microwave sensors. The production scheme of the ESA CCI SM data record is based on Level 2 soil moisture retrievals and involves the following steps:

1. Level 2 soil moisture retrieval is done for each satellite data set separately
2. Fusion of the active Level 2 data sets
3. Fusion of the passive Level 2 data sets
4. Merging of the active and passive data sets from steps 2 and 3

In this approach the three important steps in the fusion process are: 1) error characterisation, 2) matching to account for data set specific biases, and 3) merging. The major advantage of this approach is that it allows combining surface soil moisture data derived from different microwave remote sensing instruments with substantially different instrument characteristics. It is only required that the retrieved Level 2 surface soil moisture data pass pre-defined quality criteria. In this way it is guaranteed that no sensor is a priori excluded by this approach. It is thus straight forward to further enrich the ECV data set with Level 2 data from other existing (SMOS, SMAP, radar altimeters, ...) and forthcoming sensors. First results of the project were reported by (Dorigo et al., 2010) who used the novel triple collocation method (Miralles et al., 2010; Scipal et al., 2008) for characterising the spatially variable error field of active (ASCAT) and passive (AMSR-E and SSM/I) soil moisture retrievals. The fusion algorithm itself was first presented by Liu et al. (2011), who merged AMSR-E and ASCAT soil moisture retrievals for the year 2007 and furthermore by Liu et al. (2012) merging a set of active and passive microwave sensors. They found that the merging process improved the spatial and temporal coverage while minimally impacting the accuracy of the soil moisture retrievals.

As can be envisioned, ERS-1/2 ESCAT plays a vital role in the generation of a long-term consistent climate variable with soil moisture retrievals covering a time period of 20 years of active microwave observations. Nevertheless, ERS-1/2 ESCAT underwent a number of mission events which had to be tackled by the ground segment, implicating potential inconsistency in the currently available data archive. Thanks to the SCIRoCCo, these inconsistencies will be

	<h1>The SCIRoCCo Scatterometry Handbook</h1>	Ref:	SCI-PUB-14-0001-v01
		Issue:	6
		Date:	10/10/2017
		Proj:	SCIRoCCo Scatterometer Instrument Competence Centre

resolved by the use of state of the art scatterometer processing facilities and improved soil moisture retrieval models, highlighting the significance of the project in the context of climate change research (see Figure 4-20).

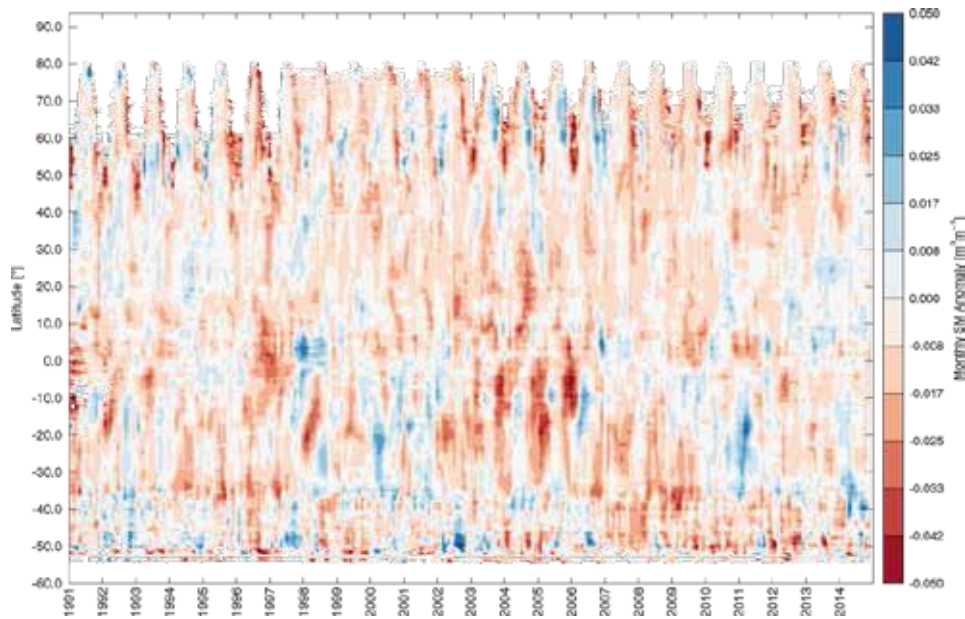


Figure 4-20: Hovmoeller plot showing soil moisture anomalies from 1991 to 2014, computed from the merged active and passive microwave soil moisture retrievals.

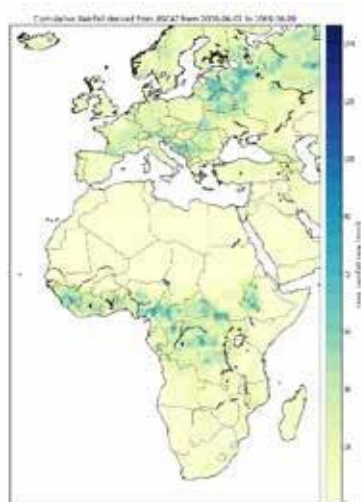


Figure 4-21: Rainfall estimation from ASCAT surface soil moisture retrieval based on SM2RAIN

	<p>The SCIRoCCo Scatterometry Handbook</p>	Ref:	SCI-PUB-14-0001-v01
		Issue:	6
		Date:	10/10/2017
		Proj:	SCIRoCCo Scatterometer Instrument Competence Centre

#### 4.4.3 Rainfall estimation through surface soil moisture observations

Obviously soil moisture content and rainfall share a strong physical connection because rainfall is the main driver of temporal soil moisture variations. For instance, after a rainfall event, soil moisture exhibits a sudden increase followed by a smooth decline caused by evapotranspiration and drainage. Based on the strong rainfall – surface soil moisture feedback, Pellarin et al. (2008) developed a methodology to improve rainfall estimates by using surface soil moisture observations. Independently, Crow et al. (2009) describe and apply a data assimilation approach, build on Kalman filtering, to correct land rainfall accumulation estimates using remotely sensed surface soil moisture retrievals. Both approaches require a first guess rainfall estimate as the proposed algorithms are only capable to correct / improve rainfall information by utilising soil moisture data. More recently, Brocca et al. (2013) presented an approach for estimating, not for correcting, rainfall by employing surface soil moisture observations (see Figure 4-21). The method leans upon the inversion of the hydrological water balance regarding soil as a natural reservoir. With the assumption of negligible evaporation rate and that all precipitation infiltrates into the soil, the following relation can be given.

$$pp(tt) \cong ZZ \frac{ssss(tt)}{sstt} + aa \frac{ss(tt)}{bb} \quad \text{Eq. 4-27}$$

In Eq. 4-27,  $p(t)$  denotes the precipitation,  $Z$  is the depth of the soil layer,  $s(t)$  expresses the relative saturation of the soil,  $t$  is the time and  $a$  and  $b$  are two parameters characterising the nonlinear relationship between the drainage rate and soil saturation. A crucial step in this rainfall estimation approach is the calibration of the model parameters  $Z$ ,  $a$  and  $b$  with respect to a benchmark dataset like the GPCP product as demonstrated in Brocca et al. (2014). The first analysis of this rainfall estimation approach, referred to as SM2RAIN, shows promising results, especially by utilising scatterometer derived surface soil moisture products from the Advanced Scatterometer (ASCAT) on-board the Meteorological Operational (MetOp) satellites.



	<p>The SCIRoCCo Scatterometry Handbook</p>	Ref:	SCI-PUB-14-0001-v01
		Issue:	6
		Date:	10/10/2017
		Proj:	SCIRoCCo Scatterometer Instrument Competence Centre

## 5 Ocean winds

This Handbook's chapter outlines user information for the wind products based on the ERS scatterometer. It includes a brief description of the ERS SCAT instrument, the processing algorithms and the data processing, and the wind product quality.

The scatterometer is an instrument that provides information on the wind field near the ocean surface, and the knowledge of extracting this information from the instrument's output is dealt with in this chapter. Space-based scatterometry has become of great benefit to meteorology and climate in the past years, see e.g. (Isaksen & Stoffelen, 2000).

### 5.1 Algorithms and Processing

In Europe scatterometer processing software is developed in the EUMETSAT Numerical Weather Prediction Satellite Application Facility (NWP SAF), whereas wind processing is performed (semi-)operationally in the Ocean and Sea Ice SAF (OSI SAF). KNMI has a long experience in scatterometer processing and is developing generic software for this purpose. Processing systems have been developed for the ERS scatterometer (ESCAT), ASCAT on MetOp, NSCAT on the Japanese ADEOS-I platform, SeaWinds on ADEOS-II and QuikSCat, the Indian OceanSat-2 scatterometer (OSCAT), the Chinese HY2A scatterometer, and will be further developed for future scatterometers such as RapidScat on the International Space Station (ISS).

KNMI was and is involved in the EARS ERS and ASCAT service as the centre where the Level 1b to Level 2 processing is carried out. As a preparation for the EARS ASCAT service, KNMI has established and operated a demonstration system based on the dissemination via EUMETCast of the current regional ERS-SCAT KNMI value-added wind product. A Product User Manual to this product is available on [www.knmi.nl/scatterometer/ers\\_prod/](http://www.knmi.nl/scatterometer/ers_prod/). The wind products are distributed in the BUFR and NetCDF CF compliant formats that are also used for the ASCAT wind data and other scatterometers. Therefore, the ERS data stream can be ingested by the user using the same interfacing as for the European ASCAT and other scatterometer wind products. Besides wind data, the KNMI processing services offer additional quality control and monitoring (Quality Assurance) ensuring that only reliable data will be made available. See also [www.knmi.nl/scatterometer/](http://www.knmi.nl/scatterometer/) for real-time graphical examples of the products and up-to-date information and documentation on all scatterometer products processed at KNMI.

	<p>The SCIRoCCo Scatterometry Handbook</p>	Ref:	SCI-PUB-14-0001-v01
		Issue:	6
		Date:	10/10/2017
		Proj:	SCIRoCCo Scatterometer Instrument Competence Centre

## 5.2 Stress-equivalent 10m wind

A scatterometer measurement relates to the ocean surface roughness (see figure 5.2.1), while the scatterometer product is represented by the wind at 10m height over a WVC. It is important to realize that in the approach followed here, the radar backscatter measurement  $\sigma^0$  is related to the wind at 10 meter height above the ocean surface, simply because such measurements are widely available for validation.

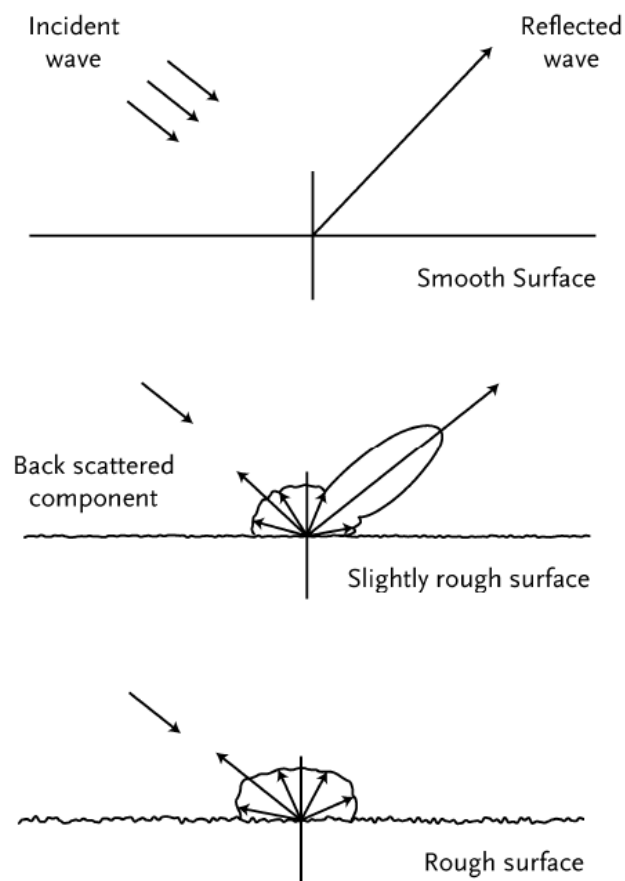


**Figure 5.2.1.** Schematic representation of microwave scattering and reflection at a smooth (a), rough (b) and very rough (c) ocean surface. As the roughness increases more microwave power is returned towards the direction of the microwave source.

This does not mean that any effect that relates to the mean wind vector at 10 meter height is incorporated in the backscatter-to-wind relationship. In particular, air stability and mass density are not sensed by the wind scatterometer

	<h2>The SCIRoCCo Scatterometry Handbook</h2>	<b>Ref:</b>	SCI-PUB-14-0001-v01
		<b>Issue:</b>	6
		<b>Date:</b>	10/10/2017
		<b>Proj:</b>	SCIRoCCo Scatterometer Instrument Competence Centre

and should not appear in the derived 10m wind. Moreover, in buoy and NWP model validation sources, the 10m wind may be corrected for air stability and mass density with good precision. Therefore, scatterometer winds are given as so-called stress-equivalent 10m winds, abbreviated as U10S.

To avoid atmospheric stability effects, we define the 10-m equivalent neutral wind vector,  $\mathbf{U}_{10N}$ , rather than the actual 10-m wind vector  $\mathbf{U}_{10}$ . To obtain  $\mathbf{U}_{10}$  from  $\mathbf{U}_{10N}$  one needs information on the stability of the atmospheric boundary layer, which may be obtained from buoys or NWP models with sufficient precision (Portabella and Stoffelen, 2006). Using Monin-Obukhov similarity scaling, the equivalent neutral wind vector amplitude is simply given by

$$U_{10N} = u_* \ln \frac{z_0}{K_A z_0} \quad (5.3.1)$$

where  $z_0$  is the aerodynamic roughness length, the friction velocity is defined by the equation for the kinematic wind stress  $u_*^2 = \tau / \rho$  and  $K$  is von Karman's constant. The aerodynamic roughness length

$$z_0 = \frac{0.11 \varpi}{\alpha u_*} + \frac{2}{g} \quad (5.3.2)$$

is approximated from the known geophysical variables  $\varpi$ , kinematic viscosity of the air ( $1.5 \times 10^{-5} \text{ m}^2/\text{s}$ ),  $\alpha$ , (dimensionless) Charnock parameter (see Charnock, 1955) and  $g$  is the gravitational constant of the Earth ( $9.81 \text{ m/s}^2$ ). The Charnock value, which is a sea-state parameter, varies substantially for different surface layer schemes, i.e., from 0.011 for to around 0.018.

For the same  $\mathbf{U}_{10N}$ , cold heavy air will produce more stress (and roughness) than lighter warmer air. This effect is expressed by the surface stress equation. The surface wind stress  $\tau = \rho u_*^2$  indeed depends on the air density  $\rho$ . Assuming that  $\sigma^0$  measurements are more a measure of  $\tau$  than  $U_{10N}$ , the  $\rho$  correction for  $U_{10N}$  takes the form

$$U_{10N} = \sqrt{\frac{\langle \tau \rangle}{\rho}} \quad (5.3.3)$$

where  $U_{10S}$  denotes the current set of stress-equivalent scatterometer wind retrievals and  $\langle \rho \rangle$  is the average air density as defined in a standard atmosphere ( $\approx 1.225 \text{ kg/m}^3$ ).  $\rho$  variations, which depend on surface pressure, air temperature, and humidity, are generally small (1-2%) and can exceptionally increase locally in cases such as cold air outflow.

We note the following:

1. When computing stress from  $U_{10S}$ , one should multiply by some globally average air density as opposed to using an air density value at the location of the measurement that one might get from a numerical model. The reason for this is that  $\mathbf{U}_{10S}$  already includes the effect of varying air density;

	<p>The SCIRoCCo Scatterometry Handbook</p>	Ref:	SCI-PUB-14-0001-v01
		Issue:	6
		Date:	10/10/2017
		Proj:	SCIRoCCo Scatterometer Instrument Competence Centre

- To obtain the value of  $U_{10N}$ , one should multiply  $U_{10S}$  by the air density ratio shown in equation (5.3.3).

However, wind scatterometers may be sensitive to more parameters than only those that relate (correlate) with  $U_{10S}$ . For example, the appearance of surface slicks, suppressing the amplitude of gravity or longer ocean waves and thus microwave roughness, is associated with low winds and depends to some degree on the strength of the wind and may, to the same degree, be fitted by a geophysical model function, GMF (Stoffelen, 1998; Chapter I). However, abundant surfactants, generated by natural or human causes, may render the nominal wind-to-backscatter relationship, as captured by the GMF, less accurate. Other variable effects, such as rain (mainly for Ku-band scatterometers), extreme wind variability, complex sea states, etc., may affect GMF accuracy too. Stoffelen (Stoffelen, 1998; Chapter IV) discusses a unique method to determine the accuracy of scatterometer, buoy, and NWP model  $U_{10S}$  winds: triple collocation, which will be discussed later. First we discuss the geophysical relationship between  $U_{10S}$  and backscatter.

### 5.3 Geophysical model function

For the ERS wind product, the CMOD6 geophysical model function (GMF) for calculating stress equivalent winds is used. This model function enables the calculation of wind speeds meeting the product requirements between 0 and 25 m/s. CMOD6 is based on CMOD5.n (Verhoef et al., 2008) and CMOD5 (Hersbach, Stoffelen and de Haan, 2007). It is known from extensive validation work on ERS that a CMOD5 bias of 0.5 m/s against buoys persists for all wind speeds (Portabella and Stoffelen, 2007) and this is compensated. Moreover, another 0.2 m/s is added to convert from real winds to neutral winds. The CMOD5.n inverted winds are thus 0.7 m/s higher than CMOD5 winds. Moreover, CMOD6 has been adapted to provide uniform  $U_{10S}$  wind PDFs over the ASCAT swath, taking into account the incidence-angle dependent ASCAT transponder calibration.

At low wind speeds, the wind direction and speed may vary considerably within the WVC. Locally, below a speed of roughly  $2 \text{ ms}^{-1}$  calm areas are present where little or no backscatter occurs, perhaps further extended in the presence of natural slicks that increase the water surface tension (Donelan & Pierson, 1987). However, given the variability of the wind within a footprint area of 25 km it is, even in the case of zero mean vector wind, very unlikely that there are no patches with roughness in the footprint. As the mean vector wind increases, the probability of a calm patch will quickly decrease, and the mean microwave backscatter will increase. Also, natural slicks quickly disappear as the wind speed increases, and as such the occurrence of these is correlated to the amplitude of the mean vector wind over the footprint, as modelled by the GMF. Low scatterometer wind speeds are thus providing useful information.

At high wind speeds wave breaking will further intensify, causing air bubbles, foam and spray at the ocean surface, and a more and more complicated ocean topography. Although theoretically not obvious, it is empirically found that

	<p>The SCIRoCCo Scatterometry Handbook</p>	Ref:	SCI-PUB-14-0001-v01
		Issue:	6
		Date:	10/10/2017
		Proj:	SCIRoCCo Scatterometer Instrument Competence Centre

$\sigma^0$  keeps increasing for increasing wind speed from 25 m/s to 40 m/s, and that a useful wind direction dependency remains (Donnelly, Carswell and McIntosh, 1999), albeit gradually weakening.

## 5.4 Wind retrieval

KNMI has an operational processing chain running in near real-time with ASCAT data, including visualisation on the web. This processor is based on the NWP SAF software and runs in the KNMI operational environment. The processing includes monitoring and archiving functionalities. A global overview of the modules of the ERS scatterometer processor is given below.

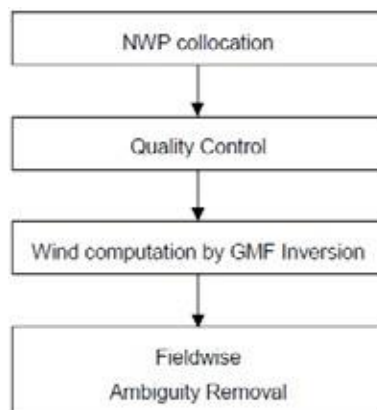


**Figure 5.4.1:** Overview of scatterometer wind retrieval algorithm.

A schematic illustration of the processing is given in figure 5.5.1. The input measurements and Geophysical Model Function not only define the wind output, but also the scatterometer processing algorithms as described below.

The GMF has two unknowns, namely wind speed and wind direction, so, if more than two backscatter measurements are available then these two unknowns may be estimated using a maximum-likelihood estimator (MLE) as the objective function for determining wind vector solutions following a Bayesian approach (Pierson, 1989). The MLE is defined by (Stoffelen, 1998; Chapter II)

$$J = (z_{oi} - z_m(u, \chi_i))^2 \quad (5.5.1)$$

where  $\mathbf{z} = (\sigma^0)^{0.625}$  are the transformed backscatter data,  $z_{oi}$  are the backscatter measurements,  $z_m(u, \chi_i)$  are the model backscatter values corresponding to the measurements. The well-defined local minima of  $J$  correspond to wind

	<h2>The SCIRoCCo Scatterometry Handbook</h2>	<b>Ref:</b>	SCI-PUB-14-0001-v01
		<b>Issue:</b>	6
		<b>Date:</b>	10/10/2017
		<b>Proj:</b>	SCIRoCCo Scatterometer Instrument Competence Centre

vector solutions. The three independent measurements (fore, mid and aft beam) well sample the azimuth variation of the GMF in order to resolve the wind direction, albeit ambiguously.

## 5.5 Ambiguity removal

ERS scatterometer winds have a multiple ambiguity with up to two wind solutions in each WVC on the earth's surface. These ambiguities are removed by applying constraints on the spatial characteristics of the output wind field, such as on rotation and divergence. Several ambiguity removal (AR) schemes were evaluated for ERS data (Stoffelen et al., 2000). In the OSI SAF Development Phase some schemes that were developed for ESCAT were compared. In addition to the subjective comparison of AR schemes, a method for the objective comparison of AR performance among the different schemes was used. In (Stoffelen et al., 2000) it is shown that this way of comparison is effective to evaluate the shortcomings of AR schemes, but also reveals a more general way forward to improve AR, which is followed up by tuning 2DVAR. For ERS this evolved version of 2DVAR is used.

## 5.6 Quality control

Since the scatterometer wind retrieval problem is over determined, this opens up the possibility of quality control (QC) by checking the inversion residual  $J$ . If  $J$  is normalised by the expected isotropic error variance then it is in theory inversely proportional to the log probability that a node is affected solely by a uniform wind. If  $Var(\sigma_m)_i = (K_{pi} \sigma_{oi})$  are the measurement variances then the norm for the inversion residual is  $\sqrt{3}$  times the root of the mean of  $(Var(\sigma_m)_i)^{0.625}$  (Stoffelen, 1998). When there is substantial wind or sea state variability within the cell, this normalised MLE is generally substantial and, as a consequence, the inferred probability low. As such, (Stoffelen, 1998) and (Portabella and Stoffelen, 2002) found that the inversion residual is well capable of removing cases with extreme variability (at fronts or centres of lows), or with other geophysical variables affecting the radar backscatter. Recently, further progress has been made in the quality assessment of ASCAT winds near rain (Lin et al., 2012; 2014).

## 5.7 NWP collocation

ECMWF wind forecasts are available twice a day (00 and 12 GMT analysis time) with forecast time steps of +3h, +6h, ..., +36h, such that KNMI receives NWP model data twice a day through the RMDCN. For reprocessing, the ECMWF archive is used, which contains reanalysis data, such as ERA-interim. At KNMI,  $U_{10s}$  is extracted from the full resolution ECMWF fields and interpolated to the time and location of the scatterometer WVCs and stored in the scatterometer output products as value-added variables. NWP model sea surface temperature and land-sea mask data are used to provide information about possible ice or land presence in the WVCs. WVCs with a sea surface temperature below 272.16 K (-1 °C) are assumed to be covered with ice and no wind information is calculated. Land presence within each WVC is determined by using the land-sea mask available from ECMWF. The weighted mean value of the land fractions of all model grid points within 80 km of the WVC centre is calculated. The weight of each

	<h2>The SCIRoCCo Scatterometry Handbook</h2>	<b>Ref:</b>	SCI-PUB-14-0001-v01
		<b>Issue:</b>	6
		<b>Date:</b>	10/10/2017
		<b>Proj:</b>	SCIRoCCo Scatterometer Instrument Competence Centre

grid point scales with  $1/r^2$ , where  $r$  is the distance between the WVC centre and the model grid point. If this mean land fraction value exceeds a threshold of 0.02, no wind retrieval is performed. Our processing uses stricter limits for ice and land presence than the ESA input product, resulting in less WVCs containing wind data (but of a better quality). NWP forecast wind data are necessary in the ambiguity removal step of the processing.

## 5.8 Calibration and Data quality

### 5.8.1 Calibration

While scatterometer systems have generally excellent calibration stability, their calibration level is difficult to determine. For fan-beam scatterometers, the beam patterns of the three beams determine the relative calibration of the backscatter values in a measured triplet for a particular WVC. This relative calibration is of utmost importance and determines the general wind retrieval quality. The different WVCs and beams experience a very similar wind climatology over a year, which is being exploited in a NWP ocean calibration (NOC) procedure, which determines a calibration value for each WVC and beam that provides statistical consistency between the calibrated backscatter triplets, the GMF and the ECMWF winds. NOC is essentially used for all scatterometers to optimise wind performance by balancing the beams for each WVC in a consistent manner. Moreover, NOC will be useful to intercalibrate scatterometers, linking ECMWF ERA-interim winds to both the ERS and ASCAT scatterometers through the GMF. In turn, both ERA-interim and scatterometer winds are being monitored and verified against buoy measurements.

### 5.8.2 Validation

Each step in the processing is validated separately by a quality control and monitoring scheme. The product validation step is controlled by visual inspection, and a statistical analysis is performed to control the validation steps. The inversion step is controlled in the same way. For ambiguity removal schemes an objective scheme exists that relies on initialisation with a one-day lead NWP forecast and validation of the ambiguity selection against NWP analyses, as in (Stoffelen et al., 2000). Moreover, (de Vries et al. 2005) describe a subjective comparison of the 2D-VAR and PreScat schemes by routine operational meteorologists.

## 5.9 Quality control and monitoring

In each WVC, the  $\sigma^0$  data is checked for quality and completeness and the inversion residual (see above) is checked. Degraded WVCs are flagged and the flag bits stored in a flag variable (see AWDP User Manual). The quality of the delivered products is controlled through an ad hoc visual examination of the graphical products and the automatic production of control parameters. The examination of the products is done at KNMI by experts. Specific tools have

	<p>The SCIRoCCo Scatterometry Handbook</p>	Ref:	SCI-PUB-14-0001-v01
		Issue:	6
		Date:	10/10/2017
		Proj:	SCIRoCCo Scatterometer Instrument Competence Centre

been developed to help this analysis. User queries obviously lead to the inspection of suspect products. The ad hoc and user queried inspections are used for quality assurance. An information file is made for each product. The content of the file is identical whatever the product and results from a compilation of all the global information concerning this product. From these files, various graphs are produced to visually display the confidence levels of the products and their evolution with time. These graphs are available on the KNMI website.

## 5.10 NWP Ocean Calibration (NOC)

The instrumental calibration of a scatterometer, and of radar in general, is a challenging problem. The mean normalized cross-section measured by an instrument,  $\sigma_{\text{obs}}^0$ , can be linearly related to its geophysical true value  $\sigma^0$  as:

$$\sigma_{\text{obs}}^0 = (1 + \delta\delta) \cdot \sigma^0$$

Where  $\delta$  is an essentially unknown calibration offset. In order to ensure stability, consistency and regularity of scatterometer winds, some calibration methods have been developed which rely on natural targets, such as the rain forest in Brazil, as calibration reference. Other methods make use of Numerical Weather Prediction (NWP) winds as calibration reference. Over the oceans, NWP winds are regularly referenced to in situ observations, such as buoys, currently providing the standard for scatterometer calibration and monitoring.

NWP Ocean Calibration (NOC) is a method for estimating the mean return from the global oceans measured by a scatterometer antenna as a function of incidence angle. The method relies on the surface wind statistics provided by a NWP model to account for the variations in ocean backscatter due to changes in wind speed and direction. NOC may be used as a simple method to perform relative calibration of scatterometer beam patterns, inter-beam calibration, or determination of cross-instrumental biases, with an estimated precision of 0.1-0.2 dB using as little as one month of data (Stoffelen, 1999) (Freilich, 1999). The method consists in comparing the global mean backscatter estimated from scatterometer measurements against simulations from a reference NWP model using a geophysical model function (GMF). The comparison gives beam and incidence angle-dependent bias corrections relative to the reference (NWP and GMF) frame, which may be attributed to a combination of instrument calibration, GMF and NWP wind errors (Verspeek et al., 2012).

### 5.10.1 Description

The NOC method is based on the analysis of a large scatterometer dataset to estimate the mean azimuthally-isotropic component of the ocean backscatter (Verspeek, 2011). For a given wind vector cell (WVC), the incidence angle is nearly constant around the orbit and removed from the equations below. The ocean backscatter is modeled as a function of wind speed  $v$  and wind direction  $\phi$  relative to the beam angle as (Stoffelen, 1998):

$$\sigma^0(v, \phi) = B_0(v) \left[ 1 + B_1(v) \cos \phi + B_2(v) \cos 2\phi \right]^{1.6} \quad (5.11.1)$$



	<h2>The SCIRoCCo Scatterometry Handbook</h2>	<b>Ref:</b>	SCI-PUB-14-0001-v01
		<b>Issue:</b>	6
		<b>Date:</b>	10/10/2017
		<b>Proj:</b>	SCIRoCCo Scatterometer Instrument Competence Centre

The term  $B_0$  is referred to as the azimuthally-isotropic backscatter component, which is a function of wind speed and incidence angle. The terms  $B_1$  and  $B_2$  represent the amplitudes of the upwind/downwind and upwind/crosswind modulations respectively, also as a function of wind speed and incidence angle. The averaging operations required to arrive at a global mean backscatter quantity are performed in a transformed space (the so called z space) whose main property is that it preserves the linearity of backscatter for changes in wind azimuth. The transformation to z space goes as:

$$z(\nu, \phi) = [\sigma^0(\nu, \phi)]^{0.625} \quad (5.11.2)$$

In z space, the ocean backscatter can be rewritten as:

$$z(\nu, \phi) = \frac{1}{2} a_0(\nu) + a_1(\nu) \cos \phi + a_2(\nu) \cos 2\phi \quad (5.11.3)$$

Where:

$$\begin{aligned} a_0(\nu) &= 2 \cdot B_0(\nu)^{0.625} \\ a_1(\nu) &= B_1(\nu) \cdot B_0(\nu)^{0.625} \\ a_2(\nu) &= B_2(\nu) \cdot B_0(\nu)^{0.625} \end{aligned} \quad (5.11.4)$$

In z space, the global mean ocean backscatter can be calculated as:

$$\langle zz(\nu\nu, \phi\phi) \rangle = \iint NN(\nu\nu, \phi\phi) \cdot zz(\nu\nu, \phi\phi) s\nu\nu s\phi\phi = \int NN(\nu\nu) \left( \int NN(\phi\phi|\nu\nu) \cdot zz(\nu\nu, \phi\phi) s\phi\phi \right) s\nu\nu \quad (5.11.5)$$

Where  $N(\nu, \phi)$  is the joint probability density function (PDF) of ocean wind speeds and wind azimuths relative to the antenna, also written as:

$$NN(\nu\nu, \phi\phi) = NN(\nu\nu) \cdot NN(\phi\phi|\nu\nu) \quad (5.11.6)$$

If the conditional distribution of wind azimuths relative to the beam angle  $N(\phi|\nu)$  for a given wind speed were uniform [i.e.  $N(\phi|\nu) = 1/(2\pi)$ ] then the azimuthally averaged backscatter in z space would be the azimuthally isotropic backscatter term:

$$\langle zz(\nu\nu, \phi\phi) \rangle_{\phi\phi} = \int NN(\phi\phi|\nu\nu) \cdot (aa_0(\nu\nu) + aa_1(\nu\nu) c\phi\phi s\phi\phi + aa_2(\nu\nu) c\phi\phi s2\phi\phi) s\phi\phi = \int aa_0(\nu\nu) \quad (5.11.7)$$

Simply put, if the global directional wind distribution was uniform, the global mean backscatter would be the isotropic response. However, the conditional distribution of global wind azimuths is not uniform, as shown in Figure 5.11.1 below, but has preferential directions along the climatologically dominant zonal trades and mid-latitude westerlies. This is unfortunate, because the global mean backscatter in Eq. (5.11.7) is affected by the harmonic terms of the ocean response (i.e., the global mean backscatter increases/decreases as measurements align preferentially along the upwind/crosswind directions), and its determination becomes sensitive to uncertainties in the a priori distribution of NWP wind azimuths that is used as reference.

	<h2 style="text-align: center;">The SCIRoCCo Scatterometry Handbook</h2>	Ref:	SCI-PUB-14-0001-v01
		Issue:	6
		Date:	10/10/2017
		Proj:	SCIRoCCo Scatterometer Instrument Competence Centre

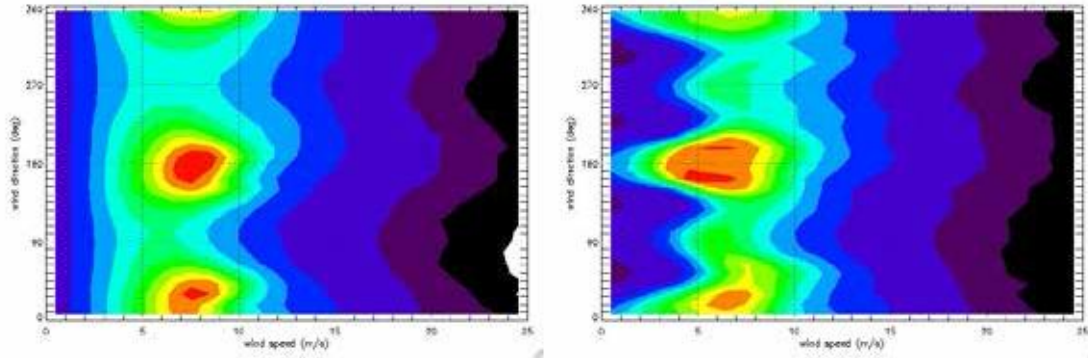


**Figure 5.11.1.** Joint PDF  $NN(vv, \phi\phi)$  of ocean NWP wind speeds and wind azimuths relative to the right mid antenna beam of ASCATA (25 km spacing) over the year 2014 from NWP (left panel) and scatterometer (right panel) datasets. Zonal trades and westerlies are aliased (via ascending and descending passes of a near-polar instrument) into histogram peaks at about 0 and 180 degrees. A discussion on differences between the NWP and scatterometer wind PDFs is deferred to Section 5.11.3.

To reduce the sensitivity to the harmonic terms of the ocean response, compensation weights  $ww(vv, \phi\phi)$  are introduced based on prior knowledge of NWP wind statistics such that:

$$ww(vv, \phi\phi)NN(\phi\phi|vv) = 1/(2\pi) \quad (5.11.10)$$

Introducing compensation weights, i.e. forcing a uniform distribution in the wind direction, is important to obtain results that are less sensitive to errors in NWP wind direction (See Section 5.11.5.1). With a forced uniform distribution in wind direction, the azimuthally averaged backscatter from the ocean yields the azimuthally isotropic term:

$$\langle ww(vv, \phi\phi) \cdot zz(vv, \phi\phi) \rangle_{\phi\phi} = \int ww(vv, \phi\phi) \cdot NN(\phi\phi|vv) \cdot zz(vv, \phi\phi) s s \phi\phi = \int_0^{2\pi} aa_0(vv) \quad (5.11.11)$$

The global average of the azimuthally isotropic backscatter is obtained after averaging the wind-speed dependent isotropic  $aa_0(v)$  coefficients over the wind speed climatology as:

$$\langle aa_0 \rangle = \int NN(vv) \cdot aa_0(vv) s s vv \quad (5.11.12)$$

Where  $NN(v)$  is the marginal PDF of a priori wind speeds, shown in Figure 5.11.2.

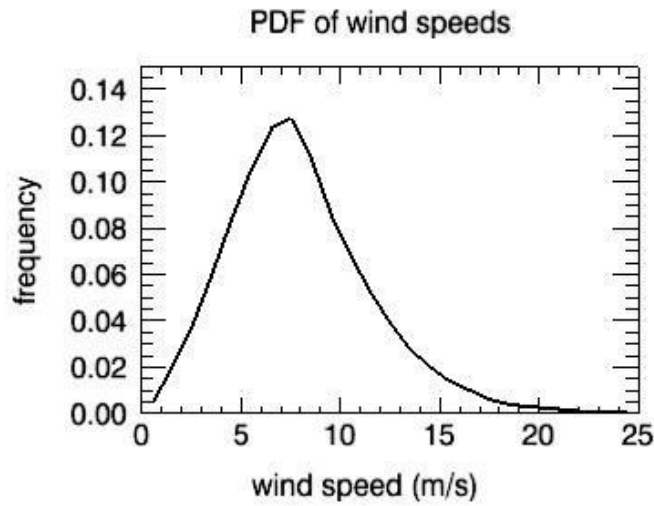


Figure 5.11.2. Marginal PDF  $N(v)$  of ocean wind speeds from NWP model.

The global mean  $\langle a_0 \rangle$  coefficients, calculated for each beam and incidence angle, may be transformed back to the linear  $\sigma\sigma^0$  space to obtain the global mean  $\langle B_0 \rangle$  coefficients:

$$\langle BB_0 \rangle = [\langle aa_0 \rangle / 2]^{1.6} \tag{5.11.13}$$

Using the following relations:

$$\begin{aligned} B_0 &= [a_0 / 2]^{1.6} \\ B_1 &= 2a_1 / a_0 \\ B_2 &= 2a_2 / a_0 \end{aligned} \tag{5.11.14}$$

Finally, the beam and incidence angle dependent calibration coefficients  $\Delta_{ddd}$  may be expressed in dBs as:

$$\Delta_{ddd} = 10 \cdot \text{CCffll}_{10}(1 + \delta\delta) \approx 1.6 \cdot \left[ \frac{\langle aa^{SSbbss} \rangle_{ddd} - \langle aa^{SSmm} \rangle_{ddd}}{\langle aa^{SSmm} \rangle_{ddd}} \right] = \langle BB^{SSbbss} \rangle_{ddd} - \langle BB^{SSmm} \rangle_{ddd} \tag{5.11.15}$$

Averaging over wind directions and wind speeds occurs in  $z$  space, whereas the instrument calibration coefficient  $\delta\delta$  is assumed linear in  $\sigma^0$ . Averaging backscatter over wind directions in  $z$  space is necessary to eliminate the dependence on the harmonic terms of the ocean response, while averaging over wind speeds in  $z$  space is necessary to suppress the effect of collocation pseudobias (see Section 5.11.5.2). Fortunately, the calibration offset  $\delta\delta$  may be considered linear both in  $z$  space and  $\sigma^0$  space in the small  $\sigma^0$  approximation.

$$z_{SSbbss} = [(1 + \delta\delta) \cdot \sigma^0]^{0.625} \approx (1 + 0.625 \cdot \delta\delta) \cdot z$$

	<b>The SCIROCCo</b> <b>Scatterometry Handbook</b>	<b>Ref:</b>	SCI-PUB-14-0001-v01
		<b>Issue:</b>	6
		<b>Date:</b>	10/10/2017
		<b>Proj:</b>	SCIROCCo Scatterometer Instrument Competence Centre

### 5.10.2 Application

Figure 5.11.3 details the steps required to perform ocean calibration. The required inputs are the scatterometer sigma naughts  $\sigma_0^{OBS}$  and the collocated model winds. Note that the current GMF (CMOD5n or CMOD7) only takes stress (or neutral) equivalent 10-meter winds U10S (or U10N) as input. If only 10-meter winds U10 are provided, then a correction of 0.2 m/s should be added to U10 in order to generate an approximate U10S (U10N). A preliminary quality control QC filter is applied to discard data of poor quality. The QC filter typically rejects about 60% of the collocation points, mostly due to the land mask (60-70% of rejections), the [55°S-65°N] latitude mask for sea ice (30-40% of rejections) and the data quality mask (0.5-5% of rejections, mainly on sigma naught and  $K_p$  quality). Note that the mask for land rejection at KNMI's NOC implementation also excludes the large North American and Siberian lakes.

The input model winds that pass the filter are used to build the joint PDF of wind speeds and azimuths  $N(v, \ell_{beam})$  for each beam, along with the simulated sigma naughts  $\sigma_0^{SIM}$  using a reference GMF. Currently, the joint PDF of model winds is assumed to not vary appreciably with incidence angle (i.e. WVC number) – the only distinction made between left and right sides of the instrument. The joint PDF is calculated from the histogram of model winds seen by the (right or left) mid beams (regardless of WVC number), then shifted in azimuth by  $\pm 45$  degrees for the fore and aft beams. The weight factors  $w(v, \ell_{beam})$  necessary to force a uniform distribution in wind direction are estimated from the inverse of this joint PDF following Eq. (5.11.10).

Next, both observed  $\sigma_0^{OBS}$  and simulated  $\sigma_0^{SIM}$  sets are transformed into z-space using Eq. (5.11.2), and they become temporally averaged using a grid of wind speed bins 1 m/s wide and wind azimuth bins 12 degrees wide, as a function of WVC number and beam, over the entire study period. The azimuthal weighting is then performed as in Eq. (5.11.11) using the model wind statistics calculated earlier, to obtain the azimuthally isotropic  $a_0^{OBS}(v)$  and  $a_0^{SIM}(v)$  backscatter coefficients for both the observed and simulated datasets as a function of wind speed. At this point, one may check the resulting  $B_0(v)$  coefficients as a function of wind speed from Eq. (5.11.13), or continue averaging over wind speeds as in Eq. (5.11.12) to obtain the globally averaged values  $\langle a_0^{OBS} \rangle$  and  $\langle a_0^{SIM} \rangle$  as a function of incidence

angle and beam, out of which the calibration coefficients  $\Delta_{ddd}$  are obtained.

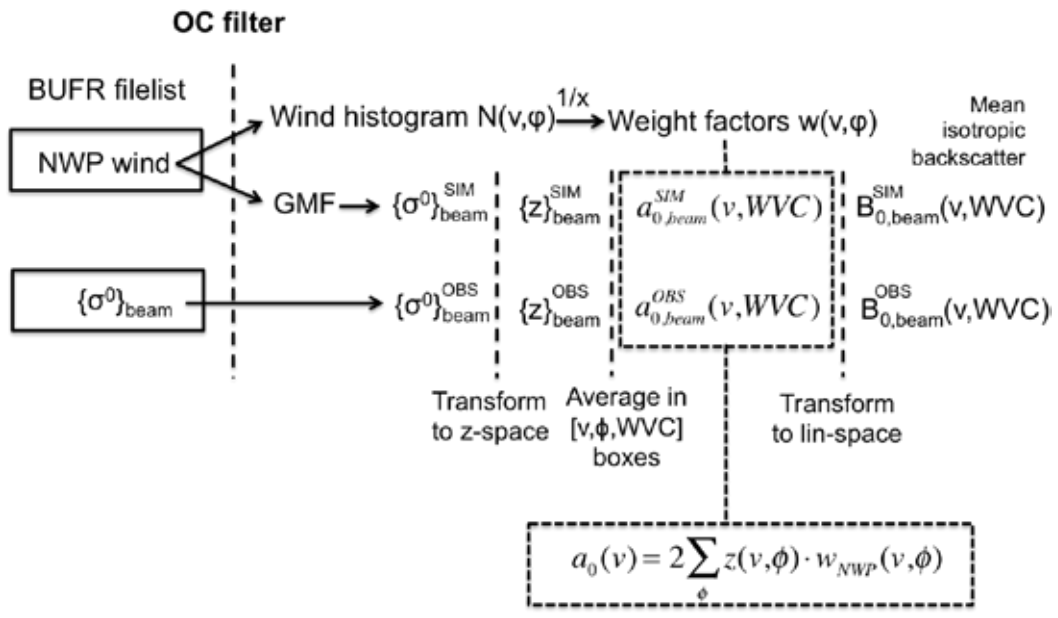


Figure 5.11.3. Diagram of the NWP ocean calibration (NOC) for a fixed WVC number and a given antenna beam.

The difference between measured and simulated global isotropic backscatter coefficients for the fore, mid and aft antennas of ASCAT A over 2014 is shown in Fig. 5.11.4.

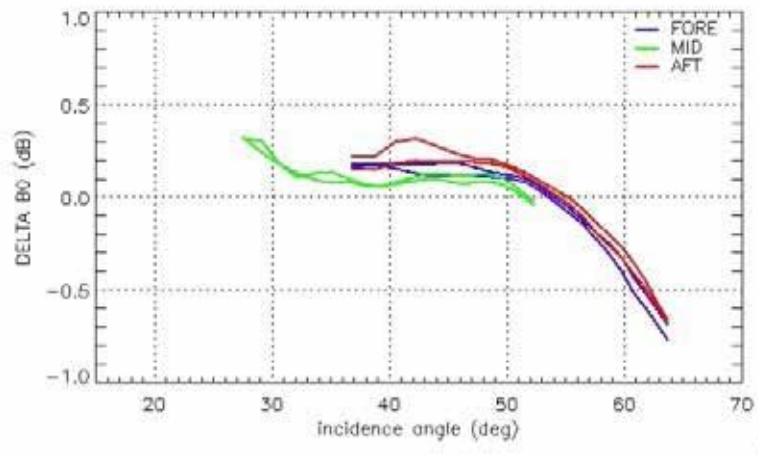


Figure 5.11.4. NOC offsets: global average backscatter differences  $(\Delta_{ddd=B_0}^{OBS} - B_0^{SIM})_{dB}$  relative to the reference GMF frame CMOD5n for ASCAT A data (25 km spacing) and collocated operational ECMWF 10-m winds over 2014. These results are similar to those published in (Verspeek, 2012) for ASCAT A data (12 km spacing) for the period Sep 2008 to Sep 2009.





	<p>The SCIRoCCo Scatterometry Handbook</p>	Ref:	SCI-PUB-14-0001-v01
		Issue:	6
		Date:	10/10/2017
		Proj:	SCIRoCCo Scatterometer Instrument Competence Centre

Lastly, note that the scatterometer directional wind distributions, like those shown in Figure 5.11.1, are not in all cases to be taken as good proxies for the underlying true distributions. Particularly at low winds, systematic accumulations in scatterometer wind distributions are observed along upwind, downwind and crosswinds directions relative to the mid beam<sup>1</sup>.

### 5.10.3.2 Sensitivity to NWP wind speed error

The presence of random Gaussian errors in the reference NWP wind speed components is introducing a bias in the reference distribution of wind speeds, and apparent wind-speed dependent biases in the calibration coefficients also known as pseudobiases (See Section 5.11.5.2). Pseudobiases are of small import, since they balance out when averaged over the collocating wind speed distribution [as done in Eq. (5.11.12)], but correcting for the bias in the reference wind speed distribution requires more precise knowledge of the NWP error characteristics. Indeed, random wind vector component errors of about 1.5 m/s in the NWP reference system will act to increase the apparent reference mean wind speed by about 0.1 m/s, with an approximate equivalent increase of about 0.1 dB in the reference mean backscatter.

### 5.10.3.3 Sensitivity to non-linearity and GMF error

Detector non-linearities (which refer to the fact that the calibration offset  $\delta\delta$  in Eq. (5.11.1) may be a function of sigma naught) and GMF errors will both produce wind speed dependent biases, which will be difficult to separate from pseudobiases in the wind speed dependent calibration curves (see Section 5.11.5.2) without more precise knowledge of the error characteristics of the NWP reference system. This issue cannot be investigated further within NOC. A new methodology based on cone metrics is being developed in the hopes of providing more information.

### 5.10.3.4 Sensitivity to QC filter settings

The NOC calibration coefficients are sensitive to the preliminary QC filter settings, in particular to the activation of level 2 flags such as the KNMI QC flag, the Variational QC flag, or the ERS ASPS NCD-PCD2 summary flag, all of which reflect conservative metrics related to distance to cone for rain flagging, or low wind speed rejections.

---

<sup>1</sup>This behavior may be associated to a known deficiency of CMOD5n, which appears to be biased low at low winds by a few dBs. Wind distributions for the right-mid beam show suppressed retrievals at 45, 135, 225 and 315 degrees, at locations where MLE distances suffer the stronger gradients and where no local extremes can be found.



The KNMI QC flag is activated when the distance to the GMF is too large (effective rain and wind variability flag) or the measurement noise is too large. The Variational QC flag is activated when the retrieved wind solution is spatially inconsistent with the surrounding wind field. The monitoring QC flag is activated when the general offset to the model wind field is too large (in case of instrument anomaly). The ERS ASPS NCD-PCD2 summary flag is activated when the distance to the GMF is too large, the measurement noise is too large, the offset to the model wind field is too large, or the wind speed is too low (less than 3 m/s).

Figure 5.11.6 below shows the differences in calibration coefficients between runs using different QC filter settings (see Table 5.11.2) on an otherwise identical dataset – ASCAT A (25 km spacing) over 2014.

**Table 5.11.2** Summary of NOC runs using different QC filter settings

RUN1	No level 2 QC	
RUN2	KNMI QC flag	Applies KNMI QC flag
RUN3	KNMI + Var QC flags	Applies Var QC flag
RUN4	KNMI + Var QC + Low wind	Winds $\leq 3$ m/s discarded

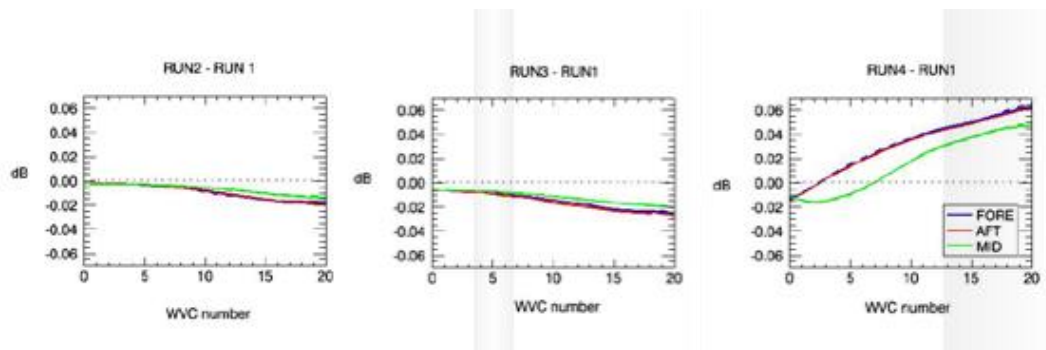


**Figure 5.11.6.** Differences in NOC calibration coefficients ( $\Delta_{ddd1} - \Delta_{ddd2}$ ) between runs with different QC filter settings (see Table 1) on ASCAT A data (25 km spacing) over 2014.

The “No level 2 QC” control run (RUN1) is filtering data on the simplest basis:

- Presence of ( $\sigma$  naught and kp) on all three beams
- Presence of (azimuth and incidence angle) on all three beams
- Presence of background wind (speed and direction)
- NO land

	<h1>The SCIRoCCo Scatterometry Handbook</h1>	<b>Ref:</b>	SCI-PUB-14-0001-v01
		<b>Issue:</b>	6
		<b>Date:</b>	10/10/2017
		<b>Proj:</b>	SCIRoCCo Scatterometer Instrument Competence Centre

- NO big lakes in USA/Asia
- NO ice / latitude mask: DISCARD lats outside of [55S, 65N]

The other QC flags (KNMI QC, Var QC and the low wind rejection) are applied in a cumulative manner. We note that the KNMI QC, Variational QC (and Monitoring QC, not shown) flags do not change the calibration coefficients by more than 0.02 dB, which is well within a 0.1 dB budget for precision. Thus their application is likely to be safe. However, the application of the low wind rejection flag ( $\leq 3$  m/s) is producing notably larger calibration coefficients, with differences increasing with incidence angle, and reaching up to 0.08 dB relative to RUN2 and RUN3. This behavior is caused by changes in the wind dependent calibration coefficients at low winds only, and is deemed unacceptable. Thus it is recommended to avoid using the low wind speed rejection flags as part of the NOC QC filter settings.

### 5.10.3.5 Temporal stability of backscatter

Random NWP wind speed and direction errors influence the accuracy of the NOC. Triple collocation studies show that NWP wind errors may undergo small variations with time and similar variations may thus occur in NOC. A time series of NOC calibration coefficients has been estimated using successive monthly periods over the year 2014 for the ASCAT A scatterometer and the results are shown in Figure 5.11.7. The relative differences between beams look rather constant during the year, with a seasonal variation that seems anti-correlated with the global mean wind speed over the ocean, featuring peak-to-peak amplitudes of 0.1 dB with minima in summer/winter and maxima in spring/fall<sup>2</sup>. Note that a shift in NOC biases of the order of 0.1 dB corresponds to approximately 0.1 m/s bias in wind speed.

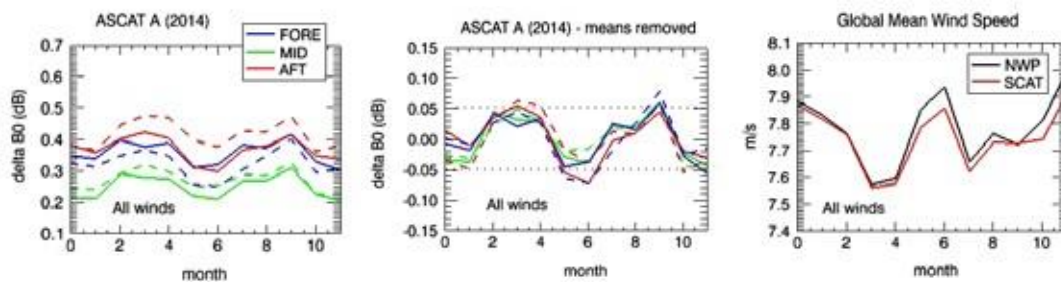


**Figure 5.11.7.** Time series of the global average backscatter differences ( $B_0^{OBS}$  minus  $B_0^{SIM}$ ) relative to the reference GMF frame CMOD5n for ASCAT A data (25 km spacing) (averaged over incidence angles between 37 and 52 degrees).

<sup>2</sup> Also note that ASCAT-A experienced a beam pattern anomaly in September 2014 and a general 0.08 decrease in backscatter in October 2014.

	<h2 style="text-align: center;">The SCIRoCCo Scatterometry Handbook</h2>	<b>Ref:</b>	SCI-PUB-14-0001-v01
		<b>Issue:</b>	6
		<b>Date:</b>	10/10/2017
		<b>Proj:</b>	SCIRoCCo Scatterometer Instrument Competence Centre

Besides random NWP errors, systematic NWP errors may also occur. Above-mentioned triple collocation studies often show underestimation by NWP wind speeds of 2-5%. Reference to moored buoys in triple collocation provides an absolute reference for retrieving scatterometer winds through a GMF. Other systematic differences are due to ocean currents and other poorly represented small-scale processes in NWP models, such as moist convection and atmospheric boundary layer parameterizations (Sandu et al., 2013). These latter (and more modest) effects are currently treated as part of the random NWP wind errors in triple collocation and global NOC.

#### 5.10.4 Concluding remarks

The methodology behind Numerical Weather Prediction (NWP) ocean calibration, which is currently the baseline for calibration before scatterometer wind retrieval, is described in detail. NWP ocean calibration (NOC) compares the mean backscatter from the global oceans measured by a scatterometer against an equivalent quantity derived from a reference GMF acting on a reference NWP wind distribution, as a function of beam and incidence angle. In order to remove the dependence of the azimuthally averaged backscatter on the amplitude of the directional wind distribution, and thereby minimize the method's overall sensitivity to directional wind uncertainties, both observed and simulated values are forced into uniform wind direction distributions using statistical weights derived from the reference NWP.

NOC is a simple but powerful method to perform relative calibration of scatterometer inter-beam or cross-instrumental biases, providing improved geophysical retrievals and an estimated accuracy of 0.1-0.2 dB using as little as one month of data. NOC accuracy is in line with that provided by other methods (e.g. rain forest calibration or absolute calibration with transponders), which is also about 0.1-0.2 dB.

The main limitation to NOC accuracy lies in the error characteristics of the reference NWP wind distributions, which are difficult to improve. Among the main issues currently limiting the NOC method we find a) sensitivity to NWP wind direction errors, which may cause calibration biases of up to -0.1 dB in the mid beams, without substantially affecting the fore/aft beams; and b) sensitivity to NWP wind speed errors, which may cause calibration biases of up to 0.1 dB in all beams. Due to seasonal variability in NOC coefficients, which feature a characteristic annual amplitude of about 0.05 dB depending on yet unresolved causes, it is recommended to run NOC over a full year for studies on instrument stability. The effects of GMF error and calibration non-linearity on NOC (which operates under the assumption of a constant beam offset) are difficult to evaluate at this point without resort to more refined approaches, such as cone metrics. Ways to improve the accuracy of the NOC method currently point towards the utilization of better reference GMFs, and the utilization of the NOC method in a relative fashion using any two simultaneous (not necessarily collocated) scatterometer records, which should result in the cancellation of common NWP wind and GMF errors.

	<p>The SCIRoCCo Scatterometry Handbook</p>	Ref:	SCI-PUB-14-0001-v01
		Issue:	6
		Date:	10/10/2017
		Proj:	SCIRoCCo Scatterometer Instrument Competence Centre

## 5.10.5 NOC-related detailed calculations

### 5.10.5.1 Compensating weights

Forcing a uniform distribution in wind direction (via compensation weights) has more advantages than direct averaging when suppressing errors due to uncertainty in the reference distribution of wind directions. In direct averaging one has:

$$\langle ZZ_{SSmm} \rangle = \iint NN_{SSmm}(vv, \phi\phi) \cdot ZZ_{SSmm}(vv, \phi\phi) SSvvS\phi\phi = \int NN_{SSmm}(vv) \langle ZZ_{SSmm}|vv \rangle_{\phi\phi} SSvv \quad (A1)$$

$$\langle ZZ_{SSbbss} \rangle = \iint NN_{SSbbss}(vv, \phi\phi) \cdot ZZ_{SSbbss}(vv, \phi\phi) SSvvS\phi\phi = \int NN_{SSbbss}(vv) \langle ZZ_{SSbbss}|vv \rangle_{\phi\phi} SSvv \quad (A2)$$

Where

$$\langle ZZ_{SSmm}|vv \rangle = \int NN_{SSmm}(\phi\phi|vv) \cdot ZZ_{SSmm}(vv, \phi\phi) S\phi\phi \quad (A3)$$

$$\langle ZZ_{SSbbss}|vv \rangle = \int NN_{SSbbss}(\phi\phi|vv) \cdot ZZ_{SSbbss}(vv, \phi\phi) S\phi\phi \quad (A4)$$

Assuming unbiased systems ( $\delta\delta = 0 \rightarrow ZZ_{SSbbss} = ZZ_{SSmm}$ ) for this particular example:

$$\langle ZZ_{SSbbss}|vv \rangle_{\phi\phi} = \int NN_{SSbbss}(\phi\phi|vv) \cdot ZZ_{SSmm}(vv, \phi\phi) S\phi\phi \quad (A5)$$

Where

$$ZZ_{SSmm}(vv, \phi\phi) = \frac{1}{2} \overline{aa^2}(vv) + aa(vv) cffs\phi\phi + aa(vv) cffs2\phi\phi \quad (A6)$$

So, even if the observation system  $ZZ_{SSbbss}$  is unbiased relative to the reference system  $ZZ_{SSmm}$ , there will arise a bias between the sample averages  $\langle ZZ_{SSbbss}|vv \rangle$  and  $\langle ZZ_{SSmm}|vv \rangle$  caused by the difference between the reference and actual sample distributions,  $NN_{SSmm}(\phi\phi|vv)$  and  $NN_{SSbbss}(\phi\phi|vv)$ , captured by the harmonic ocean response. Suppose that we take:

$$NN_{SSmm}(\phi\phi|vv) = \frac{1}{2} \overline{1 + MM cffs\phi\phi + NN cffs2\phi\phi} \quad (A7)$$

$$NN_{SSbbss}(\phi\phi|vv) = C_0 \cdot NN_{SSmm}(\phi\phi|vv) (1 + ss \cdot cffs\phi\phi + ss \cdot cffs2\phi\phi) \quad (A8)$$

Where  $C_0 \sim 1$  is a constant such that  $\int NN_{SSbbss}(\phi\phi|vv) S\phi\phi = 1$ , and the fractional uncertainty in the reference distribution of wind directions  $NN_{SSmm}(\phi\phi|vv)$  relative to the actual distribution  $NN_{SSbbss}(\phi\phi|vv)$  is expressed in terms of Fourier projections of amplitude  $m$  and  $n$  onto the ocean harmonic terms  $\cos(\delta)$  and  $\cos(2\delta)$  respectively as:

	<h1 style="text-align: center;">The SCIRoCCo Scatterometry Handbook</h1>	<b>Ref:</b>	SCI-PUB-14-0001-v01
		<b>Issue:</b>	6
		<b>Date:</b>	10/10/2017
		<b>Proj:</b>	SCIRoCCo Scatterometer Instrument Competence Centre

$$SS = \frac{1}{2\pi} \int_0^{2\pi} NN_{SSbbs}(\phi|v) / NN_{SSmm}(\phi|v) \cdot cff_{ss} \phi \phi \phi \phi$$

$$SS = \frac{1}{2\pi} \int_0^{2\pi} NN_{SSbbs}(\phi|v) / NN_{SSmm}(\phi|v) \cdot cff_{ss} 2\phi \phi \phi \phi$$

In the direct averaging case, the relative error caused by the fractional uncertainty ( $m, n$ ) in the reference distribution of wind directions is:

$$\frac{\langle \frac{d}{dt} \langle NN_{SSbbs} | v \rangle_{\phi} - \langle \frac{d}{dt} NN_{SSbbs} \rangle_{\phi} \rangle}{\langle NN_{SSbbs} | v \rangle_{\phi}} = \frac{m}{2} (BB_1 + MM_0) + \frac{n}{2} (BB_2 + NN_0) \quad (A9)$$

=

Which depends on the ocean harmonic terms ( $B_1, B_2$ ) as well as on the directional wind modulation ( $M_0, N_0$ ). After introducing compensation weights:

$$ww(\phi|v) NN_{SSmm}(\phi|v) = \frac{1}{2\pi}$$

One ends up with compensated weight averages of the form (still unbiased systems):

$$\langle ww \cdot NN_{SSmm} | v \rangle = \int NN_{SSmm}(\phi|v) \cdot ww(\phi|v) \cdot NN_{SSmm}(v, \phi) \phi \phi \phi \phi = \frac{1}{2\pi} \int NN_{SSmm}(v, \phi) \phi \phi \phi \phi = \frac{1}{2} aa_0(v)$$

$$\langle ww \cdot NN_{SSbbs} | v \rangle = \frac{1}{2\pi} \int NN_{SSbbs}(\phi|v) \cdot ww(\phi|v) \cdot NN_{SSmm}(v, \phi) \phi \phi \phi \phi = \frac{1}{2\pi} \int NN_{SSbbs}(v, \phi) \phi \phi \phi \phi \approx \frac{1}{2} (v) \frac{SS}{aa} (v) \frac{SS}{aa} v$$

In this case, the relative error caused by fractional uncertainty in the reference NWP distribution of wind directions (relative to the actual wind distribution that the scatterometer represents) is found to be:

$$\frac{\langle \frac{d}{dt} \langle NN_{SSbbs} | v \rangle_{\phi} - \langle \frac{d}{dt} NN_{SSbbs} \rangle_{\phi} \rangle}{\langle NN_{SSbbs} | v \rangle_{\phi}} = \frac{m}{2} BB_1 + \frac{n}{2} BB_2 \quad (A10)$$

=

Which only depends on the ocean harmonic terms ( $B_1, B_2$ ). Compare Eq.(A9) to Eq.(A10) to see that introducing compensation weights reduces (although does not eliminate) the sensitivity of the azimuthally isotropic backscatter

coefficient  $a_0(\nu)$  estimated by the NOC technique to directional wind uncertainty. Compensation weights eliminate the dependence of the azimuthally averaged backscatter on the amplitudes of the directional wind distribution  $(M_0, N_0)$ , but not its sensitivity to directional wind distribution errors  $(m, n)$ .

	<p>The SCIRoCCo Scatterometry Handbook</p>	Ref:	SCI-PUB-14-0001-v01
		Issue:	6
		Date:	10/10/2017
		Proj:	SCIRoCCo Scatterometer Instrument Competence Centre

Uniform distribution in wind directions: Introducing compensation weights is equivalent to binning the backscatter samples into a regular azimuth grid using NWP collocation, to perform the average over the gridded values. The direct average for a given wind speed is performed over a total number of samples  $N(v)$  as:

$$\frac{1}{N(v)} \sum_{SS=1}^{NN(v)} ZZ_{SS} = \frac{1}{N(v)} \sum_{SS=1}^{NN(v)} \sum_{kk=1}^{N_{\phi}} ZZ_{kk} \quad [N1]$$

$$\langle zz(v, \phi) \rangle_{\phi} = \frac{1}{N(v)} \sum_{SS=1}^{NN(v)} ZZ_{SS} = \frac{1}{N(v)} \sum_{SS=1}^{NN(v)} \sum_{kk=1}^{N_{\phi}} ZZ_{kk}$$

But this result is sensitive to preferential alignments of the samples along directions with stronger or weaker backscatter. If we distribute the total number of samples  $N(v)$  over a number of azimuth bins  $N_{\phi}$  with  $N_{\phi i}$  samples each, such that  $N(v) = \sum_{N_{\phi}} N_{\phi i}$ , with compensation weights  $w_i$ , such that  $w_i N_{\phi i} = N(v)/N_{\phi}$ , then we will have:

$$\frac{1}{N(v)} \sum_{SS=1}^{NN(v)} ZZ_{SS} = \frac{1}{N(v)} \sum_{SS=1}^{NN(v)} \sum_{kk=1}^{N_{\phi}} \frac{1}{N_{\phi}} ZZ_{kk} \quad [N2]$$

$$\langle ww(v, \phi) \cdot zz(v, \phi) \rangle_{\phi} = \frac{1}{N(v)} \sum_{SS=1}^{NN(v)} WW_{SS} \cdot ZZ_{SS} = \frac{1}{N(v)} \sum_{SS=1}^{NN(v)} \sum_{kk=1}^{N_{\phi}} \frac{1}{N_{\phi}} ZZ_{kk}$$

The weight-compensated mean is equivalent to the average over the binned backscatter grid. Clearly, the grid average is not sensitive to preferential sample alignments, as long as the grid spacing is uniform.

### 5.10.5.2 Pseudobiases

Pseudobiases arise whenever a collocation is performed against a noisy reference system. Noise excursions in the collocating (i.e. NWP wind) system act to agglomerate subsets of collocations asymmetrically in a collocation bin, introducing non-linear biases that depend on the true variable distribution and the collocating system noise properties, as we shall see next. Figure B1 shows the ocean calibration bias for ASCAT A (the collocated system) over the year 2014 as a function of wind speed, revealing the typical signature of pseudobiases due to random NWP model wind errors (i.e. large positive errors at low wind speeds, small negative errors at high wind speeds, and vanishing around the mode of the wind speed distribution at 8 m/s).

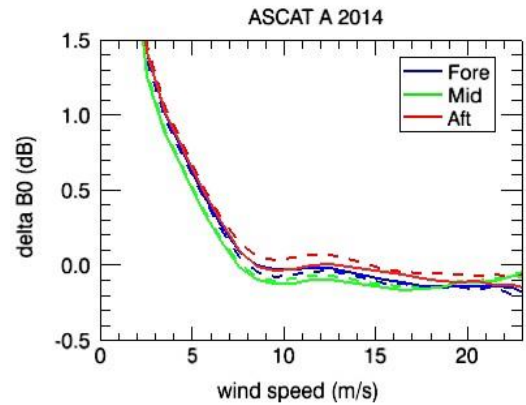


**Figure B1.** Global average backscatter differences ( $\Delta_{add} = B_0^{OBS} - B_0^{SIM}$ ) relative to the reference GMF frame CMOD5n for ASCAT A data (25 km spacing) over 2014 as a function of wind speed (averaged over incidence angles between 37 and 52 degrees). Left side beams are dashed.

Suppose that a joint PDF distribution  $p(x,y)$  is formed after collocation of scatterometer observations ( $x$ ) and NWP simulations ( $y$ ). This joint PDF distribution is a function of the distribution  $p(t)$  of the true variable  $t$  (which at this stage could either refer to wind speed or backscatter) and the error characteristics of both systems (Stoffelen, 1998):

$$pp(xx, yy) = \int_{-\infty}^{\infty} pp(xx|tt) \cdot pp(yy|tt) \cdot pp(tt) sstt \tag{B1}$$

Where  $p(x|t)$  and  $p(y|t)$  refer to the error distributions of observations and simulations around the true value, i.e. they represent observation and simulation noise and biases, although the collocating system is assumed unbiased:

$$\langle xx|tt \rangle = \int_{-\infty}^{\infty} pp(xx|tt) \cdot xx sstt = tt + bsstt \tag{B2}$$

$$\langle yy|tt \rangle = \int_{-\infty}^{\infty} pp(yy|tt) \cdot yy sstt = tt \tag{B3}$$

The mean collocated quantity (observations) over a given subrange of collocating values (simulations) is calculated as:

$$\frac{1}{\int_{-\infty}^{\infty} pp(xx, yy) \cdot xx sstt} \tag{B4}$$

$$\langle xx|yy \rangle = \int_{-\infty}^{\infty} pp(xx, yy) \cdot xx sstt$$

$$pp(yy) = \int_{-\infty}^{\infty} pp(xx, yy) sstt \tag{B5}$$

In a collocation analysis, one usually looks at the difference between the mean observed quantity in a collocation bin and the collocating bin value:

$$DDSSDDD(yy) = \langle xx|yy \rangle - yy \tag{B6}$$



	<h1>The SCIRoCCo Scatterometry Handbook</h1>	Ref:	SCI-PUB-14-0001-v01
		Issue:	6
		Date:	10/10/2017
		Proj:	SCIRoCCo Scatterometer Instrument Competence Centre

The mean observed quantity in a collocation bin is derived by inserting Eq.(B1) into Eq.(B4) and using Eq.(B2) above as:

$$\begin{aligned}
 \langle xx|yy \rangle &= \frac{1}{pp(yy)} \int_{-\infty}^{\infty} \int_{-\infty}^{\infty} pp(xx|tt) \cdot pp(yy|tt) \cdot pp(tt) sstt \cdot xx \, dx \, dt \\
 &= \frac{1}{pp(yy)} \int_{-\infty}^{\infty} \int_{-\infty}^{\infty} pp(xx|tt) \cdot xx \, dx \, dt \int_{-\infty}^{\infty} pp(yy|tt) \cdot pp(tt) sstt \, dt \\
 &= \frac{1}{pp(yy)} \int_{-\infty}^{\infty} (tt + bbssaass(tt)) \cdot pp(yy|tt) \cdot pp(tt) sstt \, dt
 \end{aligned} \tag{B7}$$

That is, the mean collocated quantity in a collocation bin  $\langle x|y \rangle$  results from the average of samples of the variable  $t$  collected by the collocating variable  $y$  along its noise excursions  $p(y|t)$ , weighted by the chance  $p(t)$  that a particular true value  $t$  is sampled.

Bringing this back to Eq. (B6) results in:

$$DDSSDDDD(yy) = \langle xx|yy \rangle - yy = PPBB(yy) + bbssaass(yy) \tag{B8}$$

Where:

$$\begin{aligned}
 PPBB(yy) &= \frac{1}{pp(yy)} \int_{-\infty}^{\infty} \int_{-\infty}^{\infty} tt \cdot pp(yy|tt) \cdot pp(tt) sstt \, dt \, dx - yy \\
 bbssaass(yy) &= \frac{1}{pp(yy)} \int_{-\infty}^{\infty} bbssaass(tt) \cdot pp(yy|tt) \cdot pp(tt) sstt \, dt
 \end{aligned}$$

The first term  $PB(y)$  is referred to as the pseudobias – which results from aggregating a skewed distribution  $p(y|t)p(t)$  of values in a collocation bin. If the collocation errors  $p(y|t)$  are symmetric, the agglomeration of samples in the collocation bin will be skewed towards the mode of the true distribution  $p(t)$ . Note that the pseudobias  $PB(y)$  would

vanish if the collocating system were noiseless [i.e. introduce  $pp(yy|tt) = \delta\delta(tt - yy)$  in Eq.(B8)]. With a noisy collocating system, if the distribution  $p(t)$  of the true variable were uniform, then the pseudobias would also vanish, provided that the collocating error distribution is symmetric with respect to the true value (i.e.  $pp(yy|tt) = pp(tt|yy)$ , as with a Gaussian distribution). Thus we see that two factors are necessary for the formation of collocation pseudobiases: that the collocating system is noisy, and that the underlying distribution of the true variable is not uniform.

The second term  $bbssaass(yy)$  in Eq.(B8) is a smoothed version of the actual observation  $bbssaass(yy)$ , only convolved with a weighted (skewed) version of the collocating error distribution. If the observation bias were a smooth function of  $t$ , with a characteristic length scale much larger than the size of the collocating system noise (i.e. the width of  $p(y|t)$ ), then this second term would already constitute a reasonable approximation to the observation bias. If the observation bias were a constant, then:

$$\begin{aligned}
 bbssaass(yy) &= bbssaass \cdot \frac{1}{pp(yy)} \int_{-\infty}^{\infty} pp(yy|tt) \cdot pp(tt) sstt \, dt = bbssaass
 \end{aligned}$$

	<h1>The SCIRoCCo Scatterometry Handbook</h1>		Ref:	SCI-PUB-14-0001-v01
			Issue:	6
			Date:	10/10/2017
			Proj:	SCIRoCCo Scatterometer Instrument Competence Centre

An important property of pseudobiases  $PB(y)$  is that they vanish when averaged over the distribution of the collocating variable  $p(y)$ , that is:

$$\begin{aligned}
 \langle xx|yy \rangle \cdot pp(yy) \text{ ssyy} &= \\
 &= \int_{-\infty}^{\infty} \int_{-\infty}^{\infty} \frac{1}{pp(yy)} (tt + bbssaass(tt)) \cdot pp(yy|tt) \cdot pp(tt) \text{ sstt} \cdot pp(yy) \text{ ssyy} = \\
 &= \int_{-\infty}^{\infty} (tt + bbssaass(tt)) \cdot pp(yy|tt) \text{ ssyy} \cdot pp(tt) \text{ sstt} = \\
 &= \int_{-\infty}^{\infty} (tt + bbssaass(tt)) \cdot pp(tt) \text{ sstt} = \langle tt \rangle + \langle bbssaass \rangle
 \end{aligned} \tag{B9}$$

Where we have used the normalization property of the marginal probability:

$$\int_{-\infty}^{\infty} pp(yy|tt) \text{ ssyy} = 1$$

Here  $\langle \text{bias} \rangle$  is the mean observation bias averaged over the true variable distribution:

$$\langle bbssaass \rangle = \int_{-\infty}^{\infty} bbssaass(tt) \cdot pp(tt) \text{ sstt}$$

Note that all reference to collocating system noise has been eliminated from Eq. (B9). That is, we go from arranging observations in terms of the noisy collocating variable  $y$  as:

$$\langle xx|yy \rangle = yy + PPBB(yy) + \langle bbssaass \rangle \tag{B10}$$

Where pseudobiases must somehow be accommodated in the picture, to arranging observations in terms of the true variable  $t$  as:

$$\langle xx \rangle = \langle tt \rangle + \langle bbssaass \rangle \tag{B11}$$

Where in Eq. (B11) we have used the fact that:

$$\langle xx \rangle = \int_{-\infty}^{\infty} \int_{-\infty}^{\infty} \langle xx|yy \rangle \cdot pp(yy) \text{ ssyy} = \int_{-\infty}^{\infty} \int_{-\infty}^{\infty} pp(xx, yy) \cdot xx \text{ ssxx} \text{ ssyy}$$

The description afforded by Eq.(B11) is free from pseudobiases, but does not provide a picture of the dependence of the actual observation bias on the collocating variable  $y$ , as only a mean averaged quantity  $\langle \text{bias} \rangle$  is produced. However, when the noise properties of the collocating system are well known, then pseudobiases can be simulated

and removed in order to obtain an approximate estimate of the wind speed or backscatter dependent  $\langle bbssaass \rangle$ .

Even if collocation errors (i.e. pseudobiases) balance out when averaging over the distribution of the collocating variable, an error term arising from uncertainty in collocating PDF distribution remains, that is:

$$\int_{-\infty}^{\infty} \langle bbssaass \rangle \cdot pp(yy) \text{ ssyy} = \int_{-\infty}^{\infty} (PPBB(yy) + \langle bbssaass \rangle) \cdot pp(yy) \text{ ssyy} =$$

	<b>The SCIRoCCo Scatterometry Handbook</b>		<b>Ref:</b>	SCI-PUB-14-0001-v01
			<b>Issue:</b>	6
			<b>Date:</b>	10/10/2017
			<b>Proj:</b>	SCIRoCCo Scatterometer Instrument Competence Centre

∞ ∞

$$= \int_{-\infty}^{\infty} tt \cdot pp(tt) sstt - \int_{-\infty}^{\infty} yy \cdot pp(yy) ssyy + (bbssaass) = (tt) - (yy) + (bbssaass) \quad (B12)$$

That is, the determination of the mean averaged quantity <bias> is encumbered by the difference between the mean value <y> of the collocating variable and the mean true value <t>.

$$\int_{-\infty}^{\infty} yy \cdot pp(yy) ssyy = (yy)$$

$$\int_{-\infty}^{\infty} tt \cdot pp(tt) sstt = (tt)$$

Care must be taken not to confound the distribution of the collocating system variable p(y) (which is available) with the actual true variable distribution p(t) (which is generally not available). Note that if the collocating system is assumed unbiased, then p(y) will differ from p(t) only by virtue of the collocating noise content:

$$pp(yy) = \int_{-\infty}^{\infty} pp(yy|tt) \cdot pp(tt) sstt$$

The presence of random wind vector component errors p(y|t) in the NWP reference (i.e. collocating) system makes the collocating wind speed distribution p(y) different from the true wind speed distribution p(t). Actually, random wind vector component errors of about 1.5 m/s in the NWP reference system will act to increase the apparent global mean wind speed by about 0.1 m/s. Therefore, random errors in the NWP model reference not only prevent us from looking into any potential wind-speed dependent biases that would be generated as a result of detector non-linearities or GMF errors (by introducing apparent error terms known as pseudobiases), but also contribute to uncertainty in the reference (i.e. collocating) wind speed distribution.

## 5.11 Applications

Not surprisingly, scatterometer applications involve both the atmosphere and the ocean. Requirements for meteorological applications are found in the domain of the World Meteorological Organisation, WMO. More in particular, space capabilities and requirements are well documented for several meteorological application areas in the on-line Observing Systems Capability Analysis and Review Tool (OSCAR) data base ([www.wmo-sat.info/oscar/spacecapabilities](http://www.wmo-sat.info/oscar/spacecapabilities)). The primary operational benefits of satellite Ocean Surface Vector Winds (OSVW) observations are the improvements of weather forecasting and warnings. In addition, knowledge of the winds and waves over the ocean is also essential for the maritime transportation, fishing, and oil production industries, as well as for search and rescue efforts, and the accurate tracking and management of marine hazards such as oil spills. Wind, wave and surge information are essential for marine safety in NRT ([www.osi-saf.org/](http://www.osi-saf.org/), [www.mywave.eu/en/](http://www.mywave.eu/en/), [www.storm-surge.info/](http://www.storm-surge.info/)).

Scatterometer winds are used in Numerical Weather Prediction (NWP) following the development of so-called observation operators for the ambiguous scatterometer winds (Stoffelen and Anderson, 1998; Portabella and Stoffelen, 2004) and training is available to provide insight in the main relevant characteristics of the scatterometer data and guidance for NWP applications ([nwpsaf.eu/deliverables/scatterometer/data\\_assimilation\\_workshop/](http://nwpsaf.eu/deliverables/scatterometer/data_assimilation_workshop/)).

	<h2 style="text-align: center;">The SCIRoCCo Scatterometry Handbook</h2>	<b>Ref:</b>	SCI-PUB-14-0001-v01
		<b>Issue:</b>	6
		<b>Date:</b>	10/10/2017
		<b>Proj:</b>	SCIRoCCo Scatterometer Instrument Competence Centre

Wind data assimilation more in general is the topic of the International Winds Working Group (IWWG) of the WMO Coordination Group of Meteorological Satellites (CGMS) ([groups.ssec.wisc.edu/groups/iwwg/activities/high-resolution-winds-1/nwp-data-assimilation](http://groups.ssec.wisc.edu/groups/iwwg/activities/high-resolution-winds-1/nwp-data-assimilation)).

In oceanography, scatterometer winds are also essential for determining the ocean forcing, wind induced mixing, currents (Lagerloef et al., 2003), and air/sea CO<sub>2</sub> fluxes. OSVW are used to estimate momentum transfer (surface stress) between the atmosphere and ocean, and are critically important for determining the large-scale ocean circulation and transport (Bourassa et al., 2009). Vector winds are needed to estimate the ageostrophic (Ekman) component of ocean currents, and consequently are linked to atmospheric and oceanographic upwelling and downwelling, coastal upwelling, primary productivity, cross shelf transport, ice transport, mixed layer evolution, and deep-water formation. Accurate wind speeds are also essential for reliable computations of air/sea heat fluxes (e.g. sensible and latent heat fluxes) as well as mass fluxes (e.g. CO<sub>2</sub> and H<sub>2</sub>O), making surface winds critically important for budgeting energy, moisture and carbon, and for studies of ocean acidification.

Core marine services are provided within the EU Copernicus programme; both off-line reprocessed winds as well as NRT products ([www.myocean.eu/](http://www.myocean.eu/)). Also, higher processing levels are provided for oceanography, such as on a geographical grid and/or combinations of multiple satellites.

The advection and offshore transport of nutrients and fresh water can be linked to the life cycle and annual variability in fish stocks. Both scalar and vector winds can be linked to upper-ocean mixing, which is easily linked to ocean, atmospheric, cryospheric and terrestrial climate change. For shorter time scale applications, surface wind vectors are also used for forecasts of storm surge and waves. Ocean surface winds change rapidly in both time and space. Satellite-based sampling density and relatively good accuracy make satellite winds desirable data (particularly for regions with sparse in situ observations) for many related applications such as coastal upwelling, oceanic/atmospheric coupling associated with both tropical instability wave and ocean fronts (Chelton et al., 2004), ocean currents (Lagerloef et al., 2003), detection of tropical disturbances (Gierach et al., 2007), wave forecasting, weather forecasting (Isaksen and Stoffelen, 2000), and storm surge (Morey et al., 2006), to list a small sample of applications. Portions of the surface winds observing systems are also used to provide observations of sea ice extent and rainfall (fresh water flux).

Several reviews of space-based wind measurements and applications have been published [e.g. (Liu, 2002) and (Liu and Xie, 2006)]. The current ocean wind observing system can be further improved by means of better bias removal and calibration, increased temporal sampling (via a constellation), finer spatial resolution (e.g. on the ocean eddy scale and intercalibration of near-coastal winds), and improved methods of blending observations (scalar winds and vector winds) from multiple scatterometers.

Long series of scatterometer data exist and satellite wind atlases ([www.norsewind.eu](http://www.norsewind.eu)) and climatologies are made. To provide for example representative monthly mean winds, the particular temporal and sampling of  $U_{10.5}$  by the

 <b>scirocco</b> scatterometer instrument competence centre	<h1>The SCIRoCCo Scatterometry Handbook</h1>	<b>Ref:</b>	SCI-PUB-14-0001-v01
		<b>Issue:</b>	6
		<b>Date:</b>	10/10/2017
		<b>Proj:</b>	SCIRoCCo Scatterometer Instrument Competence Centre

scatterometer in a month needs to be considered. Within the MyOcean project this is achieved by collocation of every scatterometer WVC with ECMWF winds, such that monthly differences between a particular scatterometer and the ECMWF NWP  $\mathbf{U}_{105}$  winds may be computed. Moreover, the difference between uniformly averaged ECMWF winds and scatterometer-sampled average ECMWF winds may be computed to obtain an estimate of the scatterometer sampling error on  $\mathbf{U}_{105}$ .

	<p>The SCIRoCCo Scatterometry Handbook</p>	Ref:	SCI-PUB-14-0001-v01
		Issue:	6
		Date:	10/10/2017
		Proj:	SCIRoCCo Scatterometer Instrument Competence Centre

## 6 The future

### 6.1 C-band Fan-Beam Scatterometer Heritage

ESCAT was followed by ASCAT, a clear heritage instrument, building on the success of the ESCAT instrument and ground processing. The Eumetsat Polar System programme lists the Second Generation ASCAT, called CSCAT, as a high-priority instrument. Specific requirements include slightly increased spatial resolution, extended swath, radiometric stability with reference to ASCAT, and the addition of horizontal polarisation. The C-band was chosen because it provides good sensitivity, all-weather capability and continuity of the ESCAT and ASCAT series. Rotating-pencil-beam concepts were discarded due to poorer simulated performance, while rotating-fan-beam concepts were considered to be technically too complex, since CSCAT would share a satellite platform with several other Earth-viewing microwave instruments (Lin et al., 2012).

The addition of new polarisation capabilities could potentially result in an improved capability to sense hurricane winds, since the vertical emit and receive polarisation of ESCAT and ASCAT saturates at around  $40 \text{ m s}^{-1}$  (Esteban et al., 2006). Since Eumetsat, together with many international sister agencies, is involved in building a global constellation of ocean vector wind missions (CEOS Ocean Surface Vector Wind Virtual Constellation), and obtaining extreme winds is a prerequisite for these sister agencies, the requirement for measuring extreme winds becomes more important. Horizontal polarisation in addition to vertical polarisation, however, requires an extended-capability antenna, which may be best accommodated on the mid-beams that are fixed on the body of the satellite platform. When emitting and receiving horizontal polarisation (HH) with the mid-beam, the additional sensitivity to hurricane winds would be limited as the geophysical dependency of HH is only favourable for extreme winds at incidence angles above  $35^\circ$ . Therefore, CSCAT incidence angles from  $20^\circ$  to  $35^\circ$  would not profit much from the extended HH capability. Another, more convenient, option would be to use the vertically emitted pulses and use the dual-polarisation mid-beam antennas to receive both the vertical (VV) and horizontal polarisations (VH).

Recently, van Zadelhoff et al. (2014) and Hwang et al. (2014) reported on the Radarsat SAR, which has cross-polarisation or VH capability, a linear dependency of VH backscatter on wind speed. No significant dependency on azimuth angle was found and a very modest incidence angle dependency. Preliminary verification of the Radarsat SAR VH backscatter dependency in tropical hurricanes confirmed a linear dependency at extreme winds as well. NOAA's aircraft campaigns and Eumetsat's NWP SAF performance assessments are planned to verify the VH geophysical dependency at extreme winds. Cross-polarisation capability would furthermore improve vegetation determination and, as a consequence, soil moisture index retrieval. Advantages for sea ice detection are also anticipated.

	<p>The SCIRoCCo Scatterometry Handbook</p>	Ref:	SCI-PUB-14-0001-v01
		Issue:	6
		Date:	10/10/2017
		Proj:	SCIRoCCo Scatterometer Instrument Competence Centre

Following the successful ERS mission at the C-band and successful NASA missions at the Ku-band, several agencies plan to develop scatterometer systems combining both wavelengths. In this way, resolution enhancements may be combined with the C-band all-weather capability.

## 6.2 Other Wind Resources

Besides using scatterometers, components of the wind field can be measured with SAR (e.g. Portabella et al., 2002) or passive radar measurements (WindSat, 2011; SSMIS, 2011). As a scatterometer, a SAR also measures the radar backscatter but at higher resolution (down to  $\sim 100$  m) and in only one azimuth direction. The GMF derived for ESCAT is often used for C-band SAR wind retrieval. The latter is a problem since it is not possible to resolve both wind direction and speed at a matching spatial resolution without prior information, while the sensitivities to wind speed and direction (in  $\text{m s}^{-1}$  per dB) are comparable (underdetermined problem). For passive radar measurements a similar underdetermination applies, but here the wind direction sensitivity of the measurements is so small that wind speed can be retrieved with sufficient accuracy.

## 6.3 Doppler Scatterometer

Scatterometer winds are measured relative to the ocean, whereas buoy and NWP model winds are provided with reference to a fixed Earth reference. Comparisons of these datasets therefore require that ocean currents are known. Direct current measurements would greatly improve ocean modelling, particularly in the tropics. ESA launched a project that assessed the potential of scatterometer instruments for sea surface current retrieval in addition to surface wind vector estimation. The project provided recommendations on signal processing techniques and GMF development for surface current retrieval from the Doppler estimates. Since the wind forces a net motion on the ocean waves, called the Stokes drift, the Doppler ocean motion measurements will also provide wind information, which may be combined with backscatter wind data to provide more complete information on air-sea interaction.

	<b>The SCIRoCCo Scatterometry Handbook</b>	<b>Ref:</b>	SCI-PUB-14-0001-v01
		<b>Issue:</b>	6
		<b>Date:</b>	10/10/2017
		<b>Proj:</b>	SCIRoCCo Scatterometer Instrument Competence Centre

## 7 References

- Attema, E.P.W. (1991). The Active Microwave Instrument on-board the ERS-1 satellite. *Proc. IEEE* **79**(6), 791–799. doi: 10.1109/5.90158
- Attema, E.P.W., Ulaby, F.T., (1978). Vegetation modeled as a water cloud. *Radio Science* **13**, 357–364. doi:10.1029/RS013i002p00357
- Bartalis, Z., Scipal, K., Wagner, W., (2006). Azimuthal anisotropy of scatterometer measurements over land. *IEEE Transactions on Geoscience and Remote Sensing* **44**, 2083–2092. doi:10.1109/TGRS.2006.872084
- Bartalis, Z., Wagner, W., Naeimi, V., Hasenauer, S., Scipal, K., Bonekamp, H., Figa, J. and Anderson, C. (2007). Initial soil moisture retrievals from the MetOp-A Advanced Scatterometer (ASCAT). *Geophys. Res. Lett* **34**, L20401.
- Bartalis, Z., (2009). Spaceborne Scatterometers for Change Detection over Land. Technische Universität Wien, Vienna.
- Belmonte Rivas, M., Stoffelen, A. (2011), New Bayesian algorithm for sea ice detection with QuikSCAT. *IEEE Trans. Geosci. Rem. Sens.* **49**(6), 1894–1901. doi:10.1109/TGRS.2010.2101608
- Belmonte Rivas, M., Verspeek, J., Verhoef, A., Stoffelen, A., (2012), Bayesian sea ice detection for the Advanced Scatterometer (ASCAT). *IEEE Trans. Geosci. Rem. Sens.* **50**(7), 2649–2657. doi: 10.1109/TGRS.2011.2182356.
- Blanke, B., Speich, S., Bentamy, A., Roy, C. & Sow, B. (2005). Modelling the structure and variability of the southern Benguela upwelling using QuikSCAT wind forcing. *J. Geophys. Res.* **110**, C07018. doi: 1029/2004JC002529.
- Bourassa, M.A., Stoffelen, A., Bonekamp, H., Chang, P., Chelton, D.B., Courtney, J., Edson, R. Figa, J. He, Y., Hersbach, H., Hilburn, K., Jelenak, Z., Kelly, K.A., Knabb, R., Lee, T., Lindstrom, E.J., Liu, W.T., Long, D.G., Perrie, W., Portabella, M., Powell, M., Rodriguez, E., Smith, D.K., Swail, V. & Wentz, F.J. (2009). Remotely sensed winds and wind stresses for marine forecasting and ocean modelling. *Proc. OceanObs '09: Sustained Ocean Observations and Information for Society*, Community White Paper. [www.oceanobs09.net/proceedings/cwp/Bourassa-OceanObs09.cwp.08.pdf](http://www.oceanobs09.net/proceedings/cwp/Bourassa-OceanObs09.cwp.08.pdf)
- Brocca, L., Moramarco, T., Melone, F., Wagner, W., (2013). A new method for rainfall estimation through soil moisture observations. *Geophysical Research Letters* n/a–n/a. doi:10.1002/grl.50173
- Brocca, L., Ciabatta, L., Massari, C., Moramarco, T., Hahn, S., Hasenauer, S., Kidd, R., Dorigo, W., Wagner, W., Levizzani, V., (2014). Soil as a natural rain gauge: Estimating global rainfall from satellite soil moisture data: Using the soil as a natural rain gauge. *Journal of Geophysical Research: Atmospheres* **119**, 5128–5141. doi:10.1002/2014JD021489
- Cavanié, A., Demurger, J. & Lecomte, P. (1986). Evaluation of the different parameters in Long's C-band model. *Proc. Workshop on ERS-1 Wind and Wave Calibration*, Schliersee, Germany. ESA SP-262, European Space Agency, Noordwijk, the Netherlands, pp.47-51.



	<b>The SCIRoCCo Scatterometry Handbook</b>	<b>Ref:</b>	SCI-PUB-14-0001-v01
		<b>Issue:</b>	6
		<b>Date:</b>	10/10/2017
		<b>Proj:</b>	SCIRoCCo Scatterometer Instrument Competence Centre

- Ceballos, A., Scipal, K., Wagner, W., Martínez-Fernández, J., (2005). Validation of ERS scatterometer-derived soil moisture data in the central part of the Duero Basin, Spain. *Hydrological Processes* 19, 1549–1566.  
doi:10.1002/hyp.5585
- Center for Ocean-Atmosphere Prediction Studies (COAPS). COAPS Scatterometry. 2004.  
<http://www.coaps.fsu.edu/scatterometry/>.  
Accessed December 2004.
- CERSAT (2011). *Monitoring Sea Ice Using Scatterometers of the ERS Satellites*. Centre ERS d'Archivage et de Traitement, IFREMER, France. <http://cersat.ifremer.fr/Science-Applications/Sea-ice/Sea-Ice-by-ERS>
- Champion, I., Faivre, R., (1997). Sensitivity of the radar signal to soil moisture: variation with incidence angle, frequency, and polarization. *IEEE Transactions on Geoscience and Remote Sensing* 35, 781–783.  
doi:10.1109/36.582001
- Chelton, D.B., Schlax, M.G. Freilich, M.H. & Milliff, R.E. (2004). Satellite measurements reveal persistent small-scale features in ocean winds. *Science* **303**, 978–983.
- Crow, W.T., Huffman, G.J., Bindlish, R., Jackson, T.J., (2009). Improving Satellite-Based Rainfall Accumulation Estimates Using Spaceborne Surface Soil Moisture Retrievals. *Journal of Hydrometeorology* 10, 199–212.  
doi:10.1175/2008JHM986.1
- De Haan, S. & Stoffelen, A. (2001). *Ice Discrimination using ERS Scatterometer*. Document external project: 2001, SAF/OSI/KNMI/TEC/TN/120, Eumetsat. [www.knmi.nl/publications/fulltexts/safosi\\_w\\_icescrknmi.pdf](http://www.knmi.nl/publications/fulltexts/safosi_w_icescrknmi.pdf)
- de Vries, J, Stoffelen, A and Beysens, (2005). J, Ambiguity Removal and Product Monitoring for SeaWinds, NWP SAF report NWPSAF\_KN\_TR\_001.
- De Wit, A. & Van Diepen, C. (2007). Crop model data assimilation with the ensemble Kalman filter for improving regional crop yield forecasts. *Agric. Forest Meteorol.* **146**(1–2), 38–56.
- Dobson, M., Ulaby, F., Hallikainen, M., El-rayes, M., (1985). Microwave Dielectric Behavior of Wet Soil-Part II: Dielectric Mixing Models. *IEEE Transactions on Geoscience and Remote Sensing* GE-23, 35–46.  
doi:10.1109/TGRS.1985.289498
- Dorigo, W.A., Scipal, K., Parinussa, R.M., Liu, Y.Y., Wagner, W., de Jeu, R.A.M., Naeimi, V., (2010). Error characterisation of global active and passive microwave soil moisture datasets. *Hydrology and Earth System Sciences* 14, 2605–2616. doi:10.5194/hess-14-2605-2010
- Drinkwater, M.R., and C.C. Lin. (2000). Introduction to the special section on emerging scatterometer applications. *IEEE Transactions on Geoscience and Remote Sensing* 38(4): 1763-1764.
- Dirmeyer, P.A., Guo, Z.C. & Gao, X. (2004). Comparison, validation, and transferability of eight multiyear global soil wetness products. *J. Hydrometeorol.* **5**(6), 1011–1033.
- Donelan, M. A., and W. J. Pierson, (1987). Radar scattering and equilibrium ranges in wind generated waves with application to scatterometry, *J. Geophys. Res.*, 92, 4971-5029.

	<h2 style="text-align: center;">The SCIRoCCo Scatterometry Handbook</h2>	<b>Ref:</b>	SCI-PUB-14-0001-v01
		<b>Issue:</b>	6
		<b>Date:</b>	10/10/2017
		<b>Proj:</b>	SCIRoCCo Scatterometer Instrument Competence Centre

Donnelly, William J., James R. Carswell, and Robert E. McIntosh, (1999). Revised ocean backscatter at C and Ku band under high wind conditions, *J. Geophys. Res.*, 104, 11,485-11,497.

Dorigo, W.A., Scipal, K., Parinussa, R.M., Liu, Y.Y., Wagner, W., de Jeu, R.A.M. & Naeimi, V. (2010). Error characterisation of global active and passive microwave soil moisture datasets. *Hydrol. Earth Syst. Sci.* **14**(12), 2605–2616.

Drinkwater, M.R., Long, D.G. & Bingham, A.W. (2001). Greenland snow accumulation estimates from satellite radar scatterometer data. *J. Geophys. Res. D: Atmospheres* **106**(D24), 33 935–33 950.

Drusch, M., Wood, E., Gao, H. & Thiele, A. (2004). Soil moisture retrieval during the Southern Great Plains Hydrologic Experiment 1999: A comparison between experimental remote sensing data and operational products. *Water Resources Res.* **40**(W02504). doi:10.1029/2003WR002441.

El-rayes, M., Ulaby, F., (1987). Microwave Dielectric Spectrum of Vegetation-Part I: Experimental Observations. *IEEE Transactions on Geoscience and Remote Sensing* GE-25, 541–549. doi:10.1109/TGRS.1987.289832

Entekhabi, D., Njoku, E.G., Houser, P., Spencer, M., Doiron, T., Yunjin, K., Smith, J., Girard, R., Belair, S., Crow, W., Jackson, T.J., Kerr, Y.H., Kimball, J.S., Koster, R., McDonald, K.C., O'Neill, P.E., Pultz, T., Running, S.W., Jiancheng, S., Wood, E. & van Zyl, J. (2004). The Hydrosphere State (Hydros) satellite mission: An Earth system pathfinder for global mapping of soil moisture and land freeze/thaw. *IEEE Trans. Geosci. Rem. Sens.* **42**(10), 2184–2195.

ESA (1998). *Proc. Emerging Scatterometer Applications Workshop*, ESTEC. ESA SP-424, European Space Agency, Noordwijk, the Netherlands.

ESA (1999). *Atmospheric Dynamics Mission: Core Earth Explorer Mission Selection Report*. ESA SP-1233(4), European Space Agency, Noordwijk, the Netherlands.

Eumetsat OSI SAF (1999). [www.knmi.nl/scatterometer/ers\\_prod/](http://www.knmi.nl/scatterometer/ers_prod/)

European Space Agency. "Scatterometer design." Earthnet Online (2004). <http://earth.esa.int/ers/instruments/>. Accessed December 2004.

Figa-Saldaña, J., J.J.W. Wilson, E. Attema, R. Gelsthorpe, M.R. Drinkwater, and A. Stoffelen (2002). The advanced scatterometer (ASCAT) on the meteorological operational (MetOp) platform: A follow on for European wind scatterometers. *Canadian Journal of Remote Sensing* 28(3): 404-412.

Figa, J. & Stoffelen, A. (2000). On the assimilation of Ku-band scatterometer winds for weather analysis and forecasting. *IEEE Trans. Geosci. Rem. Sens.* **38**(4), 1893–1902.

Freilich, M.H., Qi, H., Dunbar, R.S., (1999). Scatterometer beam balancing using open-ocean backscatter measurements, *J. Atmos. Ocean. Technol.*, 16(2), 283-297.

Frison, P.L. & Mougin, E. (1996). Monitoring global vegetation dynamics with ERS-1 wind scatterometer data. *Int. J. Rem. Sens.* **17**(16), 3201–3218.

	<h2 style="text-align: center;">The SCIRoCCo Scatterometry Handbook</h2>	<b>Ref:</b>	SCI-PUB-14-0001-v01
		<b>Issue:</b>	6
		<b>Date:</b>	10/10/2017
		<b>Proj:</b>	SCIRoCCo Scatterometer Instrument Competence Centre

- Gierach, M.M., Bourassa, M.A., Cunningham, P., O'Brien, J.J., Reasor, P.D., (2007), Vorticity based detection of tropical cyclogenesis, *J., Appl. Meteor. Climatol.*, 46, 1214-1229, doi:10.1175/JAM2522.1.
- Hallikainen, M., Ulaby, F., Dobson, M., El-rayes, M., Wu, L., (1985). Microwave Dielectric Behavior of Wet Soil-Part 1: Empirical Models and Experimental Observations. *IEEE Transactions on Geoscience and Remote Sensing GE-23*, 25–34. doi:10.1109/TGRS.1985.289497
- Henderson, F.M., and A.J. Lewis, eds. 1998. *Principles & applications of imaging radar*. Manual of Remote Sensing Third Edition, Volume 2. New York: John Wiley & Sons, Inc.
- Hersbach, H. (2008). The usage of scatterometer data at ECMWF. *OVWST meeting*, Seattle.  
<http://coaps.fsu.edu/scatterometry/meeting/docs/2008/othersci/hersbach.pdf>
- Hersbach, H., Stoffelen, A. & de Haan, S. (2007). An improved C-band scatterometer ocean geophysical model function: CMOD5. *J. Geophys. Res.* **112**. doi:10.1029/2006JC003743.
- Hillel, D., (2014). Introduction to environmental soil physics. Elsevier Academic Press, Amsterdam ; Boston.
- Hollmann, R., C.J. Merchant, R. Saunders, C. Downy, M. Buchwitz, A. Cazenave, E. Chuvieco, P. Defourny, G. de Leeuw, R. Forsberg, T. Holzer-Popp, F. Paul, S. Sandven, S. Sathyendranath, M. van Roozendaal, W. Wagner (2013), The ESA Climate Change Initiative: satellite data records for essential climate variables, *Bulletin of the American Meteorological Society*, doi: <http://dx.doi.org/10.1175/BAMS-D-11-00254.1>
- Isaksen, L. & Stoffelen, A. (2000). ERS scatterometer wind data impact on ECMWF's tropical cyclone forecasts. *IEEE Trans. Geosci. Rem Sens.* **38**, 1885–1892.
- Isaksen, L. & Janssen, P.A.E.M. (2004). Impact of ERS scatterometer winds in ECMWF's assimilation system. *Q. J. R. Meteorol. Soc.* **130**(600), 1793–1814, Part A. DOI: 10.1256/qj.03.110.
- Kennett, R.G. & Li, F.K. (1989). Seasat over-land scatterometer data, I: Global overview of the Ku-band backscatter coefficients. *IEEE Trans. Geosci. Rem. Sens.* **27**(5), 592–605.
- Kerr, Y.H. (2007). Soil moisture from space: Where are we? *Hydrogeol. J.* **15**(1), 117–120.
- Künzer, C., Zhao, D., Scipal, K., Sabel, D., Naeimi, V., Bartalis, Z., Hasenauer, S., Mehl, H., Dech, S. & Wagner, W. (2009). El Niño Southern Oscillation influences represented in ERS scatterometer-derived soil moisture data. *Appl. Geog.* **29**, 463–477.
- Lagerloef, G., Lukas, R., Bonjean, F., Gunn, J., Mitchum, G., Bourassa, M., Busalacchi, T., (2003), El Niño tropical Pacific Ocean surface current and temperature evolution in 2002 and outlook for early 2003, *Geophys. Res. Lett.*, 30, 1514, doi:10.1029/2003GL017096.
- Le Meur, D., Isaksen, L. Hansen, B., Saunders, R. & Janssen, P. (1998). *Global Validation of ERS Wind and Wave Products*. Final report to the European Space Agency, ESA contract No. 8488/95/NL/CN, ECMWF, Shinfield Park, Reading, Berkshire, UK.

	<h2 style="text-align: center;">The SCIRoCCo Scatterometry Handbook</h2>	<b>Ref:</b>	SCI-PUB-14-0001-v01
		<b>Issue:</b>	6
		<b>Date:</b>	10/10/2017
		<b>Proj:</b>	SCIRoCCo Scatterometer Instrument Competence Centre

- Lin, C.C., M. Betto, M. Belmonte-Rivas, A. Stoffelen en J. de Kloe (2012), EPS-SG Winds scatterometer Concept Tradeoffs and Wind Retrieval Performance Assessment *IEEE Transactions on Geoscience and Remote Sensing*, 50, 7, 2458-2472, doi:10.1109/TGRS.2011.2180393.
- Liu, W.T., (2002), Progress in scatterometer application, *J. Oceanogr.*, 58, 121-136.
- Liu, W.T. & Xie, X. (2006). Measuring ocean surface wind from space. In J. Gower (Ed), *Remote Sensing of the Marine Environment, Manual of remote Sensing*. 3rd edn, vol. 6, American Society for Photogrammetry and Remote Sensing, pp.149–178.
- Liu, Y.Y., Parinussa, R.M., Dorigo, W.A., De Jeu, R.A.M., Wagner, W., van Dijk, A.I.J.M., McCabe, M.F., Evans, J.P., (2011). Developing an improved soil moisture dataset by blending passive and active microwave satellite-based retrievals. *Hydrology and Earth System Sciences* 15, 425–436. doi:10.5194/hess-15-425-2011
- Liu, Y.Y., Dorigo, W.A., Parinussa, R.M., de Jeu, R.A.M., Wagner, W., McCabe, M.F., Evans, J.P., van Dijk, A.I.J.M., (2012). Trend-preserving blending of passive and active microwave soil moisture retrievals. *Remote Sensing of Environment* 123, 280–297. doi:10.1016/j.rse.2012.03.014
- Long, D.G., and M.R. Drinkwater. (1999). Cryosphere applications of NSCAT data. *IEEE Transactions on Geoscience and Remote Sensing* 37(3): 1671-1684.
- Long, D.G., M.R. Drinkwater, B. Holt, S. Saatchi, and C. Bertoia. (2001). Global ice and land climate studies using scatterometer image data. *EOS, Transaction of the American Geophysical Union* 82(43): 503. Also available online at [http://www.agu.org/eos\\_elec/010126e.html](http://www.agu.org/eos_elec/010126e.html). Paper and electronic versions are available in a [PDF file \(4 MB\)](#).
- Long, D.G., and M.R. Drinkwater. (2000). Azimuth variation in microwave scatterometer and radiometer data over Antarctica. *IEEE Transactions on Geoscience and Remote Sensing* 38(4): 1857-1870.
- Long, D.G., P. Hardin, and P. Whiting. (1993). Resolution enhancement of spaceborne scatterometer data. *IEEE Transactions on Geoscience and Remote Sensing* 31(3): 700-715.
- Long, A.E. (1986). Towards a C-band radar echo model for the ERS-1 scatterometer. *3rd Int. Coll. Spectral Signatures in Remote Sensing*, Les Arc, France. ESA SP-247, European Space Agency, Noordwijk, the Netherlands, pp.29–34.
- Magagi, R.D., Kerr, Y.H., (1997). Retrieval of soil moisture and vegetation characteristics by use of ERS-1 wind scatterometer over arid and semi-arid areas. *Journal of Hydrology* 188-189, 361–384. doi:10.1016/S0022-1694(96)03166-6
- Miralles, D.G., Crow, W.T., Cosh, M.H., 2010. Estimating Spatial Sampling Errors in Coarse-Scale Soil Moisture Estimates Derived from Point-Scale Observations. *Journal of Hydrometeorology* 11, 1423–1429. doi:10.1175/2010JHM1285.1
- Moore, G.W. & Renfrew, I.A. (2005). Tip jets and barrier winds: a QuikSCAT climatology of high wind speed events around Greenland, *J. Climate* 18, 3713–3725.
- Moore, R.J. & Pierson, W.J. (1967). Microwave determination of winds at sea. *Proc. IEEE* 67, 1504–1521.
- Morey, S.L., Baig, S.R., Bourassa, M.A., Dukhovskoy, D.S., O'Brien, J.J., (2006), Remote forcing contribution to storm induced sea level rise during Hurricane Denis, *Geophys. Res. Lett.*, 33, L19603, doi: 10.1029/2006GL027021.

	<h2 style="text-align: center;">The SCIRoCCo Scatterometry Handbook</h2>	<b>Ref:</b>	SCI-PUB-14-0001-v01
		<b>Issue:</b>	6
		<b>Date:</b>	10/10/2017
		<b>Proj:</b>	SCIRoCCo Scatterometer Instrument Competence Centre

- Mougin, E., Lopes, A., Frison, P.L. & Proisy, C. (1995). Preliminary analysis of ERS-1 wind scatterometer data over land surfaces. *Int. J. Rem. Sens.* **16**(2), 391–398.
- NASA Jet Propulsion Laboratory. "Missions - NSCAT." Winds: measuring ocean winds from space. 2004. <http://winds.jpl.nasa.gov/missions/nscat/index.cfm>. Accessed December 2004.
- NASA Jet Propulsion Laboratory. "Missions - SeaWinds on QuikSCAT." Winds: measuring ocean winds from space. 2004. <http://winds.jpl.nasa.gov/missions/quikscat/index.cfm>. Accessed December 2004.
- NASA Jet Propulsion Laboratory. "Missions - SeaWinds on ADEOS II." Winds: measuring ocean winds from space. 2004. <http://winds.jpl.nasa.gov/missions/seawinds/index.cfm>. Accessed December 2004.
- Naderi, F., M.H. Freilich, and D.G. Long. (1991). Spaceborne radar measurement of wind velocity over the ocean -- an overview of the NSCAT scatterometer system. *Proceedings of the IEEE* 79(6): 850-866. Invited paper.
- Naeimi, V., Scipal, K., Bartalis, Z., Hasenauer, S., Wagner, W., 2009. An Improved Soil Moisture Retrieval Algorithm for ERS and METOP Scatterometer Observations. *IEEE Transactions on Geoscience and Remote Sensing* 47, 1999–2013. doi:10.1109/TGRS.2008.2011617
- Neyt, X., Manise, N., Achery, N. (2005), Enhanced neural-network based sea-ice discrimination using ERS scatterometer data, *Proc. SPIE*, 5977, Remote Sensing of the Ocean, Sea Ice, and Large Water Regions.
- Niederreiter, H., 1992. Random number generation and quasi-Monte Carlo methods, CBMS-NSF regional conference series in applied mathematics. Society for Industrial and Applied Mathematics, Philadelphia, Pa.
- Offiler, D. (1987). *ERS-1 Wind Retrieval Algorithms*. UK Met Office, MET O 19, Branch Memorandum, No. 86.
- Parajka, J., Naeimi, V., Blöschl, G., Wagner, W., Merz, R. & Scipal, K. (2006). Assimilating scatterometer soil moisture data into conceptual hydrologic models at the regional scale. *Hydrol. Earth Syst. Sci.* **10**, 353–368.
- Pellarin, T., Calvet, J.-C. & Wagner, W. (2006). Evaluation of ERS scatterometer soil moisture products over a half-degree region in southwestern France. *Geophys. Res. Lett.* **33**(17), L17401.
- Pellarin, T., Ali, A., Chopin, F., Jobard, I., Bergès, J.-C., (2008). Using spaceborne surface soil moisture to constrain satellite precipitation estimates over West Africa. *Geophysical Research Letters* 35. doi:10.1029/2007GL032243
- Peteherych, S., Wurtele, M.G., Woiceshyn, P.M., Boggs, D.H. & Atlas, R. (1984). First global analysis of SEASAT scatterometer winds and potential for meteorological research. *NASA Conf. Publ. CP2303*, pp.575–585.
- Pierson, W.J., (1989). Probabilities and statistics for backscatter estimates obtained by a scatterometer, *J. Geophys. Res.*, 94, 9743-9759, 1989; correction in *J. Geophys. Res.*, 95, 809, 1990.
- Portabella, M. (2002). *Wind Field Retrieval from Satellite Radar Systems*. Thesis, University of Barcelona, Spain. [www.knmi.nl/publications/fulltexts/phd\\_thesis.pdf](http://www.knmi.nl/publications/fulltexts/phd_thesis.pdf)
- Portabella, M. & Stoffelen, A. (2001). Rain detection and quality control of sea winds. *J. Atm. Ocean Techn.* **18**(7), 1171–1183.
- Portabella, M. & Stoffelen, A. (2002). A comparison of KNMI quality control and JPL rain flag for seawinds. *Can. J. Rem. Sens.* **28**(3), 424–430.

	<b>The SCIRoCCo</b> <b>Scatterometry Handbook</b>	<b>Ref:</b>	SCI-PUB-14-0001-v01
		<b>Issue:</b>	6
		<b>Date:</b>	10/10/2017
		<b>Proj:</b>	SCIRoCCo Scatterometer Instrument Competence Centre

- Portabella, M., A. Stoffelen, (2002). Quality Control and Wind Retrieval for SeaWinds, EUMETSAT fellowship report.
- Portabella, M. & Stoffelen, A. (2006). Scatterometer backscatter uncertainty due to wind variability. *IEEE Trans. Geosci. Rem. Sens.* **44**(11), 3356–3362. doi:10.1109/TGRS.2006.877952
- Portabella, M. and Stoffelen, A., (2007). Development of a Global Scatterometer Validation and Monitoring, Visiting Scientist report for the Ocean & Sea Ice SAF, SAF/OSI/CDOP/KNMI/SCI/RP/141.
- Portabella, M., Stoffelen, A. & Johannessen, J.A (2002). Toward an optimal inversion method for SAR wind retrieval. *J. Geophys. Res.* **107**(C8), 1–13.
- Portabella, M., Stoffelen, A., Verhoef, A. & Lin, W. (2011). Rain effects on ASCAT retrieved winds: towards an improved quality control, *IEEE Trans. Geosci. Rem. Sens.* **50**(7), 2495–2506.
- Pullianen, J.T., Manninen, T., Hallikainen, M.T., (1998). Application of ERS-1 wind scatterometer data to soil frost and soil moisture monitoring in boreal forest zone. *IEEE Transactions on Geoscience and Remote Sensing* **36**, 849–863. doi:10.1109/36.673678
- Sandu, I., Beljaars, A., Bechtold, P., Mauritsen, T. and Balsamo, P., “Why is it so difficult to represent stably stratified conditions in numerical weather prediction (NWP) models?”, *Journal of Advances in Modeling Earth Systems* **5** (2), pages 117–133, June 2013, DOI: 10.1002/jame.20013.
- Schmugge, T.J., (1983). Remote Sensing of Soil Moisture: Recent Advances. *IEEE Transactions on Geoscience and Remote Sensing* **GE-21**, 336–344. doi:10.1109/TGRS.1983.350563
- Schmullius, C.C. (1997). Monitoring Siberian forests and agriculture with the ERS-1 wind scatterometer. *IEEE Trans. Geosci. Rem. Sens.* **35**(5), 1363–1366.
- Scipal, K., (2002). Global soil moisture retrieval from ERS scatterometer data. Vienna University of Technology.
- Scipal, K., Wagner, W., Trommler, M., Naumann, K., (2002). The global soil moisture archive 1992-2000 from ERS scatterometer data: first results. *IEEE*, pp. 1399–1401. doi:10.1109/IGARSS.2002.1026129
- Scipal, K., Scheffler, C. & Wagner, W. (2005). Soil moisture–runoff relation at the catchment scale as observed with coarse resolution microwave remote sensing. *Hydrol. Earth Syst. Sci.* **9**(3), 173–183.
- Scipal, K., Drusch, M., Hasenauer, S., Wagner, W. & Jann, A. (2007). Towards the assimilation of scatterometer derived soil moisture in the ECMWF numerical weather prediction system. *Joint 2007 Eumetsat Meteorological Satellite Conf. and 15th Satellite Meteorology & Oceanography Conf. of the American Meteorological Society*, Amsterdam, the Netherlands.
- Scipal, K., Holmes, T., de Jeu, R., Naeimi, V., Wagner, W., (2008). Error Estimation of Soil Moisture Derived from Active and Passive Microwave Satellite Observations and Model Data. *IEEE*, pp. II–761–II–764. doi:10.1109/IGARSS.2008.4779105
- Stephen, H., Long, D.G., 2005. Microwave backscatter modeling of erg surfaces in the Sahara desert. *IEEE Transactions on Geoscience and Remote Sensing* **43**, 238–247. doi:10.1109/TGRS.2004.840646

	<h2 style="text-align: center;">The SCIRoCCo Scatterometry Handbook</h2>	<b>Ref:</b>	SCI-PUB-14-0001-v01
		<b>Issue:</b>	6
		<b>Date:</b>	10/10/2017
		<b>Proj:</b>	SCIRoCCo Scatterometer Instrument Competence Centre

Sienkiewicz, J., Brennan, M.J., Knabb, R., Chang, P.S., Cobb, H., Jelenak, Z.J., Ahmad, K.A., Soisuvarn, S., Kosier, D. & Bancroft, G. (2010). Impact of the loss of QuikSCAT on NOAA MWS marine warning and forecast operations. *1st Int. Ocean Vector Winds Science Team Meeting*, Barcelona, Spain.

Spencer, M.W., C. Wu, and D.G. Long. 2000. Improved resolution backscatter measurements with the SeaWinds pencil-beam scatterometer. *IEEE Transactions on Geoscience and Remote Sensing* 38(1): 89-104.

SSMIS (2011). [www.ncdc.noaa.gov/oa/rsad/ssmi/swath/index.html](http://www.ncdc.noaa.gov/oa/rsad/ssmi/swath/index.html)

Stoffelen, A. (1998). *Scatterometry*, PhD Thesis, Utrecht University, the Netherlands. <http://igitur-archive.library.uu.nl/dissertations/01840669/inhoud.htm>

Stoffelen, A., (1999). A simple method for calibration of a scatterometer over the ocean, *J. Atmos. Ocean. Technol.*, 16(2), 275-282.

Stoffelen, A. & Anderson, D. (1993). Wind retrieval and ERS-1 scatterometer radar backscatter measurements. *Adv. Space Res.* **13**(5), (5)53–(5)60.

Stoffelen, A. & Anderson, D. (1997a). Scatterometer data interpretation: measurement space and inversion. *J. Atm. Ocean Techn.* **14**(6), 1298–1313.

Stoffelen, A. & Anderson, D. (1997b). Ambiguity removal and assimilation of scatterometer data. *Q. J. R. Meteorol. Soc.* **123**, 491–518.

Stoffelen, A. & van Beukering, P. (1997). *Implementation of Improved ERS Scatterometer Data Processing and its Impact on HIRLAM Short Range Weather Forecasts*. HIRLAM Technical Report No. 31, KNMI, the Netherlands.

Stoffelen, A. & Cats, G. (1991). The impact of SeaSat-A scatterometer data on high-resolution analyses and forecasts: The development of the QEII storm. *Mon. Wea. Rev.* **119**, 2794–2802.

Stoffelen, A., & Portabella, M. (2006). On Bayesian scatterometer wind inversion, *IEEE Trans. Geosci. Rem. Sens.* **44**(6), 1523–1533. doi:10.1109/TGRS.2005.862502

Stoffelen, Ad, Siebren de Haan, Yves Quilfen, and Harald Schyberg, (2000). ERS Scatterometer Ambiguity Removal Comparison, OSI SAF report, 2000.

Stoffelen, A., A. Verhoef, J. Verspeek, J. Vogelzang, T. Driesenaar, Y. Risheng, C. Payan, G. De Chiara, J. Cotton, A. Bentamy, M. Portabella and G.J. Marseille (2013), Research and Development in Europe on Global Application of the OceanSat-2 Scatterometer Winds, Document extern project: 2013, NWP SAF report number: NWPSAF-KN-TR-022 OSI SAF re port number: SAF/OSI/CDOP2/KNMI/TEC/RP/196, KNMI, [http://www.knmi.nl/publications/fulltexts/oceansat\\_cal\\_val\\_report\\_final\\_copy1.pdf](http://www.knmi.nl/publications/fulltexts/oceansat_cal_val_report_final_copy1.pdf)

Tokmakian, R. (2005). An ocean model's response to scatterometer winds. *Ocean Modeling* **9**, 89–103.

	<h2 style="text-align: center;">The SCIRoCCo Scatterometry Handbook</h2>	<b>Ref:</b>	SCI-PUB-14-0001-v01
		<b>Issue:</b>	6
		<b>Date:</b>	10/10/2017
		<b>Proj:</b>	SCIRoCCo Scatterometer Instrument Competence Centre

- Ulaby, F., El-rayes, M., (1987). Microwave Dielectric Spectrum of Vegetation - Part II: Dual-Dispersion Model. *IEEE Transactions on Geoscience and Remote Sensing* GE-25, 550–557. doi:10.1109/TGRS.1987.289833
- Ulaby, F.T., Bativala, P.P., Dobson, M.C., (1978). Microwave Backscatter Dependence on Surface Roughness, Soil Moisture, and Soil Texture: Part I-Bare Soil. *Geoscience Electronics, IEEE Transactions on* 16, 286–295. doi:10.1109/TGE.1978.294586
- Ulaby, F.T., Dubois, P.C., van Zyl, J., (1996). Radar mapping of surface soil moisture. *Journal of Hydrology* 184, 57–84. doi:10.1016/0022-1694(95)02968-0
- Ulaby, F.T., Long, D.G., Blackwell, W.J., Elachi, C., Fung, A.K., Ruf, C., Sarabandi, K., Zebker, H.A., Van Zyl, J., (2014). *Microwave radar and radiometric remote sensing*. University of Michigan Press, Ann Arbor.
- Ulaby, F.T., Moore, R.K., Fung, A.K., (1982). *Microwave Remote Sensing - Active and Passive*. Artech House, Norwood, MA.
- Ulaby, F.T., Sarabandi, K., McDONALD, K., Whitt, M., Dobson, M.C., (1990). Michigan microwave canopy scattering model. *International Journal of Remote Sensing* 11, 1223–1253. doi:10.1080/01431169008955090
- Vachon, P. & Wolfe, J. (2011). C-band cross-polarization wind speed retrieval. *IEEE Trans. Geosci. Rem. Sens. Lett.* 8(3), 456–459. doi: 10.1109/LGRS.2010.2085417.
- Valenzuela, G. R. (1978). Theories for the interaction of electromagnetic and ocean waves - a review, *Bound. Layer Meteor.*, 13, 612-685.
- Verspeek, J., Verhoef, A., Stoffelen, A., (2011). ASCAT NWP Ocean Calibration, OSI SAF Technical Note, Version 1.5.
- Verspeek, J., Stoffelen, A. Verhoef, A. & Portabella, M. (2012). Improved ASCAT wind retrieval using NWP ocean calibration. *IEEE Trans. Geosci. Rem. Sens.* 50(7), 2488–2494.
- Verhoef, A., M. Portabella, A. Stoffelen and H. Hersbach, (2008). CMOD5.n - the CMOD5 GMF for neutral winds, OSI SAF report, SAF/OSI/CDOP/KNMI/TEC/TN/165.
- Vogelzang, J., Stoffelen, A., Verhoef, A. & Figa-Saldaña, J. (2011). On the quality of high-resolution scatterometer winds. *J. Geophys. Res.* 116, C10033. doi:10.1029/2010JC006640.
- Vogelzang, J. & Stoffelen, A. (2012). Scatterometer wind vector products for application in meteorology and oceanography. *J. Sea Res.*, special issue Physics of Sea and Ocean, 74, 16–25.
- Wagner, W., (1998). Soil moisture retrieval from ERS scatterometer data. European Commission, Joint Research Centre, Space Applications Institute.
- Wagner, W., Lemoine, G., Borgeaud, M., Rott, H., (1999a). A study of vegetation cover effects on ERS scatterometer data. *IEEE Transactions on Geoscience and Remote Sensing* 37, 938–948. doi:10.1109/36.752212
- Wagner, W., Lemoine, G., Rott, H., (1999). A Method for Estimating Soil Moisture from ERS Scatterometer and Soil Data. *Remote Sensing of Environment* 70, 191–207. doi:10.1016/S0034-4257(99)00036-X
- Wagner, W., Noll, J., Borgeaud, M., Rott, H., (1999b). Monitoring soil moisture over the Canadian Prairies with the ERS scatterometer. *IEEE Transactions on Geoscience and Remote Sensing* 37, 206–216. doi:10.1109/36.739155



	<h2 style="text-align: center;">The SCIRoCCo Scatterometry Handbook</h2>	<b>Ref:</b>	SCI-PUB-14-0001-v01
		<b>Issue:</b>	6
		<b>Date:</b>	10/10/2017
		<b>Proj:</b>	SCIRoCCo Scatterometer Instrument Competence Centre

Wagner, W., Bartalis, Z., Naeimi, V., Park, S.-E., Figa-Saldana, J. & Bonekamp, H. (2010). Status of the METOP ASCAT soil moisture product. *Proc. IEEE Geoscience and Remote Sensing Symp., IGARSS 2010*, Honolulu, USA, pp.276–279.

Wagner, W., Blöschl, G., Pampaloni, P., Calvet, J.-C., Bizzarri, B., Wigneron, J.-P. & Kerr, Y. (2007). Operational readiness of microwave remote sensing of soil moisture for hydrologic applications. *Nordic Hydrol.* **38**(1), 1–20.

Wagner, W., de Jeu, R. & van Oevelen, P. (2009). Towards multi-source global soil moisture datasets for unravelling climate change impacts on water resources. *Proc. 33rd Int. Symp. on Remote Sensing of Environment (ISRSE)*. Joint Research Centre of the European Commission, Stresa, Italy, p.3.

Wagner, W., Scipal, K., Pathe, C., Gerten, D., Lucht, W. & Rudolf, B. (2003). Evaluation of the agreement between the first global remotely sensed soil moisture data with model and precipitation data. *J. Geophys. Res. D: Atmospheres* **108**(D19), Art. No. 4611.

Wen, J. & Su, Z.B. (2003). A time series based method for estimating relative soil moisture with ERS wind scatterometer data. *Geophys. Res. Lett.* **30**(7), 1397.

WindSat (2011). [www.nrl.navy.mil/WindSat/](http://www.nrl.navy.mil/WindSat/)

Wismann, V. (2000). Monitoring of seasonal thawing in Siberia with ERS scatterometer data. *IEEE Trans. Geosci. Rem. Sens.* **38**(4 II), 1804–1809.

Woodhouse, I.H. & Hoekman, D.H. (2000). Determining land-surface parameters from the ERS wind scatterometer. *IEEE Trans. Geosci. Rem. Sens.* **38**(1), 126–140.

Zhao, D., Su, B. & Zhao, M. (2006). Soil moisture retrieval from satellite images and its application to heavy rainfall simulation in eastern China. *Adv. Atmos. Sci.* **23**(2), 299–316.


Zribi, M., André, C. & Decharme, B. (2008). A method for soil moisture estimation in Western Africa based on the ERS scatterometer. *IEEE Trans. Geosci. Rem. Sens.* **46**(2), 438–448.

	<b>The SCIRoCCo Scatterometry Handbook</b>	<b>Ref:</b>	SCI-PUB-14-0001-v01
		<b>Issue:</b>	6
		<b>Date:</b>	10/10/2017
		<b>Proj:</b>	SCIRoCCo Scatterometer Instrument Competence Centre

## Appendix A. The Scatterometry Glossary

The following Glossary defines the commonly agreed terminology to use in all the documents generated by the SCIRoCCo Consortium. Glossary is also available as a separate SCIRoCCo publication: SCI-SPU-14-0001

Term	Description
<b>Absolute calibration</b>	Process of determining the relationship between the raw instrument recordings and the physical quantity of interest.
<b>Absorptance</b>	A measure of the ability of a material to absorb EM energy at a specific wavelength.
<b>Active Microwave Instrument (AMI)</b>	Part of ERS-1 and ERS-2 payload, incorporating image (SAR), wind (scatterometer), and wave (imagette) modes.
<b>Active remote sensing</b>	Remote sensing methods that provide their own source of electromagnetic radiation to illuminate the Earth's surface.
<b>Active transponder</b>	Artificial point target with a well-established radar cross section used for absolute calibration of scatterometers
<b>Advanced Scatterometer (ASCAT)</b>	Space-borne scatterometer as part of the MetOp satellites payload operated by EUMETSAT
<b>Advanced Scatterometer Processing System (ASPS)</b>	Scatterometer processing framework specifically designed to process ERS-2 AMI-WS data in Zero Gyro Mode (ZGM)
<b>Along-track resolution</b>	On-ground spatial resolution of a microwave instrument in direction of the satellite orbit.
<b>Ambiguity removal (AR)</b>	Spatial filtering method to obtain a spatially consistent and unambiguous wind vector field over the scatterometer swath.
<b>Amplitude</b>	Measure of the strength of a signal, and in particular the strength of an electromagnetic wave
<b>Analysis</b>	The process of approximating the true state of a (geo)physical system at a given time
<b>Angular beam width</b>	Angle subtended in the horizontal plane by the radar beam.
<b>Angular field of view</b>	Angle subtended by lines from a remote sensing system to the outer margins of the strip of terrain that is viewed by the system.

	<b>The SCIRoCCo Scatterometry Handbook</b>	<b>Ref:</b>	SCI-PUB-14-0001-v01
		<b>Issue:</b>	6
		<b>Date:</b>	10/10/2017
		<b>Proj:</b>	SCIRoCCo Scatterometer Instrument Competence Centre

<b>Antenna</b>	Device that transmits and/or receives microwave energy in radar systems.
<b>Antenna aperture</b>	Measure of effectiveness of an antenna to transmit or receive power of an electromagnetic wave.
<b>Antenna gain pattern</b>	Directional (angular) dependence of the strength of transmitted or received microwave energy of an antenna.
<b>Azimuth angle</b>	Geographic orientation of a line given as an angle measured in degrees clockwise from north (sometimes from south).
<b>Azimuthal anisotropy</b>	Directional, with respect to the azimuth angle, dependent properties of a surface or medium, as opposed to isotropy (uniformity in all directions)
<b>Background field</b>	In objective analysis and data assimilation, an a priori estimate of the atmospheric state. In most data assimilation systems, the background field is a forecast from the previous analysis time. Sometimes the term “First Guess” is also used for the background field.
<b>Backscatter</b>	In microwave remote sensing, the portion of the microwave energy scattered directly back towards the antenna by the Earth's surface.
<b>Backscatter coefficient</b>	In microwave remote sensing, a quantitative measure of the intensity of energy scattered back to a radar antenna from an area on the Earth's surface.
<b>Backscatter noise</b>	Uncertainty measure of the backscatter measurement.
<b>Backscatter-triple</b>	A number of three independent backscatter coefficients, observing an identical region on the Earth's surface almost simultaneously in time, but at different measurement configurations (azimuth and incidence angles).
<b>Beam</b>	A focused pulse of electromagnetic energy.
<b>Bistatic radar equation</b>	Radar equation in case of physically separated transmitter and receiver antenna.
<b>Boresight direction</b>	Direction of the maximum power emitted, appearing as a single mainlobe in the antenna gain pattern.
<b>Calibration</b>	The process of quantitatively defining the instrument response to known, controlled input signals.
<b>Calibration target</b>	In microwave remote sensing, natural or artificial targets on the Earth's surface utilised for calibration purposes.
<b>C-band</b>	A microwave band with a wavelength (frequency) interval ranging from 7.5 - 3.8 cm (4 - 8 GHz) in the electromagnetic spectrum.

	<h1>The SCIRoCCo</h1> <h2>Scatterometry Handbook</h2>	<b>Ref:</b>	SCI-PUB-14-0001-v01
		<b>Issue:</b>	6
		<b>Date:</b>	10/10/2017
		<b>Proj:</b>	SCIRoCCo Scatterometer Instrument Competence Centre

<b>Change-detection algorithm</b>	An algorithm ascertaining the changes of specific features within a certain time interval.
<b>Coherent radiation</b>	Electromagnetic radiation whose waves are equal in direction, amplitude and phase, so that they are capable of exhibiting interference.
<b>Corner reflector</b>	Cavity formed by two or three smooth planar surfaces intersecting at right angles. Electromagnetic waves entering a corner reflector are reflected directly back toward the source.
<b>Cross-over angles</b>	In the TU Wien soil moisture retrieval algorithm, particular incidence angles at which the backscatter coefficient is unaffected by vegetation changes.
<b>Curvature</b>	In the TU Wien soil moisture retrieval algorithm, the second derivative of the backscatter coefficient as a function of the incidence angle. Used in a second order Taylor polynomial approximation to normalise the backscatter value to a reference incidence angle of 40 degrees.
<b>Data assimilation</b>	The purpose of data assimilation is to determine a best possible atmospheric state using observations and short range forecasts. Data assimilation is typically a sequential time-stepping procedure, in which a previous model forecast is compared with newly received observations, the model state is then updated to reflect the observations, a new forecast is initiated, and so on. The update step in this process is usually referred to as the analysis; the short model forecast used to produce the analysis is called the background.
<b>Depolarised</b>	Refers to a change in polarisation of a transmitted radar pulse as a result of various interactions with the terrain surface.
<b>Depression angle</b>	The angle between the imaginary horizontal plane passing through the antenna and the line connecting the antenna and the target.
<b>Dielectric constant</b>	Electrical property of matter given as a factor by which the electric field between charges is decreased or increased relative to vacuum.
<b>Discrete Global Grid (DGG)</b>	A regular tessellation of a manifold or 2-D surface that divides it into a series of contiguous cells, which can then be assigned unique identifiers and used for spatial indexing purposes.
<b>Distributed targets</b>	In radar, extensive target made-up of several individual small-sized targets.
<b>Doppler shift</b>	Change in the observed frequency of a electromagnetic wave caused by the relative motion between transmitter and receiver.
<b>Dry backscatter reference</b>	In the TU Wien soil moisture retrieval algorithm, the backscatter coefficient

	<h1>The SCIRoCCo Scatterometry Handbook</h1>	<b>Ref:</b>	SCI-PUB-14-0001-v01
		<b>Issue:</b>	6
		<b>Date:</b>	10/10/2017
		<b>Proj:</b>	SCIRoCCo Scatterometer Instrument Competence Centre

	corresponding to the driest observed soil condition.
<b>Dry cross-over angle</b>	In the TU Wien soil moisture retrieval algorithm, cross-over angle used for the determination of the dry backscatter reference.
<b>Electromagnetic radiation</b>	Energy propagated in the form of and advancing interaction between electric and magnetic fields. All electromagnetic radiation moves at the speed of light.
<b>Electromagnetic spectrum</b>	Continuous sequence of electromagnetic energy arranged according to wavelength or frequency.
<b>Emission</b>	Process by which a body radiates electromagnetic energy. Emission is determined by kinetic temperature and emissivity.
<b>Emissivity</b>	Ratio of radiant flux from a body to that from a blackbody at the same kinetic temperature and emissivity.
<b>Error propagation</b>	Effect of the uncertainties of a set of variables on the uncertainty of a function based on them.
<b>Estimated Standard Deviation (ESD)</b>	In the TU Wien soil moisture retrieval algorithm, a static estimated of the backscatter noise at a given location on the Earth's surface.
<b>European Remote Sensing Satellite (ERS)</b>	European earth observation satellite with a payload of various instruments operated by ESA.
<b>European Space Agency (ESA)</b>	Intergovernmental organisation of European countries, dedicated to the exploration of space.
<b>External calibration</b>	Calibration process utilising calibration targets/references outside the instrument itself.
<b>Fan-beam antenna</b>	A directional antenna producing a main beam with a narrow beamwidth in one dimension and a wider beamwidth in the other dimension.
<b>Far range</b>	The portion of a radar beam farthest from the spacecraft flight path.
<b>Foreshortening</b>	A distortion in radar images causing the lengths of slopes facing the antenna to appear shorter on the image than on the ground.
<b>Frequency</b>	The number of wave oscillations per unit time or the number of wavelengths that pass a point per unit time.
<b>Frequency band</b>	A wavelength interval in the electromagnetic spectrum.
<b>Gamma nought (<math>\gamma_0</math>) backscatter coefficient</b>	Representation of the backscatter dedicated for volume scatterer which is proportional to the projected area of the incident energy.

	<h1>The SCIRoCCo Scatterometry Handbook</h1>	<b>Ref:</b>	SCI-PUB-14-0001-v01
		<b>Issue:</b>	6
		<b>Date:</b>	10/10/2017
		<b>Proj:</b>	SCIRoCCo Scatterometer Instrument Competence Centre

<b>Geocentric latitude</b>	A geographic coordinate that specifies the north-south position of a point on the Earth's surface. Defined as the angle between the radius, from centre to the point on the reference ellipsoid surface, and the equatorial plane.
<b>Geodetic latitude</b>	A geographic coordinate that specifies the north-south position of a point on the Earth's surface. Defined as the angle between the reference ellipsoid surface normal and the equatorial plane.
<b>Geophysical Model Function, GMF</b>	Functional relationship between NRCS and U10N, wind direction, radar beam azimuth angle, incidence angle, radar wavelength and polarization.
<b>Geophysical noise</b>	Noise induced by IFOV differences in the multiplet of WVC NRCSs. IFOV differences in combination with geophysical variability cause NRCS inconsistencies between the different views, called geophysical noise. Geophysical noise generally dominates over other noise contributions at low winds.
<b>Goddard Earth Model (GEM)</b>	Geopotential model of the Earth used in theoretical analysis of measuring and calculating the effects of the Earth's gravitational field.
<b>Grid Point Index (GPI)</b>	Unique identifier used for spatial indexing purposes of a Discrete Global Grid.
<b>Grid spacing / sampling</b>	Spacing between different grid point indices of a Discrete Global Grid, given as a distance or angle measure with respect to a sphere or ellipsoid.
<b>Ground range</b>	The distance from the ground track of the satellite to an object.
<b>Gyroscope</b>	A device for measuring or maintaining orientation, based on the principles of angular momentum.
<b>Half-power beamwidth</b>	The angle between the -3 dB points of the antenna main lobe, when referenced to the peak effective radiated power of the main lobe.
<b>Hamming window</b>	A taper formed mathematical function based on a weighted cosine that is zero-valued outside of some chosen interval with applications in spectral analysis, filter design and beamforming.
<b>Incidence angle</b>	Angle between a electromagnetic wave incident on a Earth's surface and the line perpendicular to the point of incidence.
<b>Integrated Field Of View (IFOV)</b>	Backscatter area of a number of contributions of a given wavelength, polarization and azimuth assigned to a particular WVC.
<b>Internal calibration</b>	Calibration process utilising calibration targets/references inside the instrument itself.
<b>Inversion</b>	Bayesian inference of the wind PDF, given a multiplet of NRCS values in a WVC,

	<h2 style="text-align: center;">The SCIRoCCo Scatterometry Handbook</h2>	<b>Ref:</b>	SCI-PUB-14-0001-v01
		<b>Issue:</b>	6
		<b>Date:</b>	10/10/2017
		<b>Proj:</b>	SCIRoCCo Scatterometer Instrument Competence Centre

	its noise properties and the GMF. The wind PDF obtained is generally multi-modal and therefore the wind vector information is ambiguous.
<b>Ka-band</b>	A microwave band with a wavelength (frequency) interval ranging from 1.1 - 0.75 cm (27 - 40 GHz) in the electromagnetic spectrum.
<b>K-band</b>	A microwave band with a wavelength (frequency) interval ranging from 1.7 - 1.1 cm (18 - 27 GHz) in the electromagnetic spectrum.
<b>Ku-band</b>	A microwave band with a wavelength (frequency) interval ranging from 2.5 - 1.7 cm (12 - 18 GHz) in the electromagnetic spectrum.
<b>Latitude</b>	A geographic coordinate that specifies the north-south position of a point on the Earth's surface.
<b>Layover</b>	In radar images, the geometric displacement of the top of objects toward the near range relative to their base.
<b>L-band</b>	A microwave band with a wavelength (frequency) interval ranging from 30 - 15 cm (1 - 2 GHz) in the electromagnetic spectrum.
<b>Linear frequency modulation (chirp)</b>	In signal processing, the encoding of information in a carrier wave by increasing or decreasing the signal frequency with time.
<b>Local slope</b>	In the TU Wien soil moisture retrieval algorithm, intermediate model parameter used for a robust estimation of the parameters slope and curvature to normalised the backscatter coefficient to a reference incidence angle.
<b>Longitude</b>	A geographic coordinate that specifies the east-west position of a point on the Earth's surface.
<b>Look angle</b>	The angle between the vertical plane containing a radar antenna and the direction of radar propagation. Complementary to the depression angle.
<b>Look direction</b>	Direction/angle defined in the horizontal plane with reference to north, in which pulses of microwave energy are transmitted or received by a radar system.
<b>Look-Up Table (LUT)</b>	A mathematical formula expressed as a table used to convert one distribution of data to another.
<b>Low Earth Orbit (LEO)</b>	Satellite orbit around the Earth with an appr. altitude between 160 km and 2000 km and a orbit period between 88 min. and 127 min.
<b>Maximum likelihood estimator, mle</b>	Inversion residual. The multiplet of backscatter data is inverted to 3 parameters: wind speed, wind direction and MLE. Therefore, the MLE measures the difference of the measured backscatter multiplet and the multiplet given by the solution wind

	<h1>The SCIRoCCo Scatterometry Handbook</h1>	<b>Ref:</b>	SCI-PUB-14-0001-v01
		<b>Issue:</b>	6
		<b>Date:</b>	10/10/2017
		<b>Proj:</b>	SCIRoCCo Scatterometer Instrument Competence Centre

	speed and direction in the given satellite geometry of the WVC, according to the GMF. Hence, the MLE is a measure of the inconsistency of the measured backscatter multiplet with the GMF.
<b>Microwave spectrum</b>	Region of the electromagnetic spectrum in the wavelength range of 0.1 to 30 cm.
<b>Mie scattering</b>	Scattering mechanism taking place if the target size is similar to the wavelength resulting in resonant effects.
<b>Monostatic radar equation</b>	Radar equation in case of a single physically antenna acting as transmitter and receiver.
<b>Nadir</b>	Point on the ground directly in line with the remote sensing system and the centre of the earth.
<b>Near range</b>	Refers to the portion of a radar image closest to the satellite flight path.
<b>Noise</b>	Random or repetitive events that obscure or interfere with the desired information.
<b>Normalised radar cross section, nr<sub>cs</sub>, σ<sup>0</sup></b>	Effective backscattering area of a surface in case of plane microwave radiation incident on a scattering object or a scattering medium. It is computed as the ratio of the intensity scattered back in the direction toward the source and the incident irradiance from the source.
<b>Orbit</b>	Path of a satellite around a body such as the earth, under the influence of gravity.
<b>Orbit duration</b>	Time elapsed for one complete satellite path around a body such the Earth.
<b>Passive microwave remote sensing</b>	Remote sensing of microwave energy naturally reflected or radiated from the Earth's surface.
<b>Pencil-beam antenna</b>	A directional antenna producing a main beam with a narrow beamwidth in along and across track direction.
<b>Pitch</b>	Rotation of a satellite about the horizontal axis normal to its longitudinal axis that causes a nose-up or nose-down attitude.
<b>Point targets</b>	A single target having small dimensions compared to the resolution of a radar.
<b>Polar orbit</b>	An orbit that passes close to the poles, thereby enabling a satellite to pass over most of the Earth's surface, except the immediate vicinity of the poles themselves.
<b>Polarisation</b>	The direction of orientation in which the electrical field vector of electromagnetic radiation circulate.
<b>Polarised radiation</b>	Electromagnetic radiation in which the electrical field vector is contained in a single plane, instead of having random orientation relative to the propagation



	<h1>The SCIRoCCo Scatterometry Handbook</h1>	<b>Ref:</b>	SCI-PUB-14-0001-v01
		<b>Issue:</b>	6
		<b>Date:</b>	10/10/2017
		<b>Proj:</b>	SCIRoCCo Scatterometer Instrument Competence Centre

	vector.
<b>Post-launch calibration</b>	Calibration process performed after the launch of a space-borne instrument utilising artificial and/or natural calibration targets.
<b>Pre-launch calibration</b>	Calibration process performed before the launch of a space-borne instrument to characterise the performance of individual instrument sub-systems.
<b>Pulse</b>	Short burst of electromagnetic radiation transmitted by a radar antenna.
<b>Pulse compression</b>	Signal processing technique used to increase the range resolution as well as the signal to noise ratio of a radar.
<b>Pulse duration</b>	Interval between the time, during the first transition, that the pulse amplitude reaches a specified fraction (level) of its final amplitude, and the time the pulse amplitude drops, on the last transition, to the same level.
<b>Pulse repetition frequency</b>	Number of pulses transmitted by a radar per unit time interval.
<b>Radar</b>	Acronym for radio detection and ranging. Radar is an active form of remote sensing that operates in the microwave wavelength regions.
<b>Radar cross section</b>	A measure of the intensity of backscattered radar energy from a point target. Expressed as the area of a hypothetical surface which scatters radar equally in all directions and which would return the same energy to the antenna.
<b>Radar equation</b>	Mathematical representation of the dependency between the transmitted to the received electromagnetic power of a radar.
<b>Radar scattering coefficient</b>	A measure of the back-scattered energy from a target with a large area. Expressed as the average radar cross section per unit area in decibels (dB). It is the fundamental measure of the radar properties of a surface.
<b>Radiometric accuracy</b>	Closeness to which the result of a measurement conforms to the correct value of a physical quantity of interest.
<b>Radiometric calibration</b>	Determination of the relationship between the raw instrument recordings and the physical quantity of interest with its noise related uncertainty.
<b>Radiometric resolution</b>	Ability of a radar to discriminate very slight differences in energy scattered back to the instrument.
<b>Range</b>	In radar, this is the distance in the direction of radar propagation, usually to the side of the platform.
<b>Range binning</b>	Received backscatter energy is binned according to the time delay of transmission and reception to achieve sub-beamwidth resolution.

	<h2 style="text-align: center;">The SCIRoCCo Scatterometry Handbook</h2>	<b>Ref:</b>	SCI-PUB-14-0001-v01
		<b>Issue:</b>	6
		<b>Date:</b>	10/10/2017
		<b>Proj:</b>	SCIRoCCo Scatterometer Instrument Competence Centre

<b>Range direction</b>	see look direction
<b>Range resolution</b>	Spatial resolution in the range direction, which is determined by the pulse length of the transmitted microwave energy.
<b>Rayleigh criterion</b>	In radar, the relationship between surface roughness, depression angle, and wavelength that determines whether a surface will respond in a rough or smooth fashion to the radar pulse.
<b>Rayleigh scattering</b>	Scattering mechanism taking place if the target size is much smaller than the wavelength resulting in resonant effects.
<b>Reflectivity</b>	Ability of a surface to reflect incident energy.
<b>Refraction</b>	Bending of electromagnetic rays as they pass from one medium into another when each medium has a different index of refraction.
<b>Relative calibration</b>	Determination of the relative bias of an instrument to a defined standard.
<b>Remote sensing</b>	Group of techniques for collecting and interpreting information about an distant object without being in physical contact with the object.
<b>Repeat cycle</b>	Fixed time interval after that a satellite repeats its path on the ground.
<b>Roll</b>	Rotation of an aircraft that causes a wing-up or wing-down attitude.
<b>Roughness</b>	In radar, the average vertical relief of a small-scale irregularities of the terrain surface. Also called surface roughness.
<b>Satellite</b>	An object in orbit around a celestial body.
<b>Scattering</b>	Multiple reflections of electromagnetic waves by particles or surfaces.
<b>Scatterometer</b>	Radar system that emits microwave signals to measure the power received from surface backscattering to infer earth's surface properties by measuring a multiplet of backscattering cross sections. The multiplet of signals typically includes different azimuth views and/or microwave polarizations at wavelengths on the cm scale. Satellite microwave scatterometers are mainly launched to obtain ocean vector winds, but other geophysical variables, such as soil moisture, sea ice and snow parameters, or vegetation are also obtained.
<b>Sensor</b>	Device that receives electromagnetic radiation and converts it into a signal that can be recorded and displayed as either numerical data or an image.
<b>Sensor inter-calibration</b>	Calibration of two or more sensors with respect to a common reference.
<b>Sensor intra-calibration</b>	Calibration of a single sensor to a sensor dependent reference.

	<b>The SCIRoCCo</b> <b>Scatterometry Handbook</b>	<b>Ref:</b>	SCI-PUB-14-0001-v01
		<b>Issue:</b>	6
		<b>Date:</b>	10/10/2017
		<b>Proj:</b>	SCIRoCCo Scatterometer Instrument Competence Centre

<b>Signal</b>	Information recorded by a remote sensing system.
<b>Signal to noise ratio</b>	The ratio of the level of the signal carrying real information to that carrying spurious information as a result of defects in the system.
<b>Slant range</b>	In radar, an imaginary line running between the antenna and the target.
<b>Slope</b>	In the TU Wien soil moisture retrieval algorithm, the first derivative of the backscatter as function of the incidence angle
<b>Soil moisture model parameters</b>	In the TU Wien soil moisture retrieval algorithm, parameters driving a model to retrieve surface soil moisture estimates from backscatter coefficient observations by the use of a change detection algorithm.
<b>Spatial resampling</b>	The calculation of new value at a location of interest, based on the values in the local area around the location of interest.
<b>Spatial resolution</b>	Ability of a radar to separate closely spaced objects on the ground.
<b>Speckle</b>	Random constructive and destructive interference from the multiple scattering returns.
<b>Specular reflection</b>	Scattering mechanism at which the angle of the incoming wave is the same as the angle of the outgoing/reflected wave with reference to the surface normal.
<b>Stress-equivalent 10-m-height wind speed, u10s</b>	Wind speed inferred from scatterometer backscatter measurements of the ocean surface at a height of 10 m. Atmospheric stability and density changes the relationship between ocean roughness (radar cross section) and the real wind at 10-m height. Therefore, scatterometer winds are taken at average mass density and an equivalent neutral atmospheric stability, and are compared to NWP or buoy U10S, i.e., winds corrected for atmospheric stability and mass density effects in the lowest 10 m.
<b>Sub-beamwidth resolution</b>	Extraction of target information within an antenna beam by utilising directional information to achieve higher spatial resolutions.
<b>Surface soil moisture (SSM)</b>	In the TU Wien soil moisture retrieval algorithm, representing the water content within the topsoil layer given as degree of saturation in percentage.
<b>Swath</b>	Strip of the Earth's surface from which information is collected by a radar.
<b>Swath grid</b>	Spatial grid defined within the swath of a radar used to georeference observations.
<b>Target</b>	Object on the Earth's surface of specific interest in a remote sensing investigation.
<b>Thinning</b>	A procedure to reduce the density of data

	<h2 style="text-align: center;">The SCIRoCCo Scatterometry Handbook</h2>	<b>Ref:</b>	SCI-PUB-14-0001-v01
		<b>Issue:</b>	6
		<b>Date:</b>	10/10/2017
		<b>Proj:</b>	SCIRoCCo Scatterometer Instrument Competence Centre

<b>Time-series</b>	A series of values of a quantity obtained at successive times not necessarily with equal intervals between them.
<b>Transmissivity</b>	Property of a material that determines the amount of energy that can pass through the material.
<b>Validation</b>	Process of confirming the validity of data to a known reference.
<b>Volume scattering</b>	Interaction between electromagnetic radiation and the interior of a material resulting in radiation scattered equally in all directions.
<b>Wavelength</b>	Distance between successive wave crests or other equivalent points in a harmonic wave.
<b>Wet backscatter reference</b>	In the TU Wien soil moisture retrieval algorithm, the backscatter coefficient corresponding to the wettest observed soil condition.
<b>Wet cross-over angle</b>	In the TU Wien soil moisture retrieval algorithm, cross-over angle used for the determination of the wet backscatter reference.
<b>Wet reference correction</b>	In the TU Wien soil moisture retrieval algorithm, a correction applied to the wet reference in climate regions where likely no wettest soil conditions were observed.
<b>Wind Vector Cell (WVC)</b>	Square area in a scatterometer swath, defined by an equidistant across-track range. Each subsequent range is numbered in an order depending on scatterometer swath type. The along-track range is chosen identical to the across-track range such that square cells are defined.
<b>X-band</b>	A microwave band with a wavelength (frequency) interval ranging from 3.7 - 2.5 cm (8 - 12 GHz) in the electromagnetic spectrum.
<b>Yaw</b>	Rotation of an aircraft about its vertical axis so that the longitudinal axis deviates left or right from the flight line.